Acceleration of polarized protons to 22 GeV/c and the measurement of spin-spin effects in $p_\uparrow + p_\uparrow \rightarrow p + p$

F. Z. Khiari,[a] P. R. Cameron,[a] G. R. Court,[b] D. G. Crabb, M. Fujisaki,[c] I. Gialas, P. H. Hansen,[d] M. E. Hejazifar,[e] A. D. Krisch, A. M. T. Lin, S. L. Linn,[f] D. C. Peaslee,[g] R. S. Raymond, R. R. Raylman, T. Roser, T. Shima,[h] and K. M. Terwilliger
Randall Laboratory of Physics, The University of Michigan, Ann Arbor, Michigan 48109

L. A. Ahrens, J. G. Alessi, H. N. Brown, K. A. Brown, E. D. Courant, G. T. Danby, S. Giordano, H. J. Halama, A. Kponou, R. Lambiase,[i] S. Y. Lee, Y. Y. Lee, R. E. Lockey, Y. I. Makdisi, P. A. Montemurro, R. J. Nawrocky, L. G. Ratner, J. F. Skelly, T. J. Sluyters, A. Soukas, S. Tepikian, and R. L. Witkover
Alternating Gradient Synchrotron Department, Brookhaven National Laboratory, Upton, New York 11973

J. B. Roberts and G. C. Phillips
Bonner Laboratory, Rice University, Houston, Texas 77001

V. W. Hughes and P. Schüler
Gibbs Laboratory of Physics, Yale University, New Haven, Connecticut 06511

J. A. Bywater[j] and R. L. Martin
High Energy Physics Division, Argonne National Laboratory, Argonne, Illinois 60439

J. R. O'Fallon[k]
Office of Advanced Studies and Department of Physics, University of Notre Dame, Notre Dame, Indiana 46556

T. S. Bhatia[l] and L. C. Northcliffe
Department of Physics, Texas A&M University, College Station, Texas 77843

M. Simonius
Institute for Medium Energy Physics, Eidgenossische Technische Hochschule Zurich, CH-8093 Zurich, Switzerland

(Received 11 May 1988)

Accelerating polarized protons to 22 GeV/c at the Brookhaven Alternating Gradient Synchrotron required both extensive hardware modifications and a difficult commissioning process. We had to overcome 45 strong depolarizing resonances to maintain polarization up to 22 GeV/c in this strong-focusing synchrotron. At 18.5 GeV/c we measured the analyzing power A and the spin-spin correlation parameter A_{nn} in large-P_1^2 proton-proton elastic scattering, using the polarized proton beam and a polarized proton target. We also obtained a high-precision measurement of A at $P_1^2 = 0.3$ (GeV/c)^2 at 13.3 GeV/c. At 18.5 GeV/c we found that $A_{nn} = (-2 \pm 16)\%$ at $P_1^2 = 4.7$ (GeV/c)^2, where it was about 60% near 12 GeV at the Argonne Zero Gradient Synchrotron. This sharp change suggests that spin-spin forces may have a strong and unexpected energy dependence at high P_1^2.

INTRODUCTION

The study of spin effects began when the concept of spin was first introduced in the 1920s.[1] Spin soon became an integral part of quantum mechanics and atomic physics and the proton and electron were both assigned[2] a spin of $\frac{1}{2}$. During the 1930s physicists realized that nuclear interactions had a strong spin dependence[3] and they added both a spin-orbit and a spin-spin potential to the central potential.

During the 1940s physicists realized that to understand spin forces they must study scattering processes with the beam particles spin polarized. A theoretical formalism to describe these spin experiments was then developed by Wolfenstein,[4] who also suggested a way to obtain a polarized proton beam. His proposal was similar to an earlier suggestion by Mott[5] to polarize an electron beam by scattering it from a first target (polarizer) and then to analyze its spin state by scattering it from a second target (analyzer).

During the 1950s, a series of such double- and triple-scattering experiments were performed at Rochester,[6] Berkeley,[7] Carnegie,[8] and Chicago.[8] The sizable polarizations found in these p-p and n-p experiments indicated large spin forces in the 150-to-450-MeV range. These experimental results were used in a detailed phase-shift analysis which attempted to discriminate between the different models of strong interactions.[9] However, these

double- and triple-scattering experiments became impractical above 1 GeV because the small scattering cross sections caused large statistical errors.

During the 1960s, polarized proton targets were built at Saclay,[10] Berkeley,[11] CERN,[12–14] and Argonne.[15,16] Polarized targets have allowed measurements of spin effects in p-p elastic scattering up to $P_{\rm Lab}=300$ GeV/c (Refs. 17–19). However, if only the target is polarized, the measurements are sensitive only to the spin-orbit part of the strong interaction. To measure the spin-spin forces requires that a polarized proton beam be scattered from a polarized proton target.

During the 1970s, the world's first high-energy polarized proton beam was accelerated at the 12-GeV Argonne Zero Gradient Sychrotron (ZGS).[20] Good polarized proton sources had already been developed,[21] but preserving the beam polarization during the ZGS acceleration cycle was quite difficult. The ZGS allowed the first precise measurements of two-spin effects at GeV energies; these measurements showed an interesting and unexpected structure.[22,23] One surprising result was that violent proton-proton collisions occurred much more often when the protons' spins were parallel than when they were antiparallel. The ratio $(d\sigma/dt)_{\rm parallel}$:$(d\sigma/dt)_{\rm antiparallel}$ increased rapidly at large momentum transfer, reaching a maximum value of 4 near $P_\perp^2=5.6$ (GeV/c)^2. This was the maximum $P_\perp^2$ possible at the ZGS peak energy of about 13 GeV/c; therefore, going to a higher $P_\perp^2$ required a higher-energy polarized proton beam.

The world's highest-energy accelerated polarized proton beam was first accelerated to 16.5 GeV/c at the Brookhaven Alternating Gradient Synchrotron (AGS);[24,25] later the AGS reached 22 GeV/c (Refs. 26–28). Unlike the ZGS, which was a weak-focusing accelerator, the AGS is a strong-focusing accelerator with many strong depolarizing resonances. Therefore, it was much more difficult to preserve the proton polarization at the AGS than at the ZGS. Accelerating a polarized proton beam in a strong-focusing accelerator was a painstaking task which required extensive work.[29–33]

We then made the first measurement of proton-proton elastic-scattering cross sections above ZGS energies with both a polarized proton beam and a polarized proton target. The study of spin effects gives a more complete picture of the dynamics of strong interactions than the measurement of spin-averaged cross sections. We studied the spin parameter as a function of the beam momentum $P_{\rm Lab}$, the momentum transfer squared $P_\perp^2$, and the center-of-mass scattering angle $\theta_{\rm c.m.}$.

This paper contains a detailed description of the AGS polarized proton beam, including both the hardware modifications and the commissioning. We emphasize the difficult process of overcoming 45 strong depolarizing resonances. We also stress the radio-frequency quadrupole (RFQ), which was the first RFQ ever coupled to an operating accelerator. We then discuss the measurements of the one-spin analyzing power A and the spin-spin correlation parameter A_{nn} in $p_\uparrow+p_\uparrow\rightarrow p+p$. These experiments were done using the AGS polarized proton beam, the University of Michigan polarized proton target, and a double-arm spectrometer containing magnets and scintillator hodoscopes. The measurements were made at $P_{\rm Lab}=13.3$ to 18.5 GeV/c and at $P_\perp^2=0.3$ to 4.7 (GeV/c)^2. Our measurement at $P_{\rm Lab}=18.5$ GeV/c and $P_\perp^2=4.7$ (GeV/c)^2 is the first high-$P_\perp^2$ spin-spin measurement above ZGS energies and the first high-$P_\perp^2$ measurement far from $90°_{\rm c.m.}$.

POLARIZED PROTON BEAM

The polarized beam at the Brookhaven Alternating Gradient Synchrotron (AGS) originated as a negatively ionized vertically polarized hydrogen beam from a polarized ion source. The $H_\uparrow^-$ ions were then injected into the radio-frequency quadrupole (RFQ) and accelerated to 760 keV. The beam was transported by the new low-energy beam-transport line[34] through two 60° bends into the AGS linac and accelerated to 200 MeV. The $H_\uparrow^-$ beam was then injected into the AGS main ring where a carbon stripping foil converted it into a polarized proton beam. The polarized protons were accelerated to about 20 GeV and then extracted to the experimental area. During the acceleration cycle, the horizontal magnetic fields in the ring magnets could rotate the polarization vector away from the vertical. At certain discrete energies this depolarization was coherent and the polarization was lost very rapidly; these depolarizing resonances occurred whenever the perturbing fields had a frequency equal to the spin precession frequency. It was a major problem to overcome these depolarizing resonances and thus maintain the polarization during the acceleration cycle. Three polarimeters monitored the beam polarization during the acceleration cycle. Figure 1 shows a layout of the AGS, highlighting the modifications which were made to allow the acceleration of polarized protons.

Polarized-ion source

The ion source used at the AGS was a Haeberli-type pulsed polarized negative-hydrogen-ion source,[35] which is shown in Figs. 2 and 3. The atomic-beam stage was an improved version of the ANAC source used at the ZGS (Refs. 21 and 36). Molecular hydrogen diffused from the gas bottle into a dissociator where intense radio-frequency irradiation at 20 MHz broke the hydrogen molecules into atomic hydrogen. The totally unpolarized atoms were then cooled to about 100 K by collisions with the exit nozzle of the dissociator, which was cooled to 90 K by a closed-cycle He refrigerator. The thermal atomic beam then entered the strong inhomogeneous magnetic field of the sextupole magnets. Because the magnetic moment of the electron, μ_e, is 660 times larger than that of the proton, the magnetic field acted primarily on the electron. Inside the sextupole, the Stern-Gerlach force on the electron was

$$\mathbf{F}(m_e=\pm\tfrac{1}{2})=\mp 2B_m\mu_e\frac{\mathbf{r}}{r_m^2}\ , \tag{1}$$

where B_m is the magnetic field at the pole tips, r_m is the radius of the sextupole, and $\mathbf{r}$ is the radius vector of the particle. Atoms with electron spin parallel to the local magnetic field (states 1 and 2 in Fig. 4) were focused and

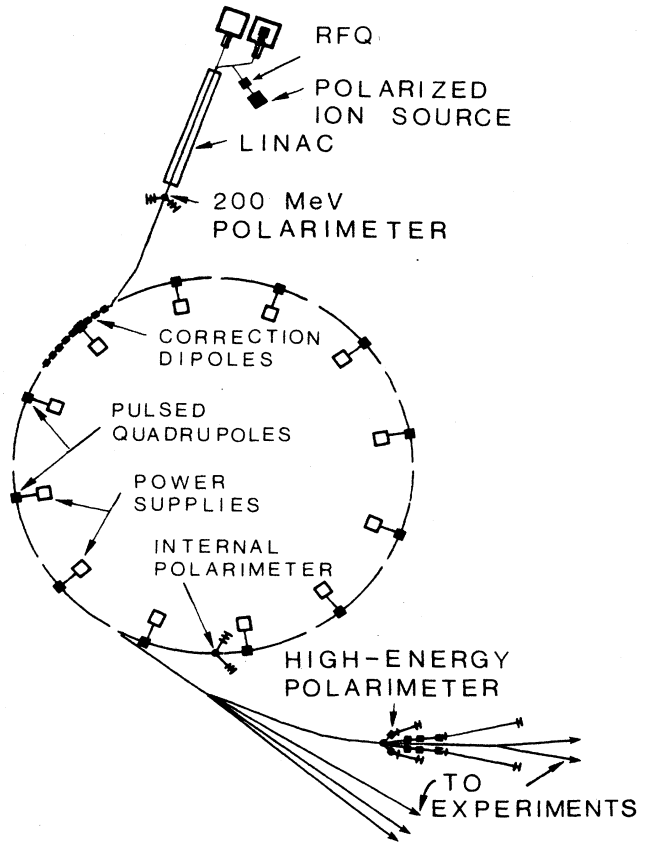

FIG. 1. AGS layout for the operation of the polarized proton beam.

passed through the sextupole, while atoms with the opposite electron spin were defocused into baffles and pumped away. The atomic beam flux was maximized by matching the sextupole magnet's geometry and strength to the average beam velocity. The atoms then passed from the sextupoles into the rf transition cavities slowly enough for the electrons' spins to follow along the local magnetic field and thereby preserve the electrons' polarization.

At this point the protons in the atomic beam were unpolarized while the electrons were spin polarized along the local magnetic field in the rf cavities. The electrons' polarization was then transferred to the protons using rf power at the appropriate frequencies to induce spin transitions between different levels of atomic hydrogen in the $1S_{1/2}$ ground state. These transitions occurred in two adjacent rf cavities which were energized on alternate AGS pulses to reverse the beam polarization. The energy-level diagram of the hyperfine levels of the $1S_{1/2}$ state is plotted in Fig. 4 against the external magnetic field. The transitions from state 1 to state 3 occurred in the cavity with 10 G and 19 MHz, while the state-2 to state-4 transitions occurred in the cavity with 150 G and 1480 MHz. Each of these hyperfine transitions flipped the protons' spins. Thus the 1-to-3 transitions gave the atomic beam a down ($\downarrow$) proton polarization ($m_p = -\frac{1}{2}$), while the 2-to-4 transitions gave the protons an up ($\uparrow$) spin polarization ($m_p = +\frac{1}{2}$). The atomic beam stage emitted up to 16 particle mA of neutral proton-polarized atomic hydrogen into the ionizer in a 5-msec pulse. In leaving the atomic beam stage the proton spin direction followed the local magnetic field and thus turned onto the axis of the ionizer solenoid, where a 500-G axial field preserved the proton polarization during ionization.

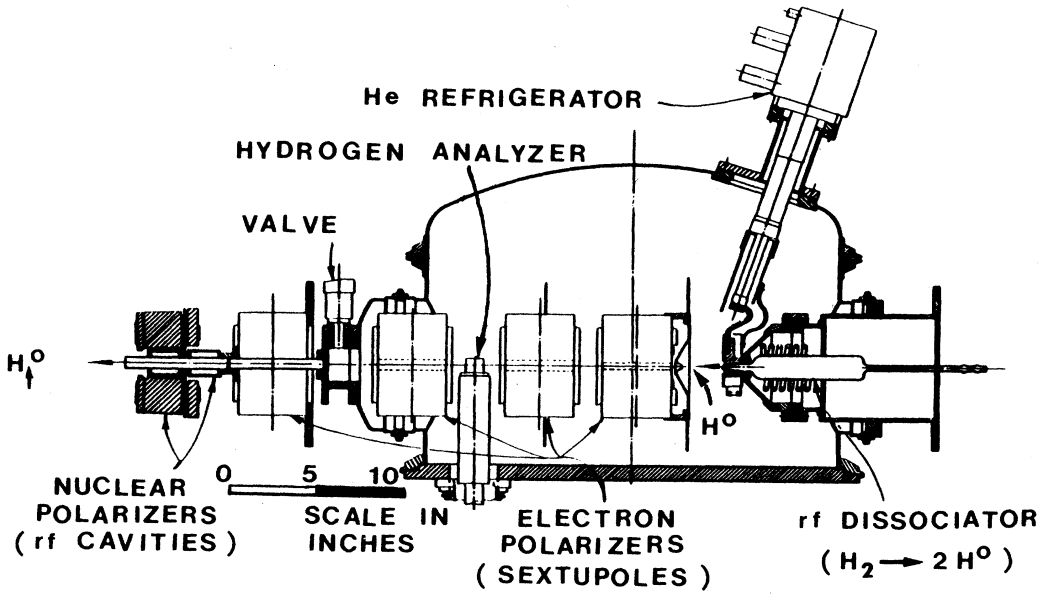

FIG. 2. Atomic-beam stage of the polarized-ion source.

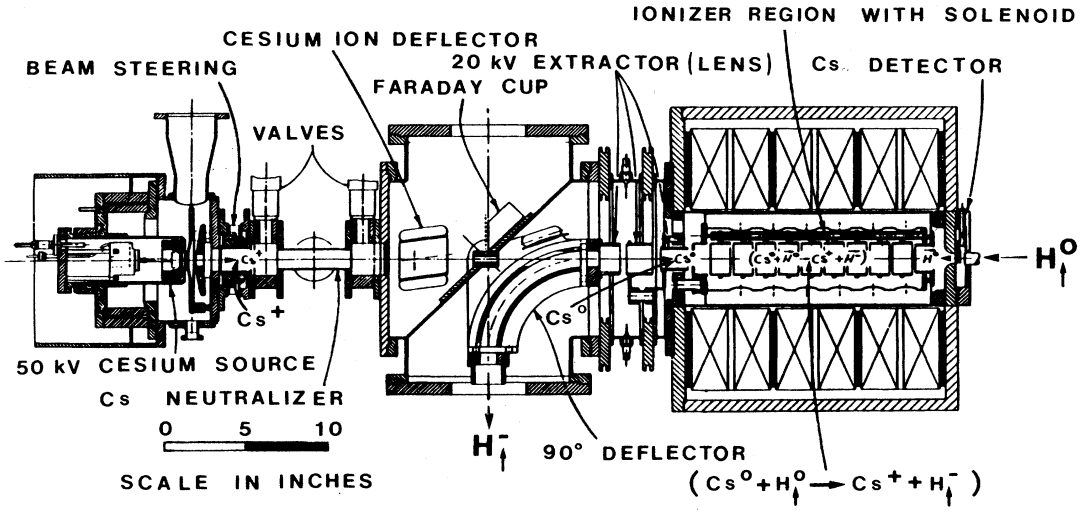

FIG. 3. Cesium source, extractor, and ionization region of the polarized-ion source.

The polarized atomic hydrogen was ionized by interacting with a neutral cesium beam in the 30-cm-long ionization region through the reaction

$$H^0_\uparrow + Cs^0 \rightarrow H^-_\uparrow + Cs^+ \ . \tag{2}$$

The neutral cesium source produced a 40-keV Cs^+ beam by surface ionization of cesium on a hot porous tungsten button. The cesium-ion beam was then neutralized in a pulsed cesium vapor neutralizer. The Cs ionizer voltage was pulsed along with the neutralizer to minimize cesium contamination. With a Cs^0 current of about 6 particle mA reaching the ionization region, about 0.3% of the polarized hydrogen atoms were ionized. The $H^-_\uparrow$ ions produced in this charge-exchange reaction were extracted and accelerated to about 20 keV. They were then focused and deflected by a 90° electrostatic mirror into the transfer line where a magnetic solenoid precessed the $H^-_\uparrow$ spin direction by 90° into the vertical direction just before the beam exited towards the RFQ.

The output current of the $H^-_\uparrow$ source was about 25 μA; the polarization was typically 75%. The source gave a pulse of width about 400-μsec FWHM every 2.2 sec which matched the AGS repetition rate. The emittance of the polarized $H^-_\uparrow$ ion beam was 0.2π mm mrad.

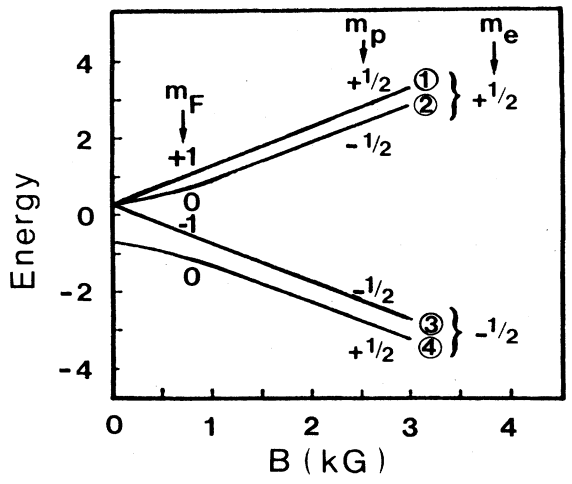

FIG. 4. Energy-level diagram of the $1S_{1/2}$ hyperfine states of atomic hydrogen. The energy units are 5.88×10^{-6} eV, which corresponds to the hfs splitting of 1420 MHz.

Radio-frequency quadrupole

An RFQ is a linac which uses rf electric fields to simultaneously accelerate and focus a low-energy beam of charged particles. The space-charge defocusing force on a particle at radius r has the form[37]

$$F(r)=\frac{2erI}{r_b^2 v}(1-\beta^2) \ , \tag{3}$$

where e is the particle's charge, I is the beam current, r_b is the transverse radius of the beam, and $v=\beta c$ is each particle's speed. Many conventional linear accelerators use quadrupole magnets to focus the particles by overcoming this force and the rf defocusing force. However, magnetic focusing is inefficient at low energies where the magnetic force is small. Therefore, velocity-independent electric focusing appears quite attractive at low energies. The radio-frequency quadrupole (RFQ), proposed by Kapchinskiy and Teplyakov,[38] uses electric quadrupole fields to both focus and accelerate particles to about 1 MeV.

The electric field in an RFQ is generated by four vanes distributed symmetrically around the central axis,[39] as shown in Fig. 5. The vanes are energized by rf power of about 200 MHz with the adjacent vanes having opposite voltages.

Each transverse component of the electric field is focusing during half of the rf period and defocusing during the other half. This gives an RFQ the strong-focusing feature of an alternating-gradient synchrotron

but with a velocity independent strength. The longitudinal accelerating component of the electric field in our RFQ was generated by modulating the distance of the vane tips from the central axis as shown in Fig. 6. The wavelength λ of the rf excitation was equal to about $c/200$ MHz which was about 150 cm. Each particle's $\beta=v/c$ increased as it moved downstream, and it always found itself in a unit cell of length $\beta\lambda/2$, which was about 0.5 cm at the 20-keV entrance and about 3 cm at the 760-keV exit. The modulation parameter m was defined by

$$m=\frac{R(z=\beta\lambda/2)}{R(z=0)}\ , \tag{4}$$

where R is the vane tip radius which is typically 4.6 mm. Each peak of the vertical vane tips occurred at the same longitudinal position as the corresponding valley of the horizontal vane tips. Sequential unit cells had opposite longitudinal fields so that phase focusing gave a particle bunch in every other cell. Each sequential cell of length $\beta\lambda/2$ gave an appropriate acceleration to match the energy and phase in the next cell.

The RFQ fields must be highly uniform along the vanes and in all four quadrants. The correct shape of the vanes is crucial to minimizing beam losses during acceleration. The rather complex shape was achieved by fabricating the vanes with a computer-controlled milling machine.[40] Each vane was then given a highly polished copper electroplating. A cross-sectional diagram of the AGS RFQ is shown in Fig. 7.

The RFQ is a heavily loaded resonant cavity which was excited in the TE211 mode at a frequency of 201.25 MHz, to match the frequency of the AGS 200-MeV linac. We used tapered tuning bars to tune the RFQ to near this resonant frequency and to correct the tilt in the longitudinal fields. We then adjusted the end cell vanes and their capacitors to equalize the fields in all four quadrants and to set exactly the resonant frequency. The 24 paddle tuners were then used to fine-tune the cavity. We compensated for small frequency shifts using three motorized tuners mounted midway along three quadrants while using the fourth quadrant as a reference. Perturbation measurements at the vane tips showed that the longitudinal electric field was uniform to within $\pm 3\%$ in all four quadrants;[41] we generated a field perturbation at each point and then measured the resulting frequency shift at resonance.[42]

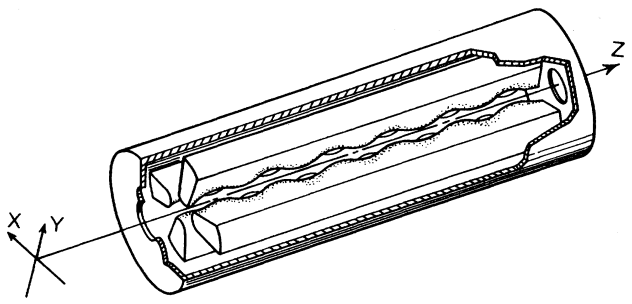

FIG. 5. Schematic of an RFQ showing the vanes.

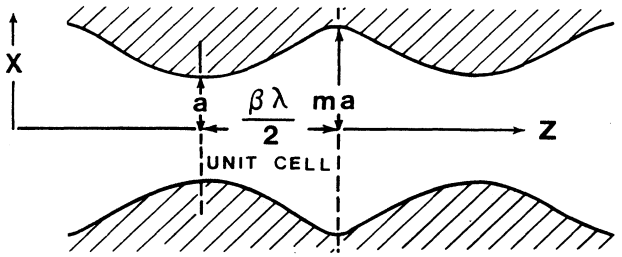

FIG. 6. A cut through one longitudinal plane of the RFQ vanes. There is a voltage of V_0 between the horizontal and vertical planes.

Two degenerate TE111 modes of the RFQ were found at 199.70 and 198.21 MHz. Note that the azimuthal symmetry of the fields would be perfect only if these two degenerate modes occurred at the same frequency. Fortunately these two modes were suppressed by more than 25 dB below the TE211 mode.[41] The TE111 and TE211 rf modes in the RFQ are shown in Fig. 8.

When particles enter an RFQ, their energy gain depends on the time at which they enter. A synchronous particle is one that gains just enough energy to be always in phase with the rf field. If the phase ϕ and the energy E differ from the synchronous phase ϕ_s and the synchronous energy E_s, the particle will either be lost or perform longitudinal oscillations around a synchronous particle.[43]

Besides bunching and accelerating the beam, an RFQ focuses it as well. The transverse motion of each particle in an RFQ is a superposition of a slow betatron oscillation with frequency Ω and a small rapid oscillation with frequency ω (Ref. 44). The average betatron oscillation of the particle is

$$x(t)=x_0\cos(\Omega t)\ . \tag{5}$$

There is net focusing only if Ω is real; this sets a limit on

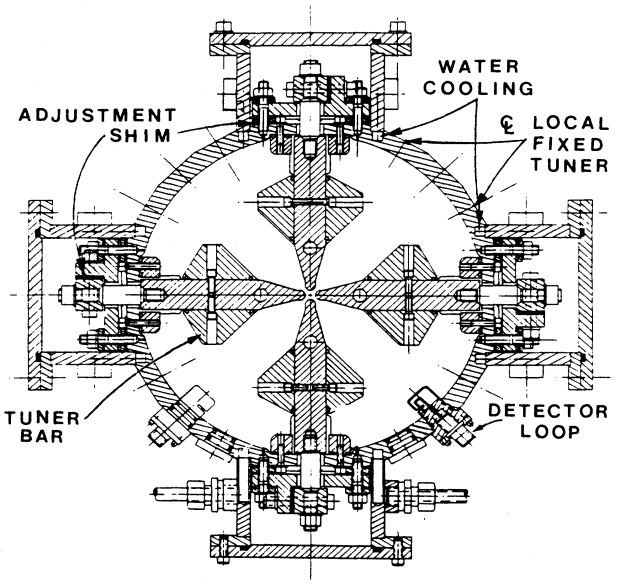

FIG. 7. A cross-sectional diagram of the AGS RFQ cavity.

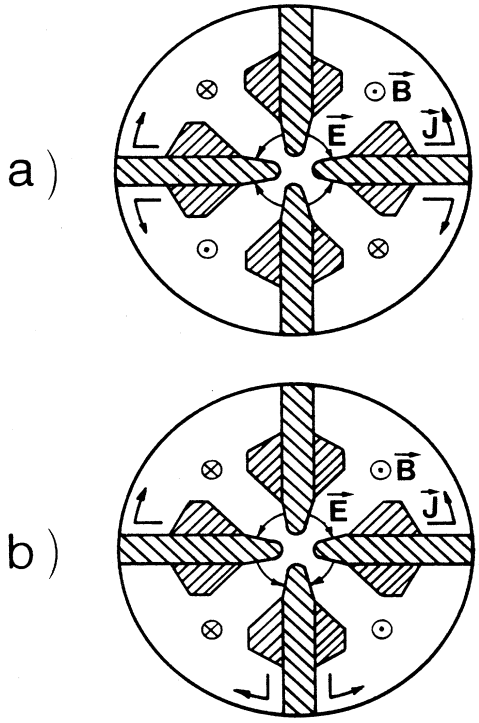

FIG. 8. Diagram of the rf modes in the RFQ showing the electromagnetic fields and wall currents in the (a) TE211 mode and (b) TE111 mode.

the accelerating electric field that can be achieved while preserving transverse focusing. The electric quadrupole strength is XV_0/a^2 where V_0 is the maximum voltage between the vanes, a is the vane radius parameter and X is a transverse parameter of the RFQ.

If a synchronous particle is on axis, its energy gain per unit cell is

$$\Delta W = \int_0^{\beta\lambda/2} eE_z dz = eV_0 \frac{\pi A}{4} \cos(\phi_s) . \quad (6)$$

For the AGS RFQ, the modulation parameter m is 1.969 in the exit region, the longitudinal parameter A is 0.568 and the transverse parameter X is 0.419. Synchronous particles have only betatron oscillations about the longitudinal axis. Nonsynchronous particles also have phase oscillations around the synchronous particles.

The functional elements of our RFQ are shown[41] in Fig. 9, where the particle's energy at the end of each element is indicated. In the radial-matching section, the vanes were not modulated but tapered to allow the radial-focusing force to grow smoothly. This enabled the unbunched beam from the source to adiabatically adjust itself to the time-varying forces in the RFQ. In the shaper section both the synchronus phase ϕ_s and the average longitudinal field E_0 were ramped. The phase ϕ_s started at $-90°$ and was kept large to obtain a high capture efficiency as acceleration was steadily increased. In the gentle buncher, the bunch length and the phase oscillation frequency were kept almost constant until the final synchronous phase was attained while the particle distribution was preserved throughout. Finally, in the accelerator section the polarized H^- ions were accelerated to their final energy at a constant phase value of $\phi_s = -30°$ to maximize acceptance in the linac.[34] Some of the design parameters of the AGS RFQ are listed in Table I.[41]

Beam transport and instrumentation

A new low-energy beam-transport (LEBT) line[34] was constructed to carry the $H_\uparrow^-$ ions from the source to the RFQ and then to the linac. Moreover, beam instrumentation was provided to measure the intensity, the emittance, and the position of the polarized beam. These measurements allowed proper tuning of the beam in the pre-linac LEBT, in the post-linac high-energy beam transport (HEBT), in the AGS main ring, and in the slow-extracted-beam (SEB) lines.

In the LEBT area the polarized H^- beam was first extracted from the ion source at 20 keV and then transported to the RFQ which accelerated it to 760 keV. The beam then passed through two 60° dipoles, 3 bunchers, and several quadrupole lenses and then entered the linac as shown in Fig. 10. The beam intensity could be measured using destructive Faraday cups after the RFQ, after the second 60° magnet and just before and after the first linac tank. A nondestructive measurement of the intensity was made just after the ion source using a beam current transformer with a noise level of about 100 nA and a risetime of about 25 μsec.

A carbon-filament multichannel profile monitor just

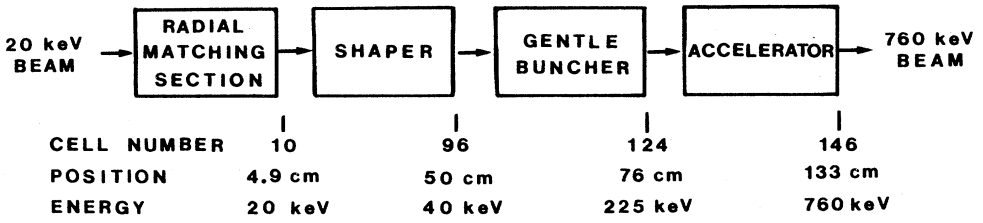

FIG. 9. Block diagram of the RFQ showing the function, the position, and the acceleration energy at the downstream end of each element.

TABLE I. RFQ design parameters.

Frequency	201.25 MHz
Ion type	H^-
Cavity length	148.27 cm
Cavity diameter	32.4 cm
Number of cells (in vane)	144
Vane length	130.28 cm
Intervane voltage V_0	63 kV
Peak surface field E_0	20.9 MV/m
Average radius R	0.464 cm
Final radius a_f	0.299 cm
Final modulation m	1.97
Initial synchronous phase ϕ_i	$-90°$
Final synchronous phase ϕ_f	$-30°$
Estimated peak rf power	60 kW
Nominal current limit	56 mA
Nominal acceptance	2.7π mm mr
Initial energy	20 keV
Final energy	760 keV
Transmission efficiency	95% (80% operational)

after the first 60° bending magnet was used to verify that the RFQ had accelerated the beam to 760 keV and that the beam was properly steered into the transport channel.

The beam emittance was measured just after the ion source to properly adjust the match into the RFQ; it was again measured just after the second 60° bend to tune the transport line, and again just upstream of the linac, to allow adjustment to the linac acceptance. These emittance measurements used the standard AGS moving slit and the 32-channel collection array detector. A preamplifier was added to each channel to compensate for the 10^{-3} lower polarized-beam intensity. The signal-to-noise ratio for the 10–25 μA polarized beam was about 40:1.

The polarized H^- ions were then transported to the linac where they were accelerated to 200 MeV. Their proton polarization was then measured by the 200-MeV polarimeter and the ions were next transported to the AGS main ring. A thin carbon foil then stripped both electrons from the H^- ions; then they were injected into the main ring as polarized protons and captured. The stripped electrons were collected and provided a measure of the injected intensity and the injection efficiency.

Three beam current transformers were used to monitor the beam intensity delivered to the AGS ring. These were located just after the 200-MeV linac, just upstream of the bend in the HEBT transport line from the linac to the AGS, and just after entry into the AGS ring tunnel.

The density distribution or profile was measured in the HEBT line using stepping motor-driven single-wire scanners. Noise was a significant problem because the amplifiers were located outside the transport tunnel about 400 feet away. It was only possible to obtain clean profiles after enclosing the signal cables in steel conduit. These profile monitors were the only tuning monitors available for the HEBT line, but they were difficult to use since they were not interfaced to the control computer. It was also difficult to match the beam into the 200-MeV

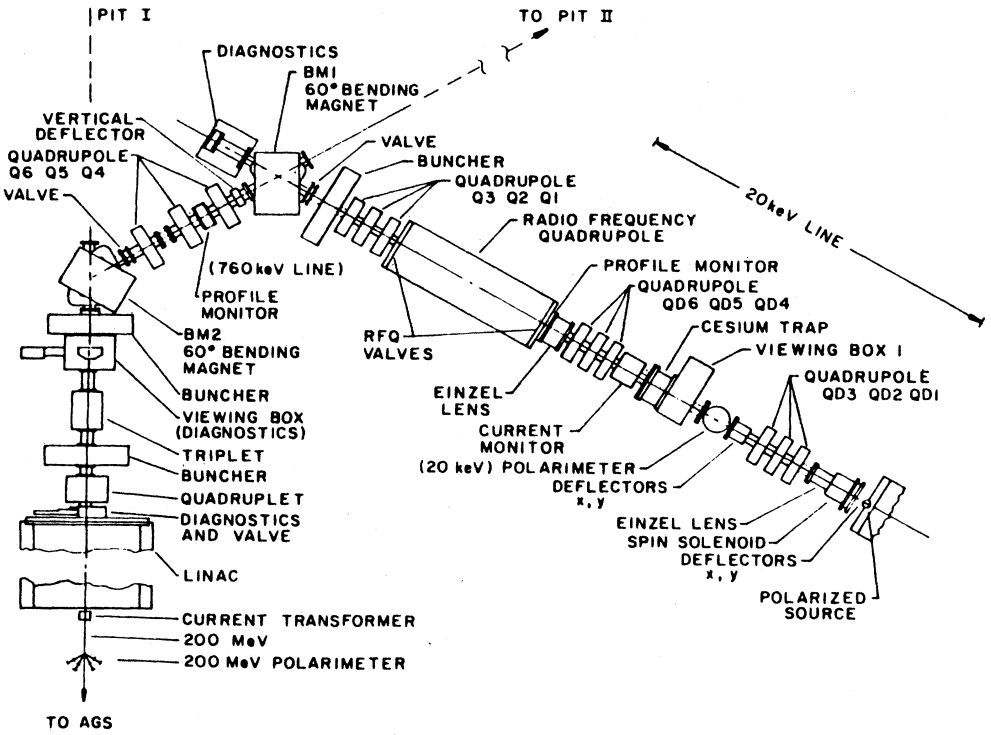

FIG. 10. Layout of the low-energy beam transport, LEBT, area. The polarized H^- ions are emitted by the polarized ion source at 20 keV, accelerated to 760 keV by the RFQ and then steered by two 60° bending magnets into the linac which accelerates them to 200 MeV where their polarization is measured.

polarimeter, which was a limiting aperture, since there was no profile monitor close to the polarimeter.

We made beam-profile measurements inside the AGS main ring using the ionization profile monitor (IPM). During normal unpolarized running with 10^{13} protons in the beam, enough molecules were ionized in the 10^{-7} Torr background vacuum to provide a good measurement of the beam density distribution when integrated for 1 msec. To see a similar signal for polarized proton running, additional gas had to be injected to raise the local pressure to about 10^{-5} Torr and we had to integrate for 10 msec. Since the beam profile measured the emittance, the IPM let us study the beam blow-up problems caused by the pulsed quadrupoles.

Several pick-up electrodes (PUE's) in the main ring were fitted with special amplifiers and used to observe the beam position and the accelerator tune. These PUE's also measured the polarized beam intensity in the AGS ring. Another electrode was instrumented to provide the phase and radial position information required by the control loops of the rf acceleration system.

Depolarizing resonances

As the vertically polarized protons circled the AGS main ring during the acceleration cycle, their polarization vectors precessed around the strong vertical magnetic field, which caused no depolarization. However, the AGS also had horizontal magnetic fields to vertically focus the beam and thus keep it within the vacuum pipe. Unfortunately, these strong horizontal focusing fields could quickly destroy the beam polarization. At the weak-focusing Argonne ZGS these horizontal focusing fields came from the weak edge focusing of the ring dipole magnets. However, the Brookhaven AGS is a strong-focusing synchrotron with strong alternating quadrupole fields superimposed on the main vertical dipole field of the ring magnets. Moreover, the strong imperfection fields in the AGS could also quickly depolarize the beam.

Depolarizing resonances have been studied by many authors;[20,45–49] our discussion will be in the local rest frame of each proton and will be similar to the study by Courant and Ruth.[49] The rotation of the polarization vector **P** of a particle moving in a magnetic field is given by

$$\frac{d\mathbf{P}}{d\theta}=\mathbf{P}\times\mathbf{\Omega}\ , \tag{7}$$

where θ is the angle along the accelerator's path as shown in Fig. 11. The driving term $\mathbf{\Omega}$ is given by the Thomas-Bargman-Michel-Telegdi equation to be[50,51]

$$\mathbf{\Omega}=\frac{e\rho}{\gamma v m c}[(1+G\gamma)\mathbf{B}_{\perp}+(1+G)\mathbf{B}_{\parallel}]\ , \tag{8}$$

where $\mathbf{B}_{\perp}$ and $\mathbf{B}_{\parallel}$ are the magnetic field components transverse and parallel to the velocity **v** of the particle, e and m are the charge and mass of the proton, $G\equiv(g/2)-1=1.792\,85$ is the proton's anomalous magnetic moment, and ρ is the local bending radius. One can describe the proton's motion using the Lorentz force equation

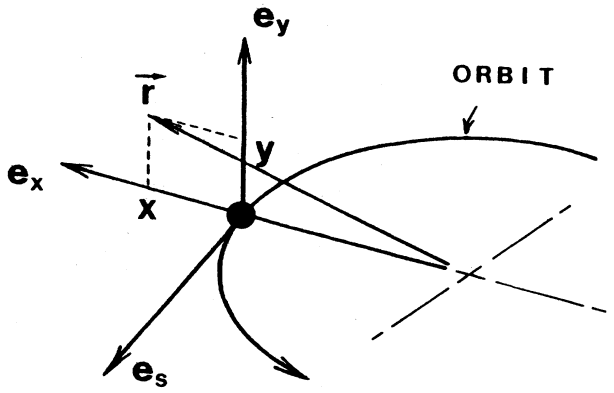

FIG. 11. Local coordinate system in the rest frame of a proton in a circular orbit in a synchrotron.

$$\frac{d\mathbf{v}}{d\theta}=\frac{e\rho}{\gamma v m c}\mathbf{v}\times\mathbf{B}\ . \tag{9}$$

Moreover, one may express $\mathbf{B}_{\perp}$ and $\mathbf{B}_{\parallel}$ in terms of the orbit coordinates x, y, and s in the proton's rest frame.

The equation of motion of a two-component spinor ψ is quite similar to the equation of motion of **P**. We can define $\mathbf{P}=\psi^{\dagger}\boldsymbol{\sigma}\psi$, where the $\boldsymbol{\sigma}$ are the Pauli spin matrices. The equation of motion for ψ is given by

$$\frac{d\psi}{d\theta}=\frac{i}{2}\begin{bmatrix}-G\gamma & \zeta(\theta)\\ \zeta^{*}(\theta) & G\gamma\end{bmatrix}\psi\ , \tag{10}$$

where we have kept only linear terms and $\zeta(\theta)$ describes the depolarizing horizontal fields. Notice that when there are no horizontal fields then $\zeta(\theta)=0$ and Eq. (10) has a simple solution in terms of the Pauli spin matrix σ_y:

$$\psi(\theta)=\exp\left[\frac{-i}{2}\int_0^{\theta}G\gamma\sigma_y d\theta'\right]\psi(0)\ . \tag{11}$$

Thus, when the only fields are vertical, the spinor precesses around the y axis with an instantaneous frequency $G\gamma$. This precession preserves the projection of **P** on the y axis which is given by

$$P_y(\theta)\equiv\psi^{\dagger}(\theta)\sigma_y\psi(\theta)=\psi^{\dagger}(0)\sigma_y\psi(0)\ . \tag{12}$$

Clearly there is no depolarization since **P** only precesses around the vertical magnetic field and $P_y(\theta)$ remains constant.

However, horizontal fields can depolarize vertically polarized protons. Consider a periodic horizontal field described by the function

$$\zeta(\theta)=h\exp(-i\omega\theta)\ , \tag{13}$$

where ω is the frequency of oscillation and h

parametrizes the field's strength. When $G\gamma$ is constant then the average change in the y component of the polarization vector can be obtained by solving Eq. (10):

$$\left\langle \frac{dP_y}{d\theta} \right\rangle \propto \int_0^\theta d\theta\, h\exp[i(G\gamma-\omega)\theta] \ . \tag{14}$$

Normally this integral is periodic with zero average after many revolutions and then there is no change in the polarization. However, at certain points in the acceleration cycle the protons pass through an energy γ which satisfies the relation

$$G\gamma=\omega \ . \tag{15}$$

Then the exponent in Eq. (14) becomes zero and there will be coherent depolarization. The polarization can be lost very rapidly when such a resonant condition occurs. The depolarizing resonances due to the strong-focusing quadrupole fields are called intrinsic depolarizing resonances, while the resonances due to the horizontal imperfection fields are called imperfection depolarizing resonances.

The same horizontal fields which can cause depolarization also cause vertical motion of the beam. This vertical motion has two parts: the closed-orbit displacement due to magnet misalignments, $y_{\rm COD}$, and the displacement due to vertical betatron oscillations, y_β. These vertical motions are described by the equations[52]

$$y_\beta''+K(s)y_\beta=0 \tag{16}$$

and

$$y_{\rm COD}''+K(s)y_{\rm COD}=F(s) \ , \tag{17}$$

where $y''\equiv d^2y/ds^2$, $K(s)$ is the focusing function, and $F(s)$ is the perturbing term due to the horizontal imperfection fields.

We will first discuss the intrinsic depolarizing resonances by solving Eq. (16) for the vertical betatron oscillations

$$y_\beta \propto \sqrt{\beta}\cos(\nu_y\theta) \ . \tag{18}$$

The quantity β is a Twiss parameter[52] called the β function which is related to the instantaneous amplitude of the betatron oscillations. The vertical tune ν_y is the number of vertical betatron oscillations per turn around the accelerator. Thus, as each proton oscillates above and below the central axis, it sees the horizontal fields of the quadrupoles with a frequency $\omega=\nu_y$. From Eq. (15) we see that an intrinsic depolarizing resonance will then occur whenever

$$G\gamma=\omega=\nu_y \ . \tag{19}$$

Moreover, in an accelerator with periodicity P, such an intrinsic depolarizing resonance will occur whenever γ satisfies the equation

$$G\gamma=nP\pm\nu_y \ , \tag{20}$$

where n is any integer. For the Brookhaven AGS the periodicity P is 12, and $\nu_y=8.75$.

We will now discuss the imperfection depolarizing resonances by Fourier expanding the perturbing term $F(s)$ in Eq. (17):

$$F(s)=\sum_k f_k\exp(ik\theta) \ . \tag{21}$$

Putting this expansion back into Eq. (17) and solving for $y_{\rm COD}$ we get

$$y_{\rm COD}\propto\sum_k \frac{f_k}{\nu_y^2-k^2}\exp(ik\theta) \ . \tag{22}$$

In general $y_{\rm COD}$ will not cause much depolarization because this summation has a periodicity similar to the periodicity of the integral in Eq. (14) and is thus close to zero. However, whenever the spin frequency $\omega=G\gamma$ becomes equal to an integer k then a resonant condition will occur and there can be a significant loss of polarization. Such an imperfection depolarizing resonance will occur whenever

$$G\gamma=\omega=k \tag{23}$$

occurs in the acceleration cycle, where k is any integer. Those imperfection resonances with k close to the vertical tune, ν_y, should have an especially strong depolarization as suggested by Eq. (22).

One can analyze the imperfection resonances by expanding the horizontal field parameter[49] ζ as the sum of the strengths ϵ_q of each resonance

$$\zeta(\theta)=\sum_q \epsilon_q\exp(-i\omega_q\theta) \ . \tag{24}$$

We then get, by inverting Eq. (24),

$$\epsilon_q=\frac{1}{2\pi}\oint ds\frac{\zeta(s)}{\rho(s)}\exp[i\omega_q\theta(s)] \ , \tag{25}$$

where $\rho(s)$ is the bending radius of the particle at position s (or θ) in the orbit. One may separate each ϵ_q into a sum of the contributions from each magnet in the accelerator:

$$\epsilon_q=\sum_m \epsilon_{q,m} \ , \tag{26}$$

where

$$\epsilon_{q,m}=\int_{s_1}^{s_2} ds\frac{\zeta(s)}{\rho(s)}\exp(i\omega_q\theta) \ , \tag{27}$$

and s_1 and s_2 lie in the field-free region just outside each magnet's ends. Note that both $1/\rho$ and the focusing function, K, of Eq. (17), are step functions, which are constant inside the magnets and zero in the field-free regions. Let ξ_1 and ξ_2 be the angles that the magnet edges make with the accelerator axis. Then following Courant and Ruth,[49] the focusing function at the magnet ends is given by

$$K=\frac{1}{\rho}[\xi_1\delta(s-s_1)+\xi_2\delta(s-s_2)] \ , \tag{28}$$

where δ is the Dirac δ function. Note that y and $y'\equiv dy/ds$ at the magnet ends are related by[52] the standard vertical betatron oscillation matrix

$$\begin{bmatrix} y_2 \\ y_2' \end{bmatrix} = \begin{bmatrix} \cos(\phi) & \sin(\phi)/\sqrt{K} \\ -\sqrt{K}\sin(\phi) & \cos(\phi) \end{bmatrix} \begin{bmatrix} y_1 \\ y_1' \end{bmatrix} \ , \tag{29}$$

where $\phi \equiv \sqrt{K}\,(s_2 - s_1) \equiv \sqrt{K}\,l$ is the vertical focusing angle in each magnet. Using Eqs. (28) and (29), one can solve[49] Eq. (27) for each magnet of length l which subtends an orbit angle of $\theta = l/\rho$. One can then calculate the strength of each resonance.

Courant and Ruth[49] evaluated the strength ϵ of each depolarizing resonance in the AGS using $y = y_\beta$ with $G\gamma = kP \pm \nu_y$ for intrinsic resonances and $y = y_{\mathrm{COD}}$ with $G\gamma = k$ for imperfection resonances. Their results, using a normalized emittance of 10π mm mrad and random rms magnetic errors of ± 0.1 mm, are shown in Fig. 12.

The polarization P, after passing through an isolated depolarizing resonance, was calculated by Froissart and Stora[45] to be

$$\frac{P}{P_0} = 2\exp(-\pi\epsilon^2/2\alpha) - 1 \ , \tag{30}$$

where P_0 is the polarization before the resonance and ϵ is the resonance strength. The quantity α is the rate at which the resonance is adiabatically crossed during the acceleration cycle. For imperfection resonances this crossing speed is given by

$$\alpha = G\frac{d\gamma}{dt} \ , \tag{31}$$

while for intrinsic resonances

$$\alpha = G\frac{d\gamma}{dt} \pm \frac{d\nu_y}{dt} \ . \tag{32}$$

The two extreme cases of Eq. (30) are especially interesting. For a weak resonance with ϵ very small, there is no polarization loss. For a strong resonance with ϵ very large, the polarization is flipped by 180° but there is also no polarization loss. Anywhere in between these two cases there is depolarization. Thus the Froissart-Stora equation suggests that to minimize the loss in polarization one should somehow either make α very large or ϵ very small. We decided to "jump" the intrinsic resonances by using pulsed quadrupoles to rapidly shift the tune and thus make α very large, and to correct the imperfection resonances by using correction dipoles to make ϵ very small.[20]

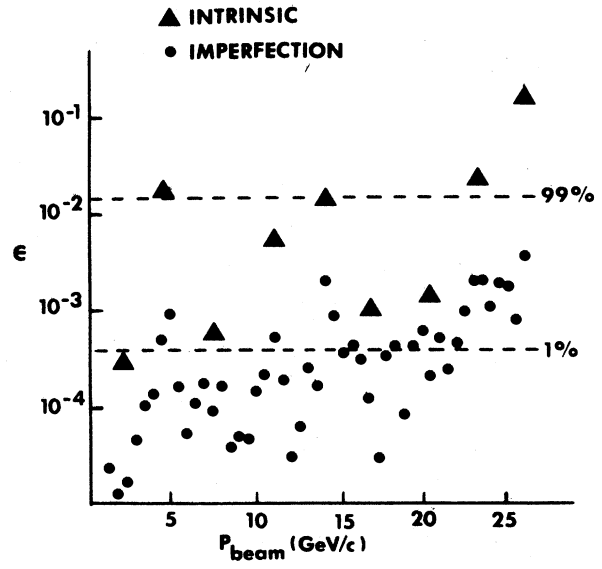

FIG. 12. AGS resonance strengths ϵ calculated by Courant and Ruth, assuming an AGS emittance of $10\pi/\gamma$ mrad mm and magnet errors of ± 0.1 mm. The intrinsic resonances are denoted by triangles and the imperfection resonances are denoted by dots. The 99% spin-flip level and 1% depolarization level are shown as dashed lines.

Intrinsic depolarizing resonances in the AGS

We "jumped" each intrinsic depolarizing resonance at the AGS by rapidly changing the tune just as each resonance was being passed,[20,31] and thus preserved the polarization. This rapid change in ν_y made $\alpha = G\,d\gamma/dt \pm d\nu_y/dt$ quite large and thus sharply reduced the depolarization in Eq. (30). The rapid tune shifts were produced by special fast quadrupole magnets; one quadrupole was installed in each of the 12 AGS superperiods as shown in Fig. 1. Sophisticated power supplies, which generated pulses with a maximum output of 2250 A at 15 000 V were connected to 10 of these quadrupoles. The field in each fast quadrupole had a 1.6-μsec risetime and then decayed back to zero in about 3 msec. Each quadrupole had a maximum field gradient of 11.7 kG/m.

Figure 13 is a diagram of one of the 12 pulsed quadrupole magnets installed inside the AGS. Each magnet was 19 cm wide by 16 cm high by 50 cm long with hyperbolic pole tips. To obtain a few μsec risetime these magnets had to be made of ferrite. Dipoles, such as fast kicker magnets, had been built of ferrite, but these were the first

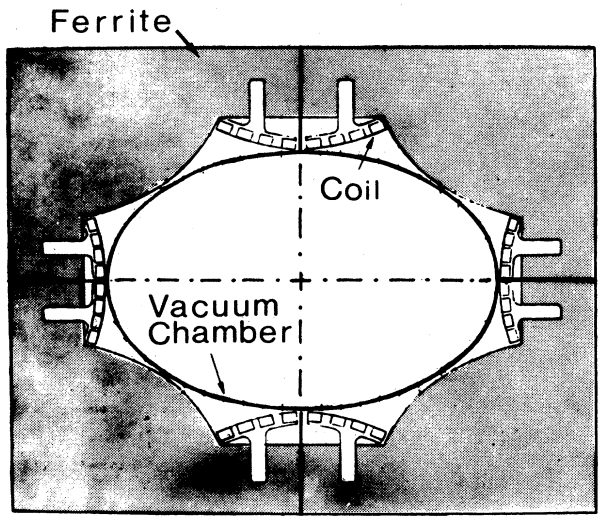

FIG. 13. A cross-sectional diagram of a pulsed quadrupole. Each quadrupole was about 19 cm wide by 16 cm high by 50 cm long.

ferrite quadrupoles.

There are several problems associated with constructing quadrupoles of ferrite. Ferrite costs about $50.00 per pound; moreover, it is considerably harder than steel and thus cannot be machined with normal tools. The ferrite also had to be machined with precise hyperbolic surfaces and is very fragile; if heated slightly during machining it shatters, as we experimentally determined. We obtained 1.7 tons of ferrite from the surplus ZGS rf acceleration cavity. We machined the ferrite at the University of Michigan on a new computer-controlled milling machine which allowed us to efficiently cut the hyperbolic pole faces with a precision of about ± 0.002 in. We ground the very hard ferrite using special diamond chip impregnated tools. The problem of overheating was solved by machining the ferrite in a bath of water.

We powered each quadrupole using a power supply[53] that was a rather complex and expensive system containing many ignitron and thyratron tubes; thus we have only been able to afford 10 of them. A simplified circuit diagram of one power supply is shown in Fig. 14. Each power supply produced a peak output power of over 20 MW with a peak current of 2250 A and a peak voltage of 15 000 V. The basic principle of the power supply was to trigger a thyratron tube which gave a 1.6-μsec risetime burst of current which then decayed with a falltime of about 20 μsec. As shown in Fig. 15, an ignitron tube was then triggered with a risetime of about 20 μsec which exactly matched the thyratron falltime and thus gave a smooth waveform. A capacitor bank with individual thyratron and ignitron switches allowed a 3-msec decay time in the pulse. The reason for this complexity was that the fast high voltage thyratrons were rather fragile and could not carry the high current for 3 msec.

As shown in Fig. 16, we obtained a risetime of 1.6 μsec for each quadrupole, which was acceptable. The pulsed quadrupoles also had to produce a good quadrupole field during the 1.6-μsec risetime. Thus we measured the field integral, $\int B\,dl$, as a function of the distance from the central axis during this fast risetime as shown in Fig. 17.

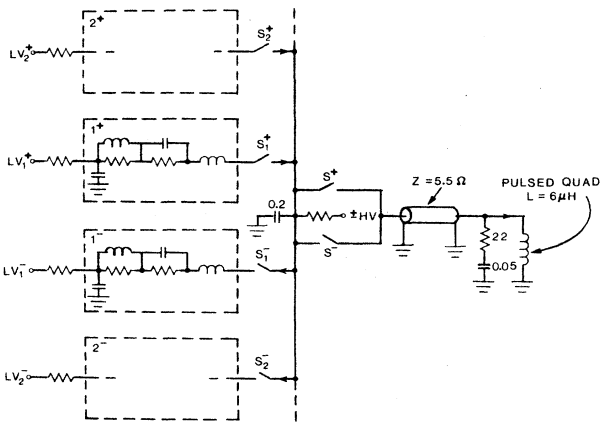

FIG. 14. Circuit diagram for each pulsed quadrupole power supply. The bipolar circuit contained thyratron and ignitron tubes which were triggered to give a fast pulse of current.

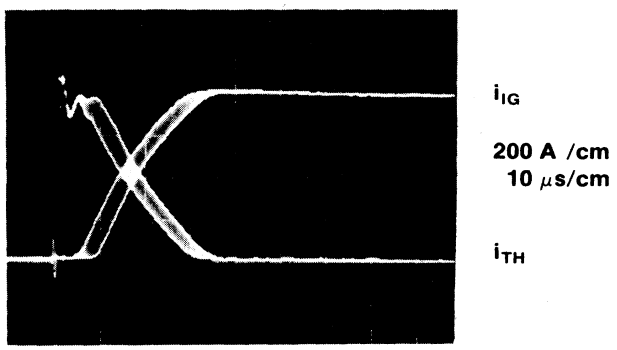

FIG. 15. Waveforms produced by thyratron and ignitron tubes. The thyratron had a fast risetime of about 1.6 μsec and a falltime of about 20 μsec. The ignitron risetime was matched to the thyratron falltime and the sum of the two pulses gave a current pulse into the pulsed quadrupole with a 1.6 μsec risetime and 3-msec falltime.

Any nonquadrupole field component would show itself as a deviation from the linear behavior, $B_x = by$ and $B_y = bx$.

A photograph of a fully assembled quadrupole is shown in Fig. 18. Notice the long white ceramic vacuum chamber inside the quadrupole. We experimentally determined that the eddy currents even in 0.005-in.-thick stainless-steel vacuum chambers increased the quadrupole's risetime to about 3 μsec, which was unacceptable. To avoid this problem, we built ceramic vacuum chambers and bonded them to the stainless-steel flanges using thin strips of monel metal. The monel was bonded to the ceramic using a special heat treatment. The inner surface of the ceramic beam tubes was coated with 0.0005 mm aluminum to prevent beam induced charge build-up, which might cause AGS beam instabilities.

The resonance jumping is demonstrated in Fig. 19, where ν_y is plotted against time in the acceleration cycle. The intrinsic resonance equation ($G\gamma = kP \pm \nu_y$) is shown along with the normal constant tune. We also show the tune shift when the quadrupoles were pulsed as the resonance was crossed; the tune then decayed back to its normal value and missed the tail of the resonance. Each in-

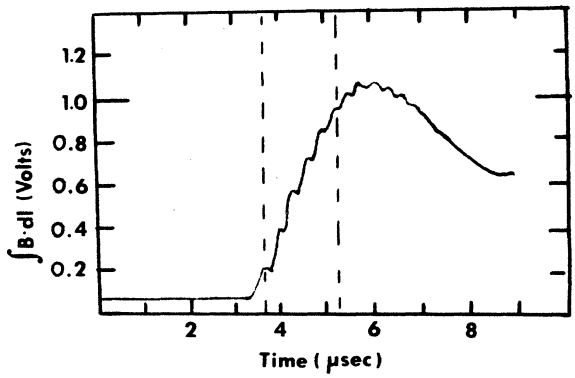

FIG. 16. Pulsed-quadrupole risetime. The integrated magnetic field in the quadrupole was measured with a long loop connected to a fast digital oscilloscope. The 10% to 90% risetime was about 1.6 μsec.

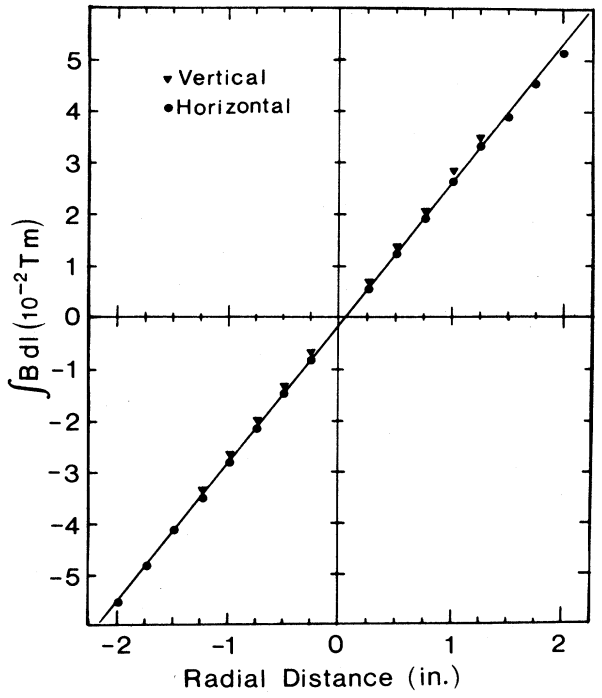

FIG. 17. Curve showing the linearity of a pulsed quadrupole. The measured integrated magnetic field is plotted against the distance from the quadrupole axis in the vertical and horizontal directions.

trinsic resonance was crossed during the fast risetime to minimize the resonance dwell time and thus to minimize the polarization loss. The firing time for each quadrupole pulse was first calculated from $G\gamma = kP \pm \nu_y$ using the AGS periodicity of 12, the measured tune of about 8.75±.01 and G, which is 1.792 85. Unfortunately, the exact γ of the trigger pulse was determined by the AGS Gauss clock whose calibration against the true AGS ring magnetic field occasionally shifted by up to 1%.

To maximize the polarization we varied the quadrupole start time around its predicted value while measuring the polarization. The quadrupole timing was then set in the middle of the experimental timing curve for each intrinsic depolarizing resonance. The timing curve for the $G\gamma = 48 - \nu_y$ intrinsic resonance is shown in Fig. 20. Many similar curves were obtained during the study of the AGS intrinsic depolarizing resonances up to 22 GeV/c. Table II lists measurements of the beam polarization before and after each intrinsic resonance; the ratio of these two measured polarizations is also compared[54] to the ratio predicted by Courant and Ruth.[49] The $12 - \nu_y$ and $24 - \nu_y$ intrinsic resonances were not jumped because they were too weak to be observed experimentally.

The jumped resonances are listed in Table III along with the high-voltage (HV) and the low-voltage (LV) setting of the fast quadrupole power supplies, the tune shift produced by these fast quadrupoles, and the quadrupole's

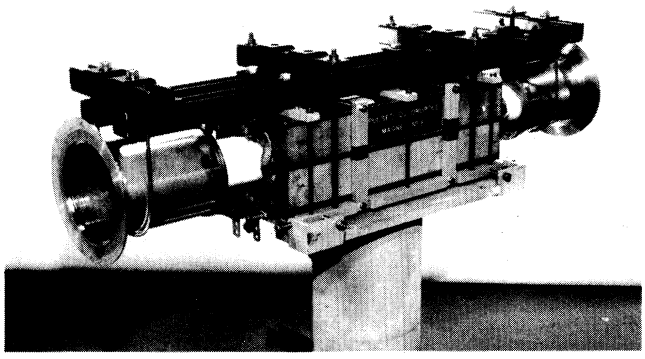

FIG. 18. Picture of an assembled pulsed quadrupole.

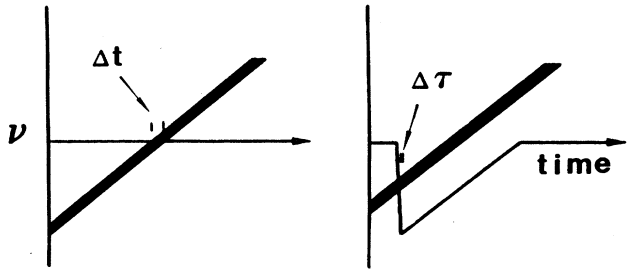

FIG. 19. The tune is plotted against the time in the acceleration cycle. The intrinsic resonance curve, $G\gamma = kP + \nu_y$, is shown as a thick line on the left along with the normal constant tune. On the right the resonance curve is shown along with the fast tune shift due to the pulsed quadrupoles. Note that the energy $m\gamma$ increases with time during the acceleration cycle.

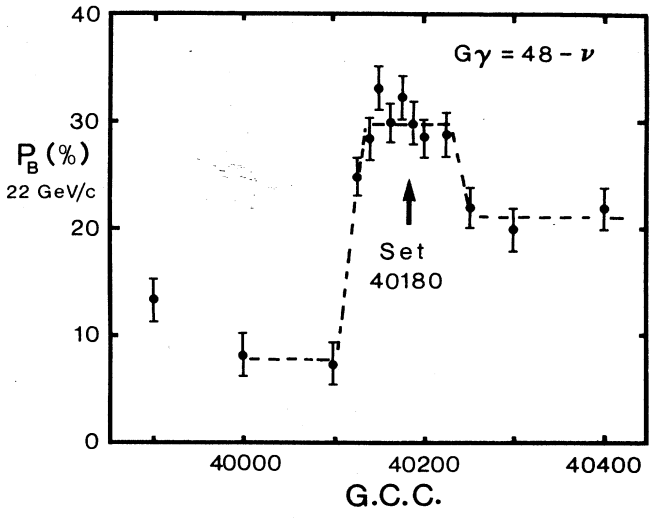

FIG. 20. Beam-polarization timing curve for the $G\gamma = 48 - \nu_y$ intrinsic resonance. The polarization measured at 22 GeV/c is plotted against the start time for the pulsed quadrupoles measured in Gauss-clock counts (GCC). The $G\gamma = 48 - \nu_y$ resonance occurs near 20.6 GeV/c. The start time where we set is shown.

TABLE II. Measured values of the polarization before and after each intrinsic depolarizing resonance. The ratio of these two polarizations is compared to the prediction of Courant and Ruth (Ref. 49). Negative values of the ratio correspond to spin flip. The error in the ratio was typically ±10%.

$G\gamma$	P_i	P_f	P_f/P_i	$(P_f/P_i)_{\text{theory}}$
$12-\nu_y$			100%	100%
$0+\nu_y$	17%	−10%	−59%	−100%
$24-\nu_y$			100%	97%
$12+\nu_y$	45%	3%	7%	−36%
$36-\nu_y$	−40%	24%	−60%	−99%
$24+\nu_y$	37%	33%	89%	93%
$48-\nu_y$	30%	21%	70%	84%

firing time in the AGS cycle in units of Gauss clock counts (GCC). Each GCC corresponds to a time of about 0.01 msec and an acceleration of about 0.5 MeV/c. We have also listed the width of the flat top of the timing curve for each intrinsic depolarizing resonance. We calculated the full width at half the maximum (FWHM) polarization measured in GCC.

A large tune shift by these pulsed quadrupoles could cause a beam blow-up resonance if ν_y crossed an integer or half-integer value. To avoid beam blow-up in the AGS, we thus had to keep $8.5<\nu_y<9$, which limited $\Delta\nu_y$ to about 0.25. We actually obtained slightly larger tune shifts without blow-up in using slow quadrupoles that already existed in the AGS ring. These slow quadrupoles were turned on slowly long before the resonance was crossed and then held at a constant tune shift of about 0.12 as shown in Fig. 21. After the fast quadrupole pulse has decayed to zero, the slow quadrupoles were turned off bringing the AGS back to its normal operating tune. Note that the slow quadrupoles changed the time at which each resonance occurred. The timing, amplitude, and width of the slow quadrupole pulses were varied to maximize the beam polarization.

The slow quadrupoles were particularly useful near 14 GeV/c in moving the $G\gamma=36-\nu_y$ intrinsic resonance away from the $G\gamma=27$ imperfection resonance. These two resonances were normally so close that they apparently overlapped and caused a serious polarization loss which could not be overcome by either jumping $G\gamma=36-\nu_y$ or correcting $G\gamma=27$. Overlapping resonances cannot be treated by the standard theoretical approaches to depolarizing resonances[45] and for some time it was impossible to accelerate polarized protons above 14 GeV/c. By using the slow quadrupoles to separate these two resonances we significantly reduced the polarization loss around 14 GeV/c as shown in Fig. 22. Understanding and somehow separating these two overlapping resonances was perhaps the most unexpected and difficult problem in the entire polarized beam project.

The slow quadrupoles also reduced the beam emittance growth caused by the dipole fields produced by the fast quadrupole pulses. The reduction in emittance growth improved the extraction efficiency.

Another possible source of depolarization was the proximity of the AGS flat top to some normally weak depolarizing resonance. Since $G\,d\gamma/dt$ is very small on the flat top, even a weak higher-order resonance might cause significant depolarization. Therefore, we experimentally measured the polarization while varying the flat top of the AGS magnet cycle. A typical flat top energy sweep is shown in Fig. 23. At each extraction energy the AGS flat top was set to the field value that maximized the polarization.

Imperfection depolarizing resonances in the AGS

The AGS imperfection depolarizing resonances were overcome by making ϵ small. We corrected the kth harmonic of the imperfection fields at each $G\gamma=k$ resonance by generating a pulsed wave of horizontal correction field of the form

$$B_k(\theta)=\alpha_k\sin(k\theta)+\beta_k\cos(k\theta)\ . \tag{33}$$

TABLE III. Fast quadrupole high voltage (HV) and low voltage (LV) for jumping the intrinsic depolarizing resonances. Also listed for each resonance are the tune shift $\Delta\nu_y$ produced by these fast quadrupoles, and the trigger time and the flat top width of each timing curve in Gauss-clock-count units (GCC).

$G\gamma$	HV (V)	LV (V)	$\Delta\nu_y$	Trigger time (GCC)	Flat top width (GCC)
$0+\nu_y$	3200	450	−0.24	8340	230
$12+\nu_y$	4716	800	−0.17	21130	150
$36-\nu_y$	11943	1986	0.28	27960	250
$24+\nu_y$	6357	1468	−0.14	33500	250
$48+\nu_y$	7172	1492	−0.11	40180	150

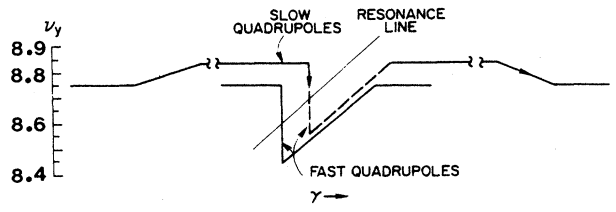

FIG. 21. The AGS tune is plotted against energy (γ) in the acceleration cycle. The fast quadrupole tune shift is shown both with and without the slow quadrupoles being used.

Each amplitude, α_k and β_k, was determined experimentally by maximizing the polarization while independently varying α_k and β_k. The horizontal magnetic field in Eq. (33) was produced by 95 correction dipoles (8 dipoles in each of the 12 superperiods, with one dipole missing) which already existed in the AGS ring. However, these dipoles required new fast power supples and a sophisticated new computer control system with complex software to successfully correct the many imperfection resonances which occurred about every 0.52 GeV. The new pulsed power supplies needed ±6-A current capability with a 100-Hz repetition rate to give about 50 pulses per AGS cycle with a 3-msec risetime, a 1.5-msec fall-

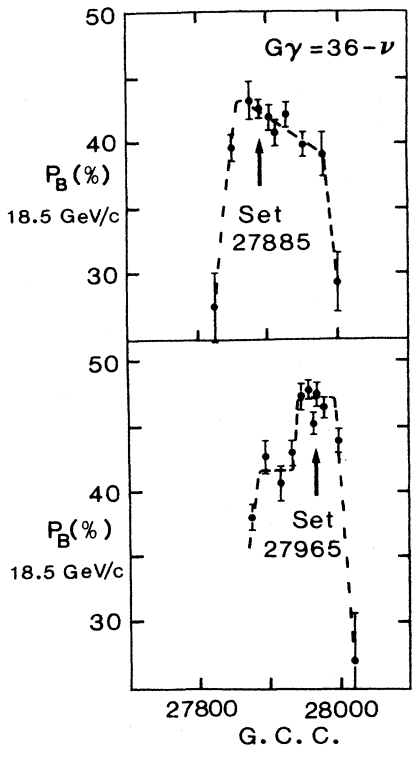

FIG. 22. The AGS beam polarization measured at 18.5 GeV/c is plotted against the trigger time for the pulsed quadrupoles before (upper) and after (lower) the $G\gamma = 36 - \nu_y$ intrinsic resonance was moved away from the $G\gamma = 27$ imperfection resonance using the slow quadrupoles.

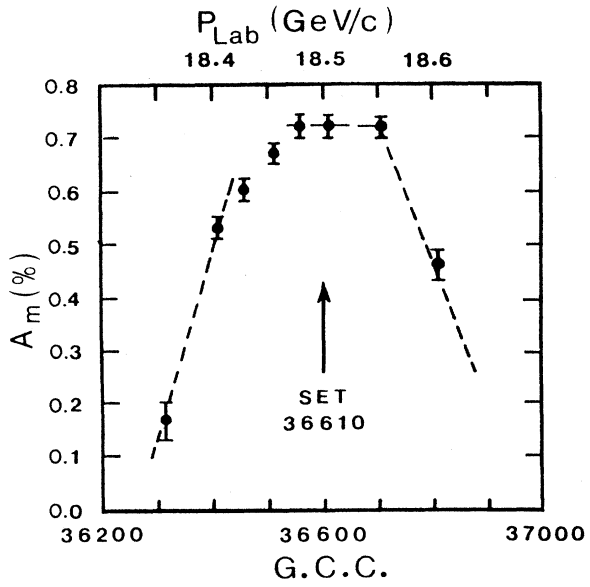

FIG. 23. Flat top energy sweep. The maximum asymmetry A_m measured by the internal polarimeter is plotted against the AGS flat top magnetic field measured in Gauss-clock counts (GCC).

time, and a 3-msec flat top.

The AGS correction dipole power supply system was divided into six separate modules, each having 16 magnet regulators with individual controls and dc power supplies. The regulator for each magnet consisted of a power amplifier and the low level electronics mounted on separate printed circuit cards. The power amplifier was configured in an H circuit as shown in Fig. 24, to produce a bipolar current. A dual power supply system used a high-voltage start supply for a fast risetime and then switched over to a lower-voltage regulator supply to minimize the transistor power dissipation. The positive and negative regulator circuits consisted of five parallel-connected power metal-oxide semiconductor field-effect transistors (MOSFET's) mounted on water-cooled heat sinks. The start and regulate selector switches consisted of two parallel connected MOSFET's. The gate-source voltages were set within ±10% of each other to ensure proper current sharing, and a shunt was used for the feedback and current monitoring. The voltage developed across a diode in series with each dipole provided the polarity information which was transmitted via opto-isolators.

Each low-level electronics card provided separate control for two power amplifiers. During the 4-msec off time between each pulse a 7-bit magnitude command and a 1 bit polarity command from the control computer were converted into a power amplifier reference signal by a digital-to-analog converter and two operational amplifiers. The start supply switch was controlled by a comparator that opened the switch when the final current was reached and minimized current overshoots by preventing the switch from closing for currents smaller than 3 A.

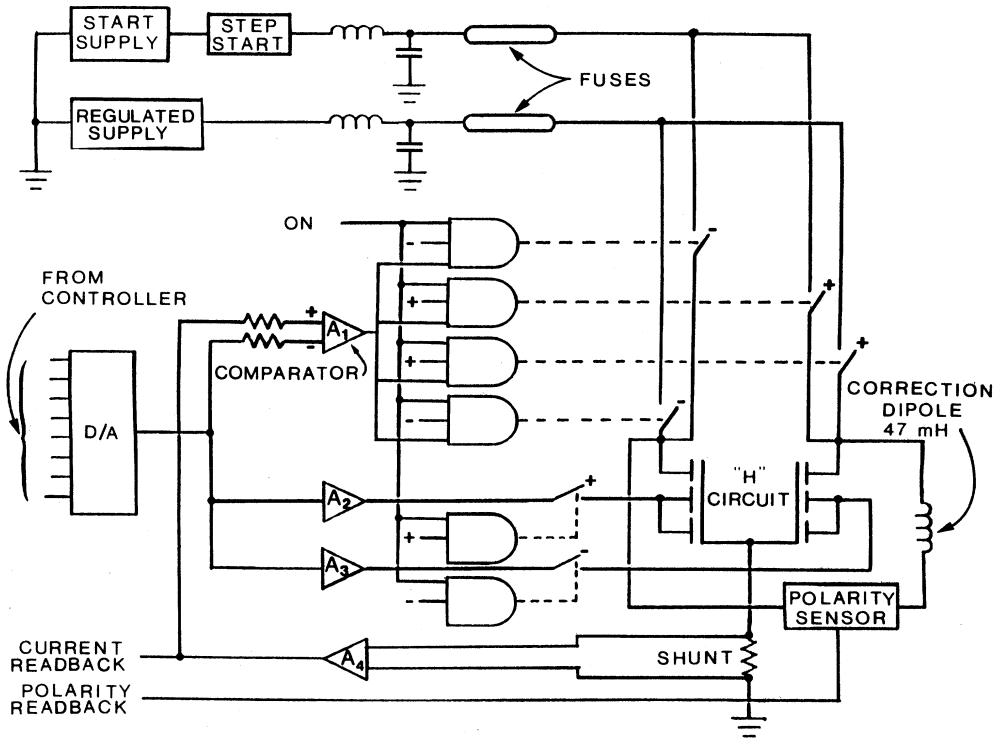

FIG. 24. Schematic of a dipole power supply.

Each correction dipole pulse was timed using the AGS Gauss clock. Unfortunately, the Gauss-clock calibration once shifted by about 1% so that the 3-msec-wide correction pulse no longer bracketed the appropriate imperfection resonances at high energies. It was then impossible to correct the imperfection fields at those resonances. We therefore had to modify the timing of some of the correction dipole pulses using the GCC calibration obtained from the intrinsic depolarization resonances and a second GCC calibration.[54] The higher-energy imperfection resonances were then successfully corrected.

Since the polarized beam was accelerated up to 22 GeV, we were able to study the effects of 39 imperfection depolarizing resonances ($G\gamma=3,4,\ldots,41$). The $G\gamma=3,4,5,6$ depolarizing resonances had no measurable depolarization and the pulsed dipoles were not used for these resonances. The $G\gamma=7,8,\ldots,41$ imperfection resonances were each corrected and studied in considerable detail. For each $G\gamma=k$ resonance we ran correction curves by measuring the beam polarization while varying the current in the pulsed dipoles which were preprogrammed to give the kth harmonic of the horizontal magnetic field. The correction curves for the $G\gamma=9$ imperfection resonance are shown in Figs. 25 and 26. The polarization was especially sensitive to this $G\gamma=9$ resonance because 9 was so close to the AGS tune of 8.75. Calculations with estimated misalignments of ± 0.1 mm indicated that the AGS correction dipoles had enough strength to correct the random horizontal fields of all AGS imperfection resonances except $G\gamma=60$ at 31.4 GeV/c (Refs. 30 and 55).

The experimental study of the 35 imperfection depolarizing resonances is summarized in Fig. 27. For each $G\gamma=k$ resonance, the parameters of interest are α_{0k} and S_k for a sine correction curve and β_{0k} and C_k for the cosine correction curve. The parameters α_{0k} and β_{0k} are those values of the correction dipole amplitudes, α_k and β_k, which maximized the polarization as shown in Figs.

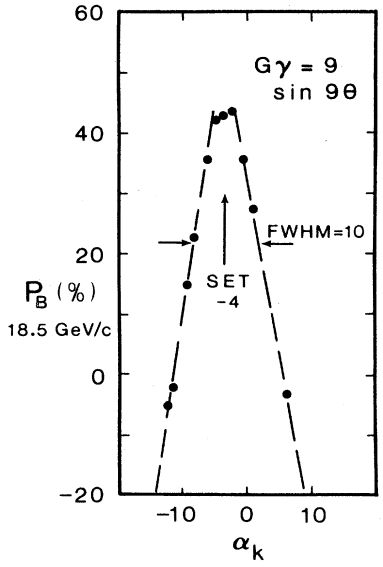

FIG. 25. The ninth harmonic sin(9θ) amplitude-correction curve for the $G\gamma=9$ imperfection depolarizing resonance. The beam polarization measured at 18.5 GeV/c is plotted against the dipole's ninth sine amplitude, α_9, in arbitrary units.

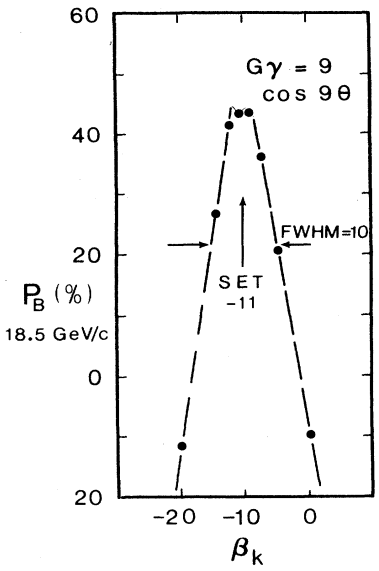

FIG. 26. The ninth harmonic cos(9θ) amplitude correction curve for the $G\gamma=9$ imperfection depolarizing resonance. The beam polarization is plotted against the dipole's ninth cosine amplitude β_9 in arbitrary units.

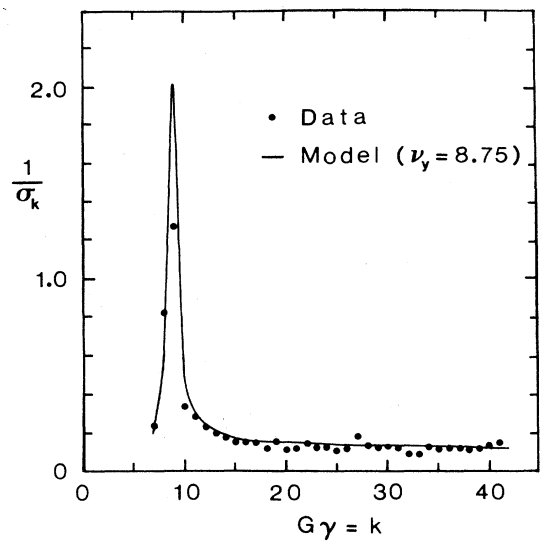

FIG. 27. The measured strength $1/\sigma_k$ of each $G\gamma=k$ imperfection depolarizing resonance is plotted against k.

25 and 26. The α_{0k} and β_{0k} are proportional to the current in the 95 dipoles needed to fully correct the imperfection resonance. S_k and C_k are, respectively, the full width at half maximum of the sine and cosine curves. All these parameters as well as $A_{0k}\equiv\sqrt{\alpha_{0k}^2+\beta_{0k}^2}$ are listed in Table IV for the 35 imperfection resonances that were corrected. The data are mostly in good agreement with simple arguments which suggest that the ratio C_k/S_k should normally be equal to 1. In the special case, when $k=12n$, then k is an integer multiple of the AGS periodicity and C_k/S_k should then be approximately equal to 2 (Refs. 54 and 55), which agrees fairly well with the data in Table IV.

We analyzed the data by fitting each $G\gamma=k$ correction curve to a Gaussian of the form

$$\frac{P_k}{P_{0k}}=2\exp\left[-1.15\left[\frac{\alpha_k-\alpha_{0k}}{S_k}\right]^2\right]-1\ , \tag{34}$$

where P_{0k} is the initial polarization and S_k is defined by setting $P_k/P_{0k}=\frac{1}{2}$ at the point where

$$\alpha_k=\alpha_{0k}\pm\frac{S_k}{2}\ . \tag{35}$$

A least-squares-fitting program evaluated each α_{0k}, S_k, their errors, $\Delta\alpha_{0k}$ and ΔS_k, and the χ^2 of the fit for the sine correction curve at each k. A similar fitting program was used for the cosine correction curves. The Gaussian fit generally gave χ^2 close to 1; when χ^2 was greater than 1, we increased the error in S_k or C_k by χ in Table IV.

We then calculated each measured resonance strength $1/\sigma_k$ by using the widths of each imperfection resonance curve, S_k and C_k, in the equation

$$\sigma_k\equiv\tfrac{10}{127}\sqrt{S_kC_k}\ . \tag{36}$$

Note that 127 dipole controller counts correspond to 10 A. We then compared these σ_k to the predictions of the simple Terwilliger model,[56] which assumes that the imperfection fields drive simple-harmonic betatron oscillations. The model approximates the AGS with a smooth constant-gradient accelerator with $\nu_y=8.75$, and gives

$$\sigma_k=8.4\left|1-\left[\frac{\nu_y}{k}\right]^2\right|\ \text{A}\ . \tag{37}$$

The depolarization should be strongest when the quadrupole fields and the driven betatron amplitudes were largest, which occurred when k was near ν_y. As shown in Fig. 27 the model is in reasonable agreement with the experimental $1/\sigma_k$. The data show quite clearly that the AGS was very sensitive to the ninth harmonic, and that the resonance strength decreased rapidly as k moved away from $\nu_y=8.75$.

Until now we have discussed the intrinsic resonances and the imperfection resonances as being totally independent. However, when a horizontal imperfection field deflected a proton vertically, the proton then entered the strong horizontal quadrupole focusing fields with the normal AGS periodicity. The imperfection fields and the quadrupole fields could then beat against each other and generate "beat" imperfection depolarizing resonances.[56] The periodicity of the beat resonance due to the k' Fourier component of the magnetic imperfection fields was found by substituting $\cos(k'\theta)$ for $\cos(\nu_y\theta)$ in Eq. (18) which describes the vertical betatron oscillation. The beat resonances therefore occurred at

$$G\gamma=k=nP\pm k'\ . \tag{38}$$

The spike in Fig. 27 may be thought of as the strong $k'=9$ beat resonance with $nP=0$. Extending the model to the $nP\neq0$ case gives[57]

$$\sigma_{k'}=\frac{8.4}{r}\left|\left(\frac{k'}{\nu_y}\right)^2-1\right| \mathrm{A}\ , \tag{39}$$

where ν_y is still typically 8.75 and r is a measure of the relative strength of the nP resonance with respect to the $nP=0$ resonance obtained from Courant and Ruth.[49] Figure 28 shows the experimentally determined strengths of the beat resonances, $1/\sigma_{k'}$, along with the predictions of the model, which are in fair agreement with the data. The data clearly indicate that the AGS was very sensitive to the ninth harmonic even when $G\gamma$ was far from 9.

The total correction amplitudes A_{0k} are plotted in Fig. 29 for both the simple imperfection resonances and the beat resonances. Notice that the $G\gamma=12$, 24, and 36 imperfection resonances were particularly strong. This suggests that there was some type of periodic systematic error in the AGS ring magnets. Note also that these A_{0k} may change from year to year as the AGS ring magnets move by up to a millimeter along with Long Island. However, the resonance strengths $(1/\sigma_k)$ should be an unchanging property of the AGS ring lattice.

AGS control system

The acceleration of polarized protons in the AGS required many complex computer controlled devices such as three polarimeters and the pulsed quadrupoles and correction dipoles, which each required both timing and amplitude adjustment to handle the many depolarizing resonances. The complexity of the problem can be seen in Fig. 30 which shows the pulsed quadrupoles firing 3 times to jump 3 intrinsic depolarizing resonances and the correction dipoles pulsing 24 times to correct the imperfection resonances while the AGS ring magnets guided the polarized protons to 16.5 GeV/c. These devices required many complex controllers, and thus we decided to use microprocessor-based designs. Adding these controllers to the 10-year-old AGS control system required a considerable increase in communications bandwidth and flexibility; therefore we installed a new local area network in the computer control system using distributed intelligence.

A broad-band local-area network called RELWAY (Ref. 58) was installed at the AGS using commercial

TABLE IV. Experimentally determined correction amplitudes and widths of the $G\gamma=k$ imperfection depolarizing resonances. The units are dipole controller counts (dcc); 127 dcc corresponds to 10 A in the dipoles.

k	α_{0k}	β_{0k}	A_{0k}	S_k	C_k
7	5	0	5	53±3	58±1
8	−8	−5	9	17±1	15±1
9	−4	−11	12	10±1	10±1
10	−2	−2	3	38±6	38±2
11	−10	−2	10	46±2	46±1
12	40	−9	41	41±2	73±2
13	−10	5	11	68±2	65±2
14	5	−13	14	73±3	78±2
15	0	−15	15	92±4	79±3
16	−5	−10	11	85±1	90±3
17	−10	−5	11	88±5	79±2
18	5	20	21	122±8	89±2
19	10	−10	14	83±6	85±8
20	−2	−33	33	122±5	102±8
21	−10	−10	14	114±4	120±5
22	−10	−5	11	105±5	81±3
23	25	15	29	120±2	99±4
24	−5	40	40	86±3	105±6
25	20	12	23	120±5	109±5
26	−5	−10	11	116±5	100±6
27	0	0	0	28±7	56±4
28	0	0	0	90±13	90±12
29	5	−3	6	100±6	100±10
30	5	0	5	100±6	100±9
31	−5	0	5	100±5	120±5
32	20	0	20	128±6	140±30
33	0	−30	30	174±20	127±15
34	−12	−40	42	104±7	92±6
35	20	−60	63	120±3	120±5
36	−40	−60	72	80±7	146±8
37	−20	−35	40	110±4	100±3
38	60	45	75	96±6	110±8
39	100	−50	112	120±9	120±6
40	30	20	36	92±45	84±45
41	−17	9	19	86±4	86±3

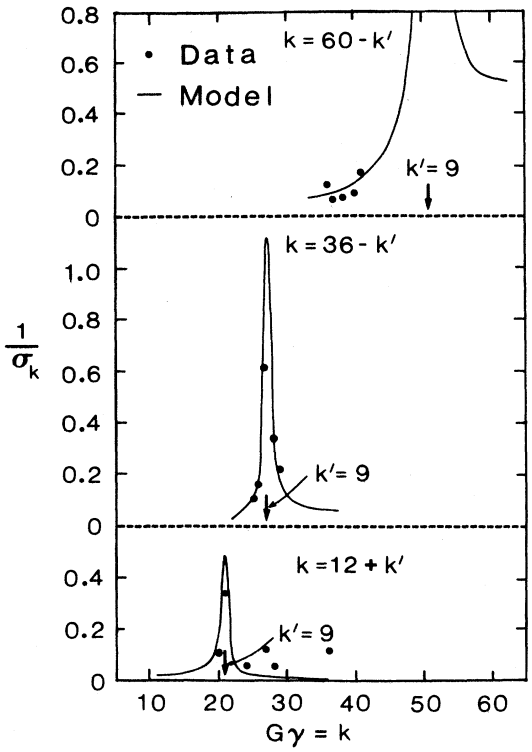

FIG. 28. The measured strength $1/\sigma_k$ of each $G\gamma=k$ beat imperfection depolarizing resonance is plotted against k. The horizontal correction fields have periodicity k'. In the upper curve we studied the beat against the $5P=60$ periodicity, in the middle curve we beat against the $3P=36$ periodicity and in the lower curve we beat against the $1P=12$ periodicity.

cable-TV hardware and using 2 km of dual coaxial cables for communications. A digital control channel with 4-MHz bandwidth was implemented on this network using carrier-sense-multiple-access–collision-avoidance (CSMA-CA) protocol. This channel was interfaced to the DEC-system-10 host computer which controls the normal AGS hardware. The channel was then connected to many RELWAY stations which were each attached to one or more device controllers. Each station polled its device controllers for readbacks at prescribed times during each AGS cycle, and upon request reported on device performance to the host computer.

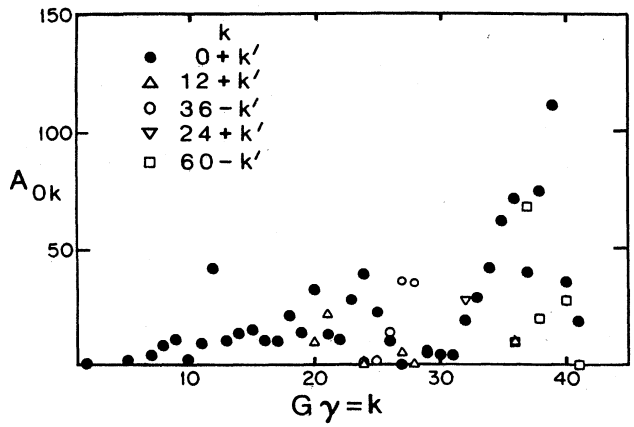

FIG. 29. The measured correction amplitude A_{0k} of each $G\gamma=k$ imperfection and beat resonance is plotted against k.

Ten of the 12 pulsed quadrupole magnets had a nearby power supply which contained capacitor banks that were discharged through thyratrons and ignitrons. Each set of 10 capacitor banks was charged in common by a centrally located voltage supply. A high-voltage (HV) supply and a low-voltage (LV) supply were used for each quadrupole pulse as shown in Fig. 14. The HV supply produced the fast 1.6-μsec risetime of the current pulse and the LV supply produced the 3-msec decay time. For each $G\gamma=nP\pm\nu_y$ intrinsic resonance the quadrupole magnet controllers measured the following data: high and low voltage, both at the voltage supplies and at the capacitor banks in each quadrupole power supply. Moreover, the current in each quadrupole was measured at 5 times during each current pulse. These data were periodically returned to a monitoring program in the host computer, which triggered an alarm if any abnormality occurred. Using a standard control program, the operator could turn individual resonance pulses on or off, adjust the timing of each pulse relative to the Gauss clock, adjust the high- and low-voltage setpoints for each pulse, and turn individual quadrupole power supplies on or off.

We overcame the imperfection resonances by using 95 air-core dipole magnets to correct the horizontal imperfection fields. These magnets were pulsed to correct the appropriate horizontal harmonics at each $G\gamma=k$ resonance. A system of regulators was constructed to pulse the 95 dipole magnets up to 50 times in each AGS cycle. The regulators stored individual preprogrammed setpoints for each magnet for each kth harmonic pulse and measured the current in each magnet for each pulse. Setpoints were specified as 8-bit bipolar quantities with ±10 A maximum current in each dipole. During the normal

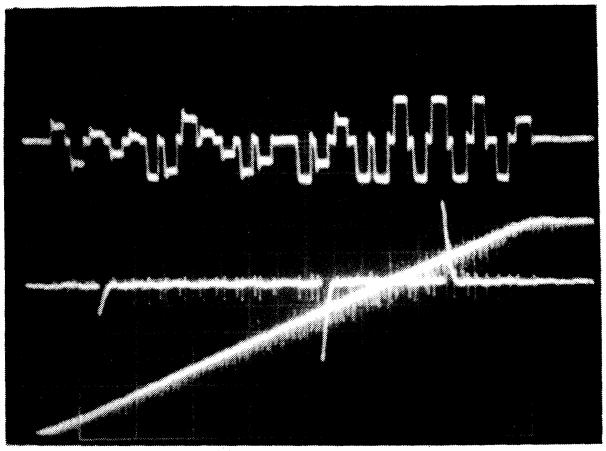

FIG. 30. Oscilloscope trace showing the pulsed quadrupoles firing three times and the dipoles being pulsed 24 times as the rising AGS magnet field guides the polarized protons to 16.5 GeV/c.

AGS acceleration cycle an imperfection resonance was crossed every 10 msec, and thus the regulators were engineered for pulses with nominal 3-msec widths and rise-times and 1.5-msec falltimes. The $50\times95=4750$ setpoints, which produced the $k=1$ to 50 harmonics, were stored in the regulators after being transferred from programs in the host computer. The current readbacks were periodically monitored in the host computer which issued appropriate alarms to the operator. Control programs in the host computer permitted the operator to specify corrections for each $G\gamma=k$ imperfection resonance in terms of Fourier components of field harmonics, with up to three harmonics per resonance. The host computer calculated individual dipole magnet setpoints from these harmonics and then sent the setpoints to the regulators. Using a standard control program, the operator could turn individual pulses on or off, adjust their timing and width relative to the Gauss clock, select the harmonics to be generated for each pulse, and adjust the strength of each harmonic.

Each polarimeter was interfaced to conventional fast logic and CAMAC modules. Each CAMAC crate was connected to a LSI-11 microcomputer which was connected to a RELWAY station. A monitoring program in the host computer periodically polled the polarimeters and posted each polarization and error estimate on a video display available in the AGS main control room and at each experiment. This information was also distributed to each experiment via a CAMAC interface. Using a standard control program, the operator could begin a new measurement of the polarization, pause and then resume data collection, adjust the analyzing power, and control the timing gates for the fast logic.

Polarimeters

Three polarimeters[59] were used to measure the beam polarization, before injection into the AGS, during the acceleration cycle in the ring, and after extraction. We determined the polarization by measuring the left-right asymmetry in the horizontal scattering plane which was normal to the vertical polarization vector. The beam polarization P_B was obtained from the equation[59a]

$$P_B=\frac{1}{2A}\left[\frac{L\uparrow-R\uparrow}{L\uparrow+R\uparrow}-\frac{L\downarrow-R\downarrow}{L\downarrow+R\downarrow}\right], \tag{40}$$

where A was the analyzing power of each polarimeter while $L\uparrow$ and $R\uparrow$ were the number of spin-up particles scattered to the left and right, respectively. Note that the polarization of the AGS beam was flipped between up and down ($\uparrow$ and $\downarrow$) on alternate pulses.

The 200-MeV polarimeter was placed just downstream of the linac. It measured the beam polarization just before injection into the AGS main ring. The 200-MeV polarimeter, as shown in Fig. 31, consisted of two independent polarimeters each containing a left arm and a right arm. Each arm contained two scintillation counters in series. Each polarimeter measured the asymmetry in

$$p+{}^{12}\mathrm{C}\rightarrow p+\text{anything} \tag{41}$$

at 200 MeV, one at a scattering angle of 12° and the other at a scattering angle of 16°. The two measurements were converted into polarizations using Eq. (40) and then averaged to give the final polarization. The 0.25-in.-thick final counters of the 12° polarimeter were 1 in.$\times$0.5 in. ($h\times v$) and were 30 in. from the target. The horizontal position of the 0.015-in.-diam carbon filament target was adjusted to optimize the count rate and minimize the systematic asymmetry.

The polarimeter was calibrated using the 200-MeV polarized proton beam at the Indiana University Cyclotron Facility, and the analyzing powers of the 12° and 16° arms were found to be 0.620 ± 0.004 and 0.511 ± 0.004, respectively.[60] The polarimeter provided a fast, absolute measurement of the beam polarization with a 2% statistical precision in about 60 AGS pulses. The beam loss due to the thin carbon target was only about 1% and thus the 200-MeV polarimeter could continuously monitor the beam polarization just before injection into the main ring. The 200-MeV beam polarization was typically (75 ± 2)%.

The internal polarimeter was placed inside the AGS ring to rapidly measure the polarization during the acceleration cycle by observing the left-right asymmetry in proton-proton scattering from a nylon target. It was the main polarimeter used in correcting and jumping the various depolarizing resonances.

The internal polarimeter is shown in Fig. 32. The target was a spooling nylon fishline about 1 km long and 0.004 in. diam. The fishline was swung into the beam every AGS pulse while being spooled at 100 cm/sec to minimize heat and radiation damage. We used a sliding mechanism to adjust the position of the target with respect to the beam to optimize the count rate and minimize the systematic asymmetry. The scattered particles were detected by two identical recoil arms, each arm consisting of 3 scintillation counters in coincidence. Each arm detected the reaction products in proton-proton scattering at 77° where $P_\perp^2$ was about 0.15 (GeV/c)^2. The solid angle was defined by the 1.5-cm-thick final counters which were 5 cm$\times$7.5 cm($h\times v$) in size and were placed 114 cm from the target. The elastically scattered protons, which had about 400 MeV/c for P_{Lab} above 12 GeV/c, were selected by placing aluminum absorber wedges in front of the final counter to range out the lower-energy inelastic protons. However, the effective analyzing power was only about 40% of the elastic

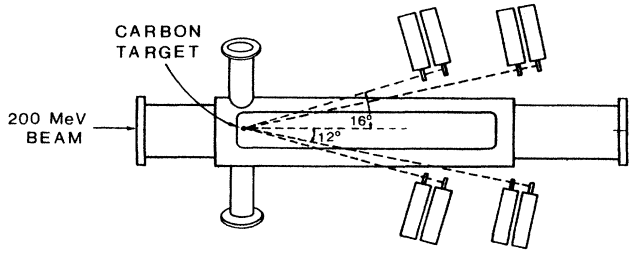

FIG. 31. Layout of the 200-MeV polarimeter. The polarized H^- ions scatter in the thin carbon target. The left-right asymmetry in 200-MeV p-carbon scattering is measured by the identical L and R scintillator telescopes at both 12° and 16°.

analyzing power because of unrejected background. Thus while the polarimeter could rapidly measure the polarization, it was not absolutely calibrated and had to be periodically calibrated against the high-energy polarimeter.

The internal polarimeter could be electronically gated to measure the beam polarization at up to five different times during the AGS acceleration cycle or on the flat top. This let us simultaneously scan the polarization at many energies. Such an energy scan is shown in Fig. 33 which clearly demonstrates the polarization loss near the $G\gamma=36-\nu_y$ and $G\gamma=27$ resonances. Typically, one gate was set just before a depolarizing resonance and another gate just after it; the depolarizing resonance was then corrected or jumped until the polarizations measured in the two gates were equal.

The high-energy polarimeter was in the D line of the extracted AGS beam about 20 m upstream of the polarized proton target. As shown in Fig. 34, the polarimeter contained two symmetrical double-arm spectrometers, which each consisted of a forward arm and a recoil arm with magnets for momentum analysis and scintillators to detect the scattered protons. By measuring the angle and momentum of both outgoing protons we could clearly identify proton-proton elastic scattering events from the liquid-hydrogen target. Each recoil arm had a small C-

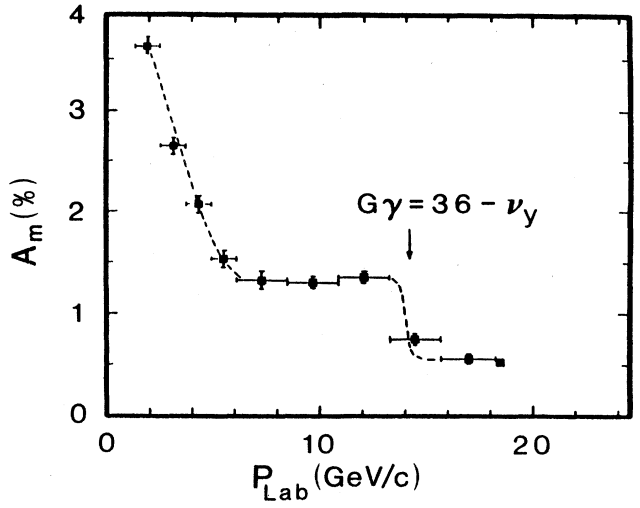

FIG. 33. A polarization energy scan. The asymmetry measured by the internal polarimeter A_m is plotted against P_{Lab}. Notice the sharp polarization loss near the $G\gamma=36-\nu_y$ resonance and the nearby $G\gamma=27$ resonance. This loss was studied in detail as shown in Fig. 22.

type horizontal steering magnet followed by a 28.3° vertical bending magnet. Each forward arm contained three dipole magnets for horizontal steering and bending. This arrangement of steering and bending magnets let us adjust the polarimeter to the appropriate angles and momenta of p-p elastic scattering at $P_\perp^2=0.3$ (GeV/c)^2 at incident momenta of 6 to 22 GeV/c without moving any magnets or scintillators.

The polarimeter gave a 1% precision measurement of the beam polarization in 30 min with a typical AGS beam intensity of 5×10^9 polarized protons every 2.2 sec. We selected the elastically scattered protons from the liquid-hydrogen target using the six scintillation counter hodoscopes in the forward and backward arms. Table V lists the high-energy polarimeter counter sizes and their distances from the liquid-hydrogen target. A typical elastic event in the left arm was defined by a sixfold coincidence $L_1L_2^uL_3L_4^dL_5L_6^d$, where u and d refer to the up and down vertical hodoscope channels which determined coplanari-

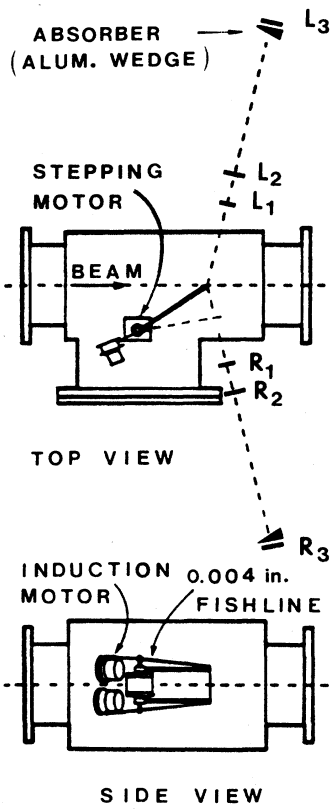

FIG. 32. Layout of the internal polarimeter. The polarized protons in the AGS scatter from the 0.004-in.-diameter nylon string. The left-right asymmetry is measured by the identical L and R scintillator telescopes.

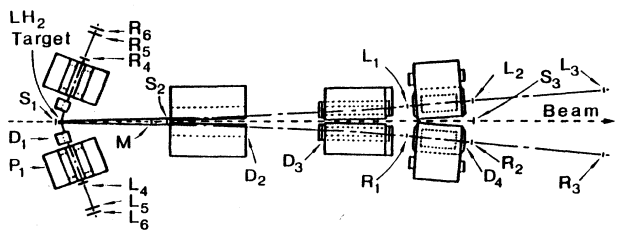

FIG. 34. Layout of the high-energy polarimeter. The polarized proton beam scatters from the liquid-hydrogen target. The left-right asymmetry in p-p elastic scattering is measured by the identical L and R double-arm spectrometers.

ty. The electronic circuitry for the left polarimeter is shown in Fig. 35. The accidental events were estimated by the coincidences in the delayed circuit where the recoil arm was delayed by 230 nsec with respect to the forward arm. The 230 nsec corresponds to the time between two successive rf bunches in the AGS ring.

The high-energy polarimeter was normally tuned by running magnet and timing curves with the AGS unpolarized proton beam as shown in Figs. 36 and 37. These curves let us properly set each magnet current and electronic logic delay time and helped to minimize the systematic asymmetry in the polarimeter. The small background off the peak in Fig. 37 shows that the accidental events were less than 1%. Moreover, the near equality of the left and right events in Fig. 36 indicates that the systematic asymmetry in the polarimeter was not too serious. The effect of this asymmetry was almost eliminated by flipping the beam spin every pulse.

We monitored the beam intensity at the liquid-hydrogen target using the M counter telescope, which counted the secondary particles produced in the target at a vertical angle of about 30°. We monitored the angle and position of the beam using the segmented-wire ion chambers (SWIC's) S_1, S_2, and S_3 shown in Fig. 34. The beam's size at the hydrogen target was typically 10×8 mm ($h\times v$) and its angular divergence was typically 1.2×1.0 mrad($h\times v$) (Ref. 61). The beam was centered on the hydrogen target to within ±0.4 mm and ±0.1 mrad.

To obtain the beam polarization from the measured asymmetry, we must know the analyzing power for p-p elastic scattering.[11–13,17–19,62–66] The measured analyzing power for p-p elastic scattering at $P_\perp^2=0.3$ (GeV/c)^2 is plotted against $P_{\rm Lab}$ in Fig. 38. While a $1/P_{\rm Lab}$ fit is fairly good between 2 and 6 GeV/c, our new data indicate that there is a deviation from this fit between 10 and 20 GeV/c. This deviation was also suggested by the internal polarimeter energy scan shown in Fig. 33. The measured internal polarimeter asymmetry was constant above 6 GeV/c except for the polarization loss around 14 GeV/c. Since the AGS polarization certainly does not increase with energy, this flatness indicates that the analyzing power may be constant.

We determined the analyzing power A for the high-energy polarimeter at 13.3 GeV/c by using our polarized proton target and spectrometer to measure A in

TABLE V. Counter sizes and positions of the high-energy polarimeter.

Counter	Size $h\times v$ (in.)	Number	Total size $h\times v$ (in.)	Distance to H_2 target (in.)
R_1, L_1	3×2.5	1		420
R_2, L_2	3.5×2	2	3.5×3	500
R_3, L_3	4×3	1		730
R_4, L_4	6×4.5	2	6×8	92
R_5, L_5	6×10	1		114
R_6, L_6	6×5	2	6×10	142

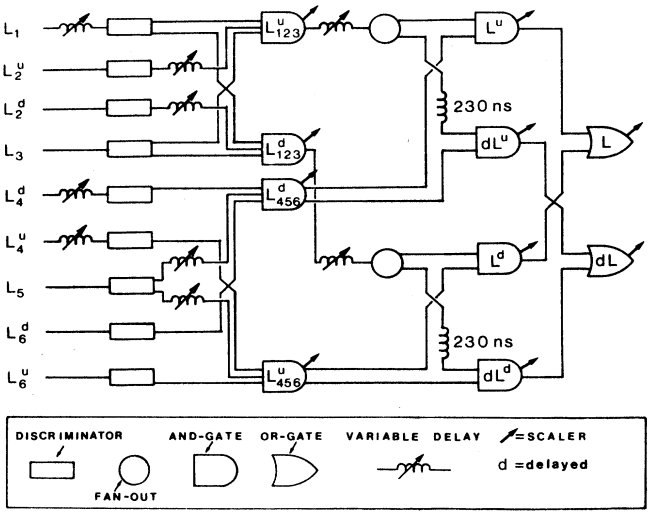

FIG. 35. Electronic-logic diagram of the left arm of the high-energy polarimeter. The right arm has an identical circuit.

$p_\uparrow+p_\uparrow\rightarrow p+p$ at $P_\perp^2=1.5$ (GeV/c)^2. We then found the beam polarization by noting that the analyzing powers must be equal when measured with either the beam or the target polarized. Knowing the target polarization with a high precision, we could extract the analyzing power from the measured asymmetry in the high-energy polarimeter. The analyzing power at 16.5 GeV/c and 18.5 GeV/c were then determined by the interpolation shown in Fig. 38 which also used data from other experiments. These interpolated values and the data at 13.3 GeV/c are

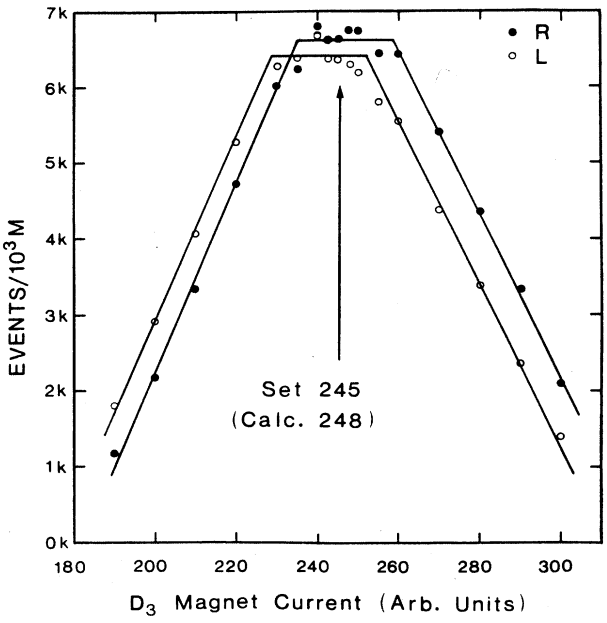

FIG. 36. High-energy polarimeter magnet curve. The number of L and R events at 18.5 GeV/c is plotted against the current in the D_3 bending magnets in the forward arms.

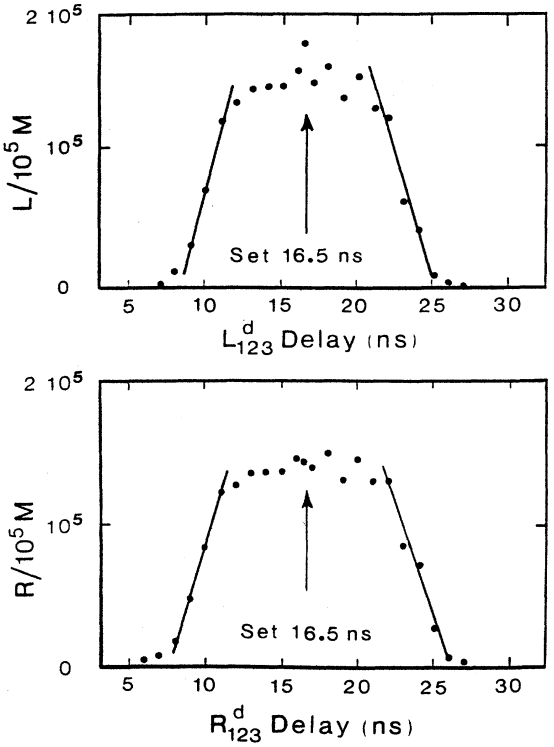

FIG. 37. High-energy polarimeter timing curves. The number of L and R events are, respectively, plotted against the L^d_{123} and R^d_{123} delay times going into the L and R coincidence circuits.

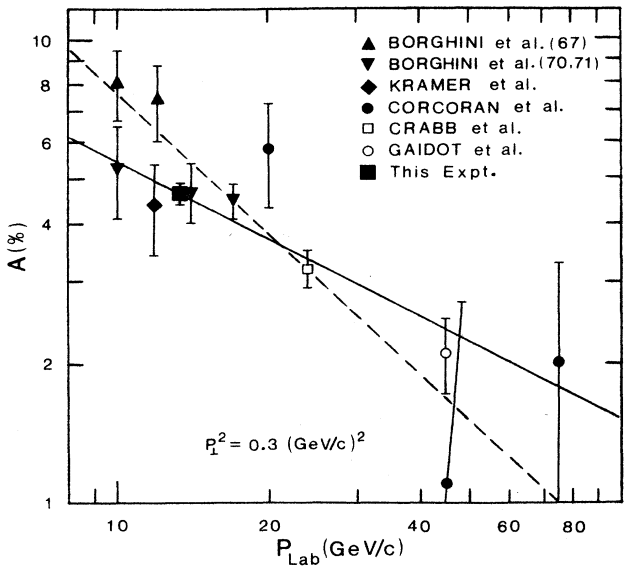

FIG. 38. The analyzing power, A (for the high-energy polarimeter) at $P_\perp^2=0.3$ $(\mathrm{GeV}/c)^2$ is plotted against P_{Lab} for various experiments. The lower-energy $1/P_{\mathrm{Lab}}$ fit is shown as a dashed line, while the solid line is the interpolated fit which we used for A at 16.5, 18.5, and 22 GeV/c.

listed in Table VI. Our new 13.3-GeV/c point at $P_\perp^2=0.3$ $(\mathrm{GeV}/c)^2$ agrees with the 12-GeV/c data of Kramer *et al.*[65] and the 10- and 14-GeV/c data of Borghini *et al.*,[13] but does not agree well with the earlier 10- and 12-GeV/c data of Borghini *et al.*[12]

We calibrated the analyzing power of the internal polarimeter by noting that the beam polarization measured by the internal polarimeter must be equal to the corrected beam polarization measured by the high-energy polarimeter. A correction had to to be made for the depolarization of the extracted protons due to the vertical and horizontal bends in the extracted beam line; the calculated[67] depolarization is shown in Fig. 39. The P_B measured in the high-energy polarimeter was corrected by the calculated depolarization factors of 0.92 at 13.3 GeV/c, 0.92 at 16.5 GeV/c, 0.95 at 18.5 GeV/c and 0.995 at 22 GeV/c. The effective analyzing power of the internal polarimeter was thus determined to be about 2.3% at 13.3 GeV/c, 1.9% at 16.5 GeV/c, and 1.6% at 18.5 GeV/c.

The acceleration of polarized protons at the AGS is summarized in Fig. 40 where the maximum beam polarization is plotted against the AGS momentum. About 10% of the polarization was lost between injection and 13.3 GeV/c where P_B was 65±3%. There was a polarization loss near 14 GeV/c of about 20% which was probably caused by interference between the $G\gamma=36-\nu_y$ intrinsic resonance and the $G\gamma=27$ imperfection resonance. The polarization at 16.5 GeV/c and 18.5 GeV/c, were, respectively, 44±4% and 47±4%. There appeared to be no significant polarization loss between 14 and 22 GeV/c where the polarization was 42±4%. The average AGS accelerated polarized beam intensity was 1.8×10^{10} protons per 2.2-sec pulse.

EXPERIMENT

Polarized proton target

The polarized proton target (PPT) used the dynamic-nuclear-polarization (DNP) technique[68] to polarize the free protons in the target material. This material, which was normally small beads of frozen ammonia[69–71] (NH_3), was contained in a 40-mm-long by 29-mm-diam cylindrical target cavity with its axis parallel to the beam direction as shown in Fig. 41. Free-electron-spin radicals were doped into the target beads and were then polarized by a magnetic field of 2.5 T at a temperature of about 0.5 K. We used 70-GHz microwaves to transfer the electron polarization to nearby protons and we used a 106.8-MHz NMR system to measure the proton polarization. The

TABLE VI. The measured (top row) and interpolated (bottom three rows) values of the analyzing power A for the high-energy polarimeter at $P_\perp^2=0.3$ $(\mathrm{GeV}/c)^2$.

P_{Lab} (GeV/c)	A (%)
13.3	4.66±0.26
16.5	4.2 ±0.3
18.5	3.9 ±0.3
22	3.5 ±0.3

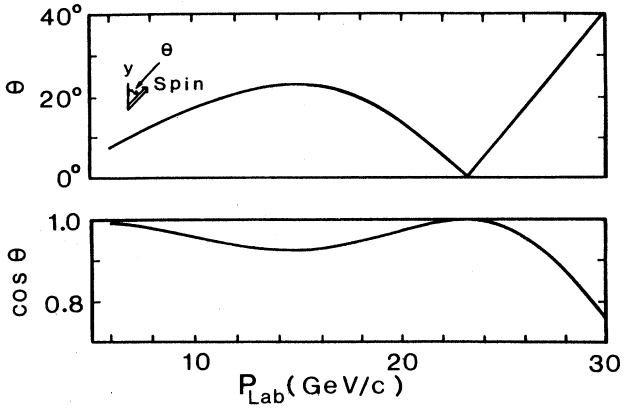

FIG. 39. The calculated precession angle θ of the polarization vector away from the vertical is plotted against beam momentum in the D extracted beam line. The polarization is proportional to $\cos\theta$ which is also shown.

proton polarization direction was periodically reversed by changing the microwave frequency by about 0.5%.

The DNP process first requires adding free-electron-spin radicals to the target beads either by radiation doping or chemical doping. These unpaired electron spins are next polarized and then their polarization is transferred to the free hydrogen protons. These paramagnetic electron centers each have a magnetic moment comparable to a free electron's magnetic moment, μ_e. In a strong magnetic field B at a low temperature T, these electrons acquire a high thermal equilibrium polarization given by

$$P=\tanh\left[\frac{\mu B}{kT}\right]. \tag{42}$$

At a temperature of 0.5 K and a magnetic field of 2.5 T, the electron's polarization is about 99.7%, while the

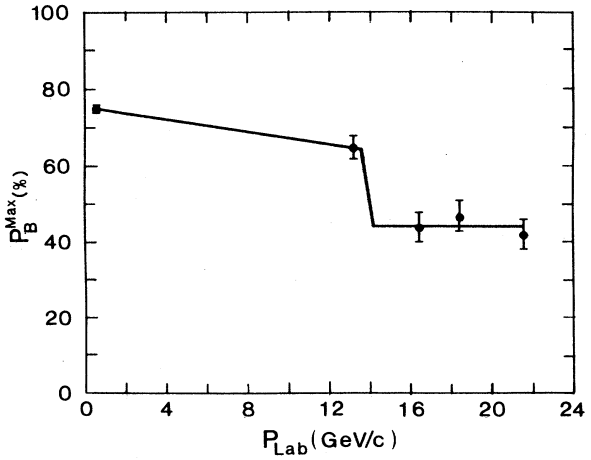

FIG. 40. The maximum AGS beam polarization is plotted against the beam momentum. The errors include both statistical and systematic uncertainties.

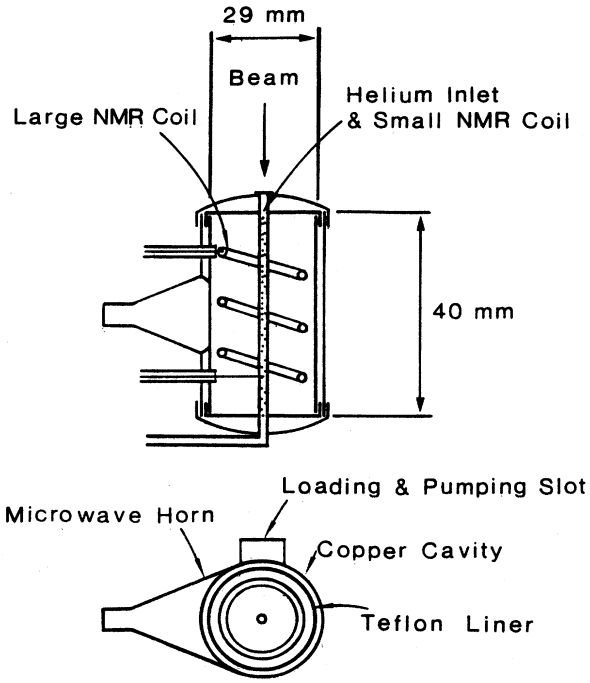

FIG. 41. Diagram of the polarized target cavity.

proton's polarization is only about 0.5% because μ_p is about 660 times smaller than μ_e. One can then enhance the nearby proton's spin polarization by using 70-GHz microwaves to drive spin transitions which use the weak magnetic dipole coupling between the electron's and the proton's magnetic moments. The proton spin polarization then spreads throughout the target beads by a mechanism known as spin diffusion.[68,72]

Our polarized proton target[73–75] used a conventional 2.5-T iron-core C-type magnet with a 75-mm gap. The tapered pole tips provided a magnetic field which was uniform to 1 part in 10^4 over a 2.5-cm-radius region. This uniformity allowed a high homogeneous polarization of the hydrogen protons in the target beads. The microwave frequency of about 70 GHz was matched to drive the appropriate spin transitions in the 2.5-T magnetic field and thus polarized the protons using DNP. About 3 W of microwaves were produced in a carcinotron tube and approximately 1 mW per cm^3 was dissipated in the target beads.

The proton polarization was measured using a University of Liverpool NMR system.[76] The target beads were sampled by a coil operating in series resonance and using a constant current mode Q meter.[76] The NMR resonance curve was driven by a Boonton signal generator which swept the rf by ±250 kHz around the resonance frequency of 106.8 MHz. A PDP-11 microcomputer controlled the signal generator and measured the resonant voltage across the inductive coil. The proton polarization P_T was proportional to the area under the resulting resonant voltage curve. The DNP area was calibrated against the "thermal equilibrium" area, which was measured while the target protons were in thermal equilibrium at about 1 K, with the microwaves and beam both turned off. This

thermal equilibrium polarization at 1 K and 2.5 T was calculated from Eq. (42) to be about 0.25%. The systematic uncertainty in P_T of about 3% was dominated by the error in measuring the temperature at thermal equilibrium using a carbon resistor in the cavity. The remaining systematic error was reduced by signal averaging to well below 1%.

Maintaining the polarized target at 0.5 K required a high-powered refrigerator, especially when used in a high-intensity beam. We used a Roubeau-type[75,77] evaporation refrigerator which is shown in Fig. 42. Liquid ^{4}He was continuously pumped to a pressure of about 100 Torr and thus a temperature of about 2.7 K. This cooled the inner cryostat to about 2.7 K through thermal contract. The cooling fluid in the inner cryostat was a (60%/40%) ^{3}He/^{4}He mixture[71,75] rather than pure ^{3}He. During earlier high-intensity runs we found that this mixture reduced the polarization loss due to the local heating of the beads near the axis where the beam intensity was maximum. Apparently the ^{3}He provided cooling by evaporation while the ^{4}He improved the thermal contact with the target beads. We further reduced the beam-heating problem by feeding the ^{3}He/^{4}He liquid into the target cavity along the central axis through the small NMR coil, which was a thin-walled cupronickel tube with many small holes. The ^{3}He/^{4}He gas mixture was first liquified and then passed through a heat exchanger, where it was further cooled by the returning cold ^{3}He/^{4}He gas. The liquid mixture next passed through a control valve and then into the target cavity where it was further cooled to 0.5 K by evaporation. The cold gas was pumped away by a series of two Roots blower pumps and a mechanical pump with a capacity of 833 liters/sec at a pressure of about 0.15 Torr. The gas was then compressed to about 1 atm, filtered, and recirculated. The circulation rate was about 4 millimoles/sec of ^{3}He/^{4}He mixture which gave a cooling power of about 120 mW at 0.5 K.

We normally used ammonia (NH_3) as the target material because of its high hydrogen content and high resistance to radiation damage. However, for some low beam intensity runs we used a chemically doped material ethyl amine-borane ammonia (EABA) because of its rapid polarization growth time.[78] The frozen NH_3 beads were prepared by freezing liquid NH_3 in an alcohol and dry ice bath and then crushing and selecting 2–3-mm fragments.[79] Using small fragments gave good thermal contact with the ^{3}He/^{4}He mixture. We produced the DNP paramagnetic centers by irradiating the NH_3 beads in a 250-MeV electron beam at the MIT Bates linac at a temperature of 90 K in liquid argon;[75] a typical integrated flux was 5×10^{16} electron/cm^2.

While the Bates irradiation at 90 K seemed to primarily produce polarizing centers, the irradiation at 0.5 K during the AGS experiment produced both polarizing centers and centers which inhibited the polarization growth. These "depolarizing" centers were periodically eliminated by annealing the NH_3 target beads for 3 min at an optimum temperature which we found experimentally to be about 80 K. This annealing apparently did not remove too many polarizing centers. While chemically doped beads must be replaced after a few daily annealings, we used a single set of NH_3 beads for as long as 4 weeks with no significant deterioration. This long bead

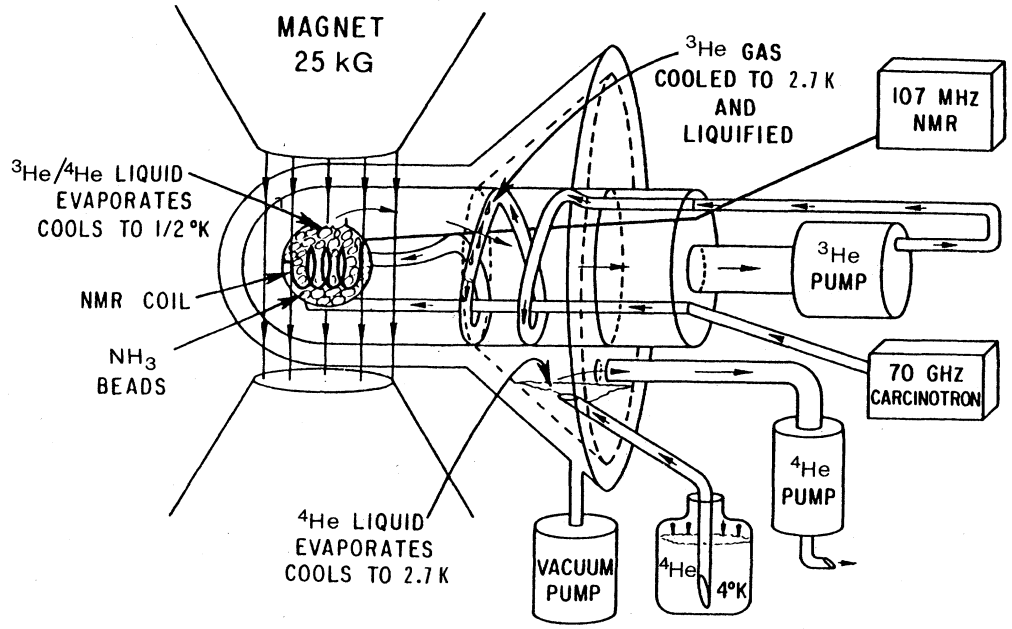

FIG. 42. Diagram of the polarized proton target, indicating the different components including the 2.5-T magnet, the inner and outer refrigerators, the 70-GHz microwave system, and the 107-MHz NMR system.

life makes radiation doped ammonia beads especially suitable for high-intensity beam experiments.[75,79]

During normal operation, the target polarization was reversed approximately every 3 h to minimize the systematic errors. The maximum polarization was typically 70% with a risetime of 25 min. The polarization reversal time was about 30 min. One potential source of error in the polarization measurement was the spatial nonuniformity of the radiation damage caused by the Gaussian shaped beam. We minimized this effect by increasing the beam diameter to 13-mm FWHM. Two separate NMR coils continuously monitored the nonuniformity by independently measuring the nearby polarization. Notice in Fig. 41 that one coil senses mainly the region close to the axis of the target while the other coil senses the outer regions. No significant difference was observed in the polarization measured by these two coils. This was not surprising since our beam intensity was typically 6×10^{9} polarized protons per pulse, which was well below our typical 5×10^{10} unpolarized protons per pulse in high intensity running. The average target polarization for the whole experiment was $53\pm3\%$.

Spectrometer

The double-arm spectrometer detected $p_{\uparrow}+p_{\uparrow}\rightarrow p+p$ events from the polarized proton target. It gave good rejection of inelastic and quasielastic events by measuring both the angle and momentum of both the forward-scattered proton and the backward recoil proton. The spectrometer, which is shown in Fig. 43, contains a 25-m-long forward arm and an 11-m-long recoil arm, each consisting of magnets and scintillation counter hodoscopes. The 36° recoil arm has an upstream dipole magnet for steering protons scattered at angles other than 36°, a dipole magnet for momentum analysis and three sets of scintillation counter hodoscopes B_1,B_2, and B_3. The 5° forward arm has a septum magnet for steering, three dipole magnets for momentum analysis and four sets of counter hodoscopes F_0,F_1,F_2, and F_3. By reversing the PPT magnetic field we obtained additional steering flexibility and could thus measure additional $P_{\perp}^2$ points. All magnets were computer controlled and maintained the required field with a stability of $\pm0.1\%$.

For each $P_{\perp}^2$ and P_{Lab}, a computer kinematic program calculated the momentum, angle, and time of flight of both scattered protons. It also calculated the magnetic-field integral, $\int B\,dl$, needed in each of the six spectrometer magnets to properly steer both scattered protons into the hodoscopes. We then used a computer ray-trace program to determine the position of the F_0 counter and the envelopes of the forward and recoil protons defined by the F_3 and B_3 hodoscopes. These envelopes allowed us to properly pack lead bricks inside the magnet apertures to reduce the background. The F_3 and B_3 counters each defined a momentum bite of typically $\pm5\%$ and a $\Delta\Omega_{\mathrm{Lab}}$ of, respectively, about 7×10^{-5} sr and about 2×10^{-3} sr. The F_0,F_1,F_2,B_1, and B_2 counters were all overmatched to allow for finite target size, angular beam divergence, multiple Coulomb scattering and magnet variations.

All counters were made of 0.5-in.-thick plastic scintillator (pilot B, pilot Y, or NE102). Their sizes and positions are listed in Table VII. Each scintillator was optically connected through an ultraviolet-transmitting Lucite light guide to an RCA 8575 photomultiplier tube with an ORTEC 265 base. The B_1,B_3,F_0,F_1, and F_3 hodoscopes each had 4 horizontal channels (A,B,C, and D), while B_2 and F_2 each had 2 vertical channels (u and d) bringing the total number of channels to 8.

The high voltage on each photomultiplier was set so that the voltage pulse band produced by minimum-ionizing particles passing through the 0.5-in.-thick plastic scintillator was between 80 and 100 mV, well above the discriminator threshold of 40 mV. The high voltages on the cathodes of the photomultiplier tubes ranged from 1750 to 2200 V. They were adjusted individually on two Le Croy 32-channel high-voltage power supplies. Addi-

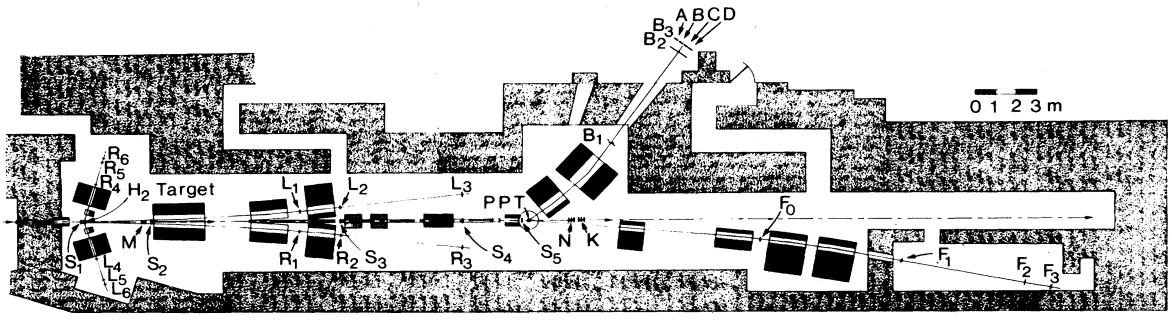

FIG. 43. Layout of the experiment. The polarimeter on the left used a liquid-hydrogen target to measure the left-right asymmetry in p-p elastic scattering. The polarized-proton beam then scattered from the vertically polarized proton target (PPT) and the elastic events were detected by the spectrometer which contained magnets for momentum analysis and the F and B scintillation-counter hodoscopes. The M, N, and K counters were intensity monitors, while the S_1, S_2, S_3, S_4, and S_5 segmented wire ion chambers monitored the beam's position, size, and angle. Moving downstream the F magnets were D_8, D_9, D_{10}, and D_{11} while the B magnets were D_6 and D_7.

tional high current power supplies provided stabilized voltages on the last four dynodes. This stabilization kept the dynode voltages constant and thus reduced the counting losses when the scintillators were subjected to very high instantaneous counting rates. Each counter's efficiency was occasionally checked with a pulse-height-analysis (PHA) measurement using the scintillation light from the 5-MeV α particles emitted by a standard ^{241}Am source.

The output signals from the photomultiplier tubes were analyzed by Le Croy 100-MHz and Phillips 300-MHz NIM electronic logic circuitry. The outputs of the logic network were displayed on 150-MHz Joerger QVS visual scalers and recorded simultaneously by a PDP-11 microcomputer through 100-MHz CAMAC scalers. The visual scaler outputs were recorded after each data run using a Polaroid camera. A complete diagram of the electronic circuitry is shown in Fig. 44. For each hodoscope channel, i, the 800-mV outputs of discriminators B_1^i, B_2^i, and B_3^i passed into a 300-mV threshold coincidence circuit where they triggered a threefold coincidence B^i if they were simultaneous. Similarly the signals from F_1^i, F_2^i, and F_3^i formed a threefold coincidence F^i. The 800-mV output signals from F^i and B^i were then combined together with the F_0^i signal into a threefold coincidence FB_0^i for each hodoscope channel. The resolving time for each coincidence was about 10 nsec. We separately recorded all eight FB_0^i for each run; however, we normally summed the 8 channels to improve the statistical precision

$$FB_0 = FB_0^{Au} + FB_0^{Ad} + FB_0^{Bu} + FB_0^{Bd} + FB_0^{Cu} + FB_0^{Cd} + FB_0^{Du} + FB_0^{Dd} . \quad (43)$$

The total number of FB_0 coincidences is the sum of the elastic scattering events plus the accidental events and the background events. An accidental event is an accidental coincidence between the F and B signals when the corresponding protons did not originate from the same scattering event. The rate for such accidental events was estimated by delaying the recoil-arm signal by 230 nsec and setting it in coincidence with the forward-arm signal from the next rf bucket:

$$(F_1F_2F_3) \text{ into } (B_1B_2B_3)_{\text{del}} . \quad (44)$$

The F_0 counter was installed to reduce the accidental rate and other background rates, and it did significantly reduce these background rates. However, with F_0 additional accidental monitors were needed to estimate additional types of accidental events such as

$$(F_0)_{\text{del}} \text{ into } (F_1F_2F_3B_1B_2B_3) , \quad (45)$$

$$(B_1B_2B_3)_{\text{del}} \text{ into } (F_0F_1F_2F_3) , \quad (46)$$

$$(F_0B_1B_2B_3)_{\text{del}} \text{ into } (F_1F_2F_3) , \quad (47)$$

and

$$(F_0)_{\text{del}} \text{ into } (B_{123})_{\text{del}} \text{ into } (F_{123}) , \quad (48)$$

where del means that the signal is delayed by the 230 nsec between successive AGS rf buckets. These four types of accidental events were subtracted from the raw number of events; all four were quite small due to the relatively low polarized beam intensity.

To ensure that the spectrometer was properly selecting elastic scattering events, we varied the field in one spectrometer magnet around its calculated value. Figure 45 shows a typical magnet curve with a clear elastic peak. Note that the 10% flat background is a measure of inelastic and quasielastic background events which we will discuss later. We ran such magnet curves at each $P_\perp^2$ point and found that the center of the elastic peak normally agreed with the calculated $\int B\,dl$ within about 1%.

The relative timing of each scintillation counter was first calculated and then set experimentally by running standard delay curves. Each curve consisted of measuring the counting rate while varying one input signal cable length. Elastic scattering events were used in the delay curves between the F and B arms. Figure 46 shows one set of delay curves for the F_0 counters. The very small event rate off the peak indicates that the accidental rate was less than 1%.

The beam intensity was measured by an ion chamber and indirectly by three scintillation counter telescopes

TABLE VII. Sizes and positions of spectrometer and monitor counters.

Counter	Size $h \times v$ (in.)	Number	Total size $h \times v$ (in.)	Distance to PPT (in.)
F_0	1.875×2.75	4	5×2.75	400
F_1	2.75×4	4	8×4	705
F_2	12×3.25	2	12×5.5	912
F_3	3.75×5.5	4	12×5.5	992
B_1	6×8	4	20.25×8	227
B_2	20×7	4	40×14	455
B_3	10×14	4	40×14	482
N_1	1×1	1	1×1	93
N_2	1×1	1	1×1	99
N_3	1×1	1	1×1	105
K_1	1×1	1	1×1	114
K_2	1×1	1	1×1	120
K_3	1×1	1	1×1	126

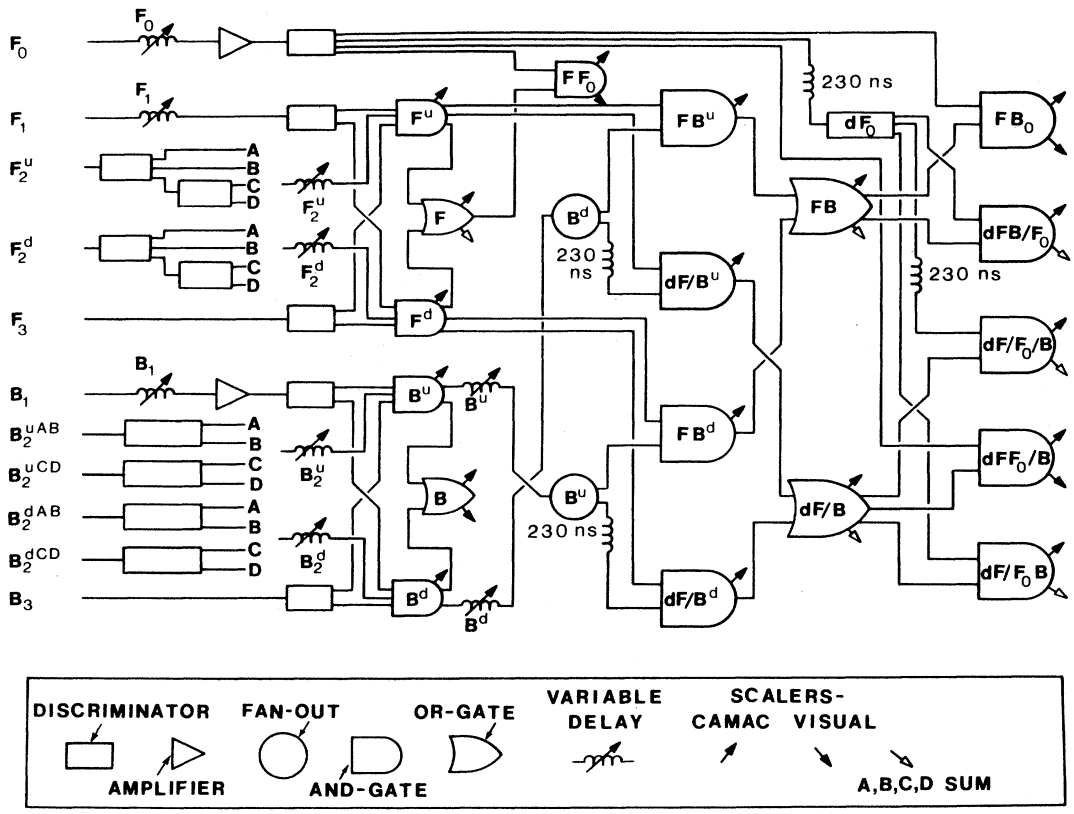

FIG. 44. Electronic-logic diagram for each of the *A*, *B*, *C*, and *D* hodoscope channels of the spectrometer. The notation for accidental monitors, such as dFB/F_0, means that F_0 is delayed by an extra 230 ns.

M, *N*, and *K*, which each counted the particles produced by the beam. The *K* and *N* counters were, respectively, placed directly above and below the beam at angles of about 30° so that they pointed at the PPT. The *M* counter was similarly placed above the beam pointing at the hydrogen target in the polarimeter.

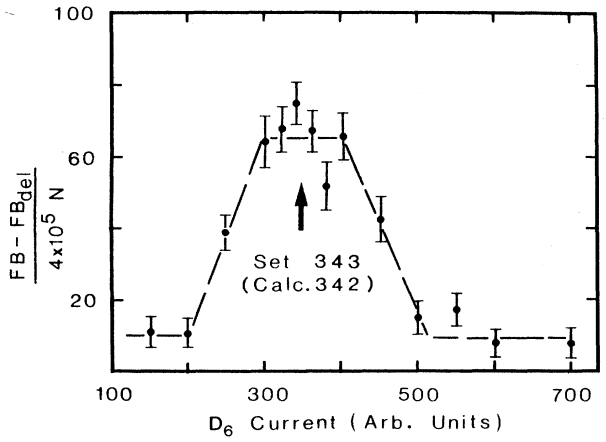

FIG. 45. Magnet curve in the spectrometer. The total number of *p-p* elastic events is plotted against the current in the upstream recoil magnet, D_6. All hodoscope channels have been summed.

During each run, the beam's position and size were monitored by segmented wire ion chambers (SWIC's) placed just upstream of the PPT (S_5) and at other places (S_1,S_2,S_3, and S_4) along the beam line as shown in Figs. 34 and 43. The $DQ_{7/8}$ and DQ_9 quadrupoles just upstream of the PPT were used to focus the beam at the PPT to a size of about 13×13 mm ($h \times v$) FWHM with an angular divergence of about 0.5×1.5 mrad ($h \times v$) FWHM. We reduced the horizontal beam motion at the 29-mm-diam polarized target by using a servosystem discussed later. Beam fluctuations that might cause significant problems were averaged out by reversing the beam polarization every AGS pulse and reversing the target polarization about every 3 h. Some parameters relevant to each measured P_1^2 point are listed in Table VIII.

While our spectrometer was designed to detect only elastic events, it did not reject all inelastic and quasielastic background events. The quasielastic background events were those elastic events coming from the bound protons in the nitrogen nuclei of NH_3. If the nitrogen were polarized,[80] the quasielastic events could induce a left-right asymmetry which would be indistinguishable from the free protons' elastic asymmetry. Fortunately, this background asymmetry was very small because only the outer nitrogen protons could be polarized and cause such an asymmetry. Moreover, the nitrogen polarization was at most 6% (Ref. 80). The binding energy of each

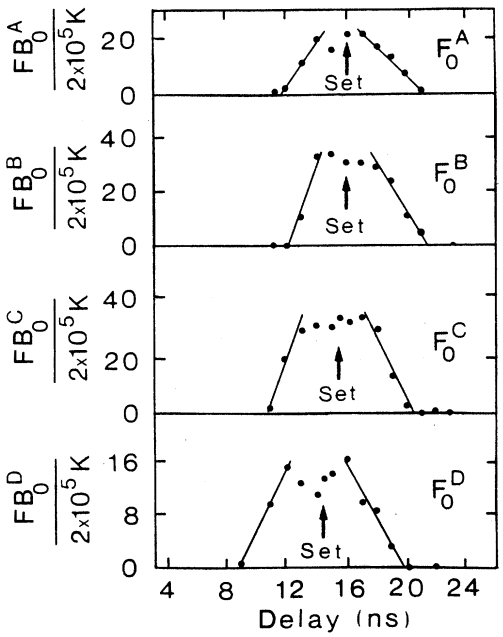

FIG. 46. Spectrometer delay curves. The number of p-p elastic events in each channel of the spectrometer is plotted against each delay in the F_0 hodoscope. The up and down hodoscope channels have been summed.

outer proton corresponding to the 130-MeV/c Fermi momentum was about 8 MeV (Ref. 81). Notice that all seven bound nitrogen protons contributed equally to the quasielastic background, but only one could cause a polarization asymmetry. Since only one of the seven nitrogen protons had this 6% polarization, only about $6\%/7\approx1\%$ of the nitrogen protons could cause an asymmetry in the quasielastic background. The remaining 99% of the background could not cause any left-right asymmetry and could thus be treated as a dilution factor.

We experimentally estimated the quasielastic dilution factor to be 5–15% by taking special runs with hydrogen-free Teflon, C_2F_4, beads substituted for the normal hydrogen-rich ammonia or chemical beads. As will be discussed later, this background determination should be reliable since the atomic number of nitrogen lies between those of carbon and fluorine.

Inelastic events from bound and free protons came mostly from the reaction

$$p+p\rightarrow N^*_{\text{forward}}+p\rightarrow p+\pi^0+p\ . \tag{49}$$

The most serious inelastic background was probably from the N^* with mass 1688 MeV; but fortunately only a small fraction of its decay protons could get into the forward arm because of its tight momentum and angle acceptance. The fairly tight angle and momentum constraints of the recoil arm further reduced the spectrometer's acceptance for inelastic events. The kinematic smear due to the production of a single π meson was much larger than the Fermi momentum smear. Thus the Teflon runs also gave an upper limit on the inelastic background. We estimated[82] the probability of an inelastic event triggering an FB coincidence to be less than 1%.

Experimental procedures

For each data point, we used two independent computer programs to calculate the kinematic parameters for both the spectrometer and the high-energy polarimeter. The beam lines, the magnets and the detectors were then surveyed by the AGS staff and our group, using these cal-

TABLE VIII. Kinematics and acceptance parameters of the spectrometer.

P_{Lab} (GeV/c)	13.3	16.5	18.5
$P_\perp^2$ (GeV/c)^2	1.5	1.6	4.7
$-t$ (GeV/c)^2	1.6	1.7	5.7
$\theta_{\text{c.m.}}$ (deg)	30.5	27.9	49.0
P_F (GeV/c)	11.6	12.4	15.6
θ_F (deg)	5.6	4.7	8.1
P_B (GeV/c)	1.5	1.6	3.9
θ_B (deg)	53.0	52.9	34.2
$\int B\,dl$ (D_6) (kG in.)	374	396	−459
$\int B\,dl$ (D_7) (kG in.)	−673	−700	−1114
$\int B\,dl$ (D_8) (kG in.)	−400	400	−400
$\int B\,dl$ (D_9) (kG in.)	−485	−976	−690
$\int B\,dl$ ($D_{10/11}$) (kG in.)	2003	2434	1720
$\Delta\theta_{\text{c.m.}(F)}$ (deg)	3.7	4.2	3.8
$\Delta\phi_{\text{c.m.}(F)}$ (deg)	1.6	1.8	1.7
$\Delta\theta_{\text{c.m.}(B)}$ (deg)	5.5	5.1	4.3
$\Delta\phi_{\text{c.m.}(B)}$ (deg)	1.3	1.2	2.4
$\Delta\Omega_{\text{c.m.}}$ (msr)	1.4	1.9	2.0
ΔT(PPT$\rightarrow B_3$) (ns)	47.1	46.7	42.0
ΔT(PPT$\rightarrow F_3$) (ns)	86.3	86.4	86.3
$\Delta T(F_3-B_3)$ (ns)	39.2	39.7	44.3
PPT bends	Right	Right	Left

culated particle trajectories and magnetic field integrals. We next partially filled the magnet apertures with lead bricks to reduce the accidental and quasielastic background. We then adjusted the polarized proton target to operate in a stable condition.

The extracted proton beam was transported into our experimental area and tuned to approximately center the beam on both our hydrogen target and polarized target. We then turned off all nearby focusing elements and used two servomagnet systems to center and stabilize the beam's position and angle. The upstream "D_8 trim" magnet, which was placed inside the DD_8 dipole magnet 70 feet upstream of the liquid-hydrogen target, was servocoupled to a split segmented wire ion chamber (SWIC) just upstream of this target. The "DS trim" magnet was just upstream of the liquid-hydrogen target and was servocoupled to a split SWIC just in front of our polarized proton target. The beam position and size (horizontal and vertical) were monitored by five double-plane SWIC's: S_1, S_2, S_3, S_4, and S_5. SWIC S_2 had 1.25-mm wire spacing and the other four SWIC's had 2.00-mm wire spacing. Once the beam was centered on both targets, we used the DQ_5 and DQ_6 quadrupoles to adjust its size and divergence at the liquid-hydrogen target, and the $DQ_{7/8}$ and DQ_9 quadrupoles to adjust the beam's size and divergence at the polarized proton target.

The beam intensity was measured by an ion chamber. Moreover the M scintillators counted the number of particles produced by the beam at the liquid-hydrogen target, and the N and K scintillators counted the number produced in the polarized proton target. These quantities M,N, and K were proportional to the number of beam interactions in each target, and thus were proportional to the beam intensity.

After the beam was properly tuned, we adjusted the photomultiplier high voltages to efficiently detect minimum-ionizing particles. We then ran magnet curves and timing curves as shown in Figs. 45 and 46 which helped us to cleanly select elastic events and to minimize the systematic errors. We also occasionally ran a beam steering curve where we maximized the event rate in the spectrometer while sweeping the beam across the PPT.

After finishing this tune-up procedure, we started taking data in sets of runs. During each run we collected data for about 90 min for a given direction of the target polarization, while the beam polarization was reversed every AGS pulse. Each run ended when either N or K counted a specified number of particles, typically 5×10^6. During each run, we monitored the high voltages, the magnet settings, the target polarization and cryogenics as well as the hydrogen-target liquid level and the beam's position and size at both the H_2 target and the PPT. The scalers and the computer were also monitored. The analog signal from each SWIC was digitized and updated after every 2.2 sec AGS pulse. The average beam position and size at each SWIC, except S_3, were printed by the computer at the end of each run. There were two sets of scalers: the first set recorded the data for the up-beam polarization ($\uparrow$), and the second set recorded the data for the down-beam polarization ($\downarrow$). The number of events in each beam spin state, the average target polarization, and the average beam asymmetry were also printed by the computer at the end of each run. Normally, we took two successive runs with the same direction of target polarization and summed them. The target polarization was reversed after each pair of runs; this reversal took about 30 min.

Data analysis

The differential elastic cross section in the initial spin state ij where, $i=\uparrow$ or $\downarrow$ is the beam spin state and $j=\uparrow$ or $\downarrow$ is the target spin state, is given by

$$\left[\frac{d\sigma}{d\Omega}\right]_{ij}=\frac{\mathcal{N}(ij)}{I_0(ij)N_0 t\rho\,\Delta\Omega\,\epsilon}\ , \tag{50}$$

where $\mathcal{N}(ij)$ is the number of forward-backward coincidences in our spectrometer, $I_0(ij)$ is the number of incident particles, N_0 is Avogadro's number $=6.02\times10^{23}$ particles/mole, t is the target length, ρ is the density of hydrogen protons in the polarized proton target (≈0.098 g/cm^3), $\Delta\Omega$ is the acceptance solid angle of the spectrometer, and ϵ is the detection efficiency. Since there were uncertainties in our absolute measurements of $I_0(ij),\rho,\Delta\Omega$, and ϵ we could not accurately measure the absolute cross sections. But we did accurately measure the relative cross sections for the initial spin states $\uparrow\uparrow$, $\uparrow\downarrow$, $\downarrow\uparrow$, and $\downarrow\downarrow$, by obtaining the normalized event rates, $N(ij)$, given by

$$N(ij)\equiv\frac{\mathcal{N}(ij)}{I(ij)}\ , \tag{51}$$

where $I(ij)$ is the relative beam intensity given by $I(ij)=CI_0(ij)$; note that C is a constant which is independent of the spin state (ij). Since $N_0 t\rho\,\Delta\Omega\epsilon$ is also independent of spin direction, we find from Eqs. (50) and (51) that

$$N(ij)=\text{const}\times\left[\frac{d\sigma}{d\Omega}\right]_{ij}\ . \tag{52}$$

Our experimental results can be described by a set of spin parameters, which are related to the pure-initial-spin state differential elastic cross sections by the formulas

$$\left[\frac{d\sigma}{d\Omega}\right]_{ij}=\left[\frac{d\sigma}{d\Omega}\right]_0[1+P_B(ij)A_B+P_T(ij)A_T+P_B(ij)P_T(ij)A_{nn}]\ , \tag{53}$$

where $(d\sigma/d\Omega)_0$ is the spin-averaged cross section, A_B is the beam analyzing power, A_T is the target analyzing power, and A_{nn} is the initial state spin-spin correlation parameter, while P_B and P_T are, respectively, the beam and target polarizations. Equations (52) and (53) can be solved for A_{nn}, A_B, and A_T to give

$$A_{nn}=\frac{1}{P_B P_T}\frac{N(\uparrow\uparrow)-N(\uparrow\downarrow)-N(\downarrow\uparrow)+N(\downarrow\downarrow)}{N(\uparrow\uparrow)+N(\uparrow\downarrow)+N(\downarrow\uparrow)+N(\downarrow\downarrow)}\equiv\frac{\hat{A}_{nn}}{P_B P_T}\ , \tag{54}$$

$$A_B=-\frac{1}{P_B}\frac{N(\uparrow\uparrow)+N(\uparrow\downarrow)-N(\downarrow\uparrow)-N(\downarrow\downarrow)}{N(\uparrow\uparrow)+N(\uparrow\downarrow)+N(\downarrow\uparrow)+N(\downarrow\downarrow)}$$
$$\equiv-\frac{\hat{A}_B}{P_B}\ , \tag{55}$$

$$A_T=-\frac{1}{P_T}\frac{N(\uparrow\uparrow)-N(\uparrow\downarrow)+N(\downarrow\uparrow)-N(\downarrow\downarrow)}{N(\uparrow\uparrow)+N(\uparrow\downarrow)+N(\downarrow\uparrow)+N(\downarrow\downarrow)}\equiv-\frac{\hat{A}_T}{P_T}\ . \tag{56}$$

The minus sign for A_B and A_T occurs because our spectrometer observes the forward particle that scatters to the right rather than to the left as specified by the Ann Arbor convention.[83] The P_B and P_T in Eqs. (54)–(56) are the average beam and target polarizations of a matched data set that normally consists of two consecutive runs with the target polarization up and the two following runs with the target polarization down.

We had six monitors which could potentially be used to normalize the event rates. These were the N, K, and M counters, the ion chamber and the forward and backward single arms rates, F and B. The normalized intensity used in Eq. (51) was then taken to be

$$I(ij)=\frac{1}{\nu}\sum_{k=1}^{\nu}\frac{m_k(ij)}{\frac{1}{4}\sum_{pq}m_k(pq)}\ , \tag{57}$$

where the m_k are the number of counts in monitor number k in each spin state and ν is the total number of monitors used. The forward arm was not used for the normalization because it was quite long and well defined, and thus quite sensitive to inclusive spin effects. We did not use the K monitor to normalize the event rates since the stand holding K was sometimes accidently kicked. Occasionally one of the other four monitors failed for a short time. We thus used either three or four monitors to normalize each matched data set. We also carefully studied the ratios of the different monitors to ensure that ratios such as N/M stayed fixed when the target spin and the beam spin were reversed.

Errors and corrections

We now discuss the errors and the corrections to the results. From Eqs. (54)–(56) we can explicitly write the errors ΔA_{nn}, ΔA_B, and ΔA_T:

$$(\Delta A_{nn})^2=\left[\frac{\Delta\hat{A}_{nn}}{P_BP_T}\right]^2+A_{nn}^2\left[\left[\frac{\Delta P_B}{P_B}\right]^2+\left[\frac{\Delta P_T}{P_T}\right]^2\right]\ , \tag{58}$$

$$(\Delta A_B)^2=\left[\frac{\Delta\hat{A}_B}{P_B}\right]^2+A_B^2\left[\frac{\Delta P_B}{P_B}\right]^2\ , \tag{59}$$

$$(\Delta A_T)^2=\left[\frac{\Delta\hat{A}_T}{P_T}\right]^2+A_T^2\left[\frac{\Delta P_T}{P_T}\right]^2\ . \tag{60}$$

Note that two types of errors can contribute to the uncertainty in the spin parameters. Statistical errors correspond to the statistical uncertainties in the measured asymmetries $\hat{A}_{nn}$, $\hat{A}_B$, and $\hat{A}_T$. These errors, which we call $\Delta\hat{A}_{nn}$, $\Delta\hat{A}_B$ and $\Delta\hat{A}_T$, are given by

$$\Delta\hat{A}_{nn}=\Delta\hat{A}_B=\Delta\hat{A}_T=\frac{1}{\sqrt{N}}\ , \tag{61}$$

where N is the total number of events for a set of runs. The other type of error is systematic and can occur in the $\hat{A}$'s and in P_B and P_T. As was mentioned earlier, the error on P_T was primarily due to the temperature uncertainty in the thermal equilibrium calibration and was estimated to be $\Delta P_T\approx 3\%$.

The error on P_B, ΔP_B, can be obtained by rewriting Eq. (40) in the form

$$P_B=\frac{\hat{A}_H}{A_H}\ , \tag{62}$$

where $\hat{A}_H$ is the asymmetry measured by the high-energy polarimeter, given by

$$\hat{A}_H=\frac{1}{2}\left[\frac{L\uparrow-R\uparrow}{L\uparrow+R\uparrow}-\frac{L\downarrow-R\downarrow}{L\downarrow+R\downarrow}\right]\ , \tag{63}$$

and A_H is the polarimeter's analyzing power. We then get, from Eq. (62),

$$\Delta P_B=\left[\left[\frac{\Delta\hat{A}_H}{A_H}\right]^2+P_B^2\left[\frac{\Delta A_H}{A_H}\right]^2\right]^{1/2}\ , \tag{64}$$

where ΔA_H is the error in the polarimeter's analyzing power and $\Delta\hat{A}_H=1/\sqrt{N}$ is the statistical error. We see from Table VI that A_H ranged between 3.9% and 4.66% and ΔA_H is about 0.3%. Since P_B was typically 40%, the systematic error in P_B was typically

$$P_B\frac{\Delta A_H}{A_H}\approx 3\%\ . \tag{65}$$

Since the event rate in the high-energy polarimeter was very high, the statistical error was rather small. For a 1 h run, N was typically 10^7 and thus

$$\frac{\Delta\hat{A}_H}{A_H}\approx 0.8\%\ . \tag{66}$$

Therefore, the error in the beam polarization was dominated by the uncertainty in the polarimeter's analyzing power and ΔP_B was typically $\pm 3\%$.

Systematic errors might occur in the $N(ij)$, which could be sensitive to either the stability or the spin dependence of the monitors. If the monitor rates depended upon the beam or target spin state, a systematic spin-up and spin-down asymmetry could be introduced, which would not cancel out when the beam and target polarizations were reversed. To avoid the major problem of left-right asymmetry the M,N, and K monitors were placed directly above or below the vertically polarized beam. While the beam could have a small horizontal spin component, the maximum resulting up-down asymmetry was well below 1%. Any spin-dependent asymmetries were reduced even further by averaging M, which was above the beam line, together with N, which was below the beam line, and with the ion chamber and B, which were

both insensitive to horizontal spin components.

The angle and position of the 13×13 mm ($h\times v$) FWHM beam at the 29-mm-diam polarized proton target were kept centered to within ±0.1 mrad and ±0.2 mm using the servomagnets. The systematic error in the measured asymmetry due to the ±0.2 mm beam motion inside the target is estimated to be at most $\pm0.1\%$. The error due to the angular movement was estimated to be at most $\pm0.4\%$. Moreover, such errors were reduced much further by the signal averaging when we reversed the beam polarization and target polarization about 45 000 and 15 times, respectively, for each data point. The quantities A_{nn} and A_B benefited from the many beam reversals and were therefore much less sensitive to such systematic errors than A_T which benefited only from the less frequent target reversals.

We made several background corrections to the $N(ij)$ for events that were not good elastic events. As mentioned previously, the accidental events were subtracted from the raw number of events. No corrections were made for inelastic events since they were estimated to be less than 1% by calculation and by comparison with the measured quasielastic background.

The quasielastic events were measured using Teflon beads and were treated as a dilution of the spin parameters. To understand this dilution we define $E(ij)$ to be the number of normalized elastic events and $B(ij)$ to be the number of normalized quasielastic background events. The measured event rate is then

$$N(ij)=E(ij)+B(ij) . \tag{67}$$

We showed earlier that the nitrogen polarization in the PPT made a negligible contribution to this background; therefore, we can set $B(\uparrow\uparrow)=B(\uparrow\downarrow)$ and $B(\downarrow\uparrow)=B(\downarrow\downarrow)$. We then get, from Eq. (54),

$$\hat{A}_{nn}=\frac{E(\uparrow\uparrow)-E(\uparrow\downarrow)-E(\downarrow\uparrow)+E(\downarrow\downarrow)}{\sum E(ij)+\sum B(ij)} , \tag{68}$$

which can be written as

$$\hat{A}_{nn}=\frac{E(\uparrow\uparrow)-E(\uparrow\downarrow)-E(\downarrow\uparrow)+E(\downarrow\downarrow)}{\sum E(ij)} \times\left[\frac{1}{1+\sum B(ij)/\sum E(ij)}\right] . \tag{69}$$

We now define the corrected A_{nn} for elastic events to be

$$A_{nn}(\text{corrected}) \equiv\frac{1}{P_B P_T}\frac{E(\uparrow\uparrow)-E(\uparrow\downarrow)-E(\downarrow\uparrow)+E(\downarrow\downarrow)}{\sum E(ij)} . \tag{70}$$

Using Eqs. (54), (69), and (70) we get

$$A_{nn}(\text{corrected})=A_{nn}\left[1+\frac{\sum B(ij)}{\sum E(ij)}\right] . \tag{71}$$

Setting $E(ij)=N(ij)-B(ij)$ in Eq. (71) we get

$$A_{nn}(\text{corrected})=A_{nn}\frac{1}{1-r} , \tag{72}$$

where $r\equiv\sum B(ij)/\sum N(ij)$ is the ratio of the normalized background events to the normalized total number of events. A similar corrected relation can be easily derived for A_T:

$$A_T(\text{corrected})=A_T\frac{1}{1-r} . \tag{73}$$

To get a similar expression for A_B, we must assume that the quasielastic and inelastic background is insensitive to the beam spin direction. This assumption is reasonable since at the 1% level we found no evidence for beam spin dependence during background runs with Teflon beads. Thus we also have, at this 1% level,

$$A_B(\text{corrected})=A_B\frac{1}{1-r} . \tag{74}$$

We will next comment on the measurement of the beam polarization using the high-energy polarimeter. Instead of using Eq. (63) to calculate $\hat{A}_H$, we might use an alternative definition[59a] of this polarimeter asymmetry, namely,

$$\hat{A}_H\equiv\tfrac{1}{2}(\hat{A}_L+\hat{A}_R) , \tag{75}$$

where

$$\hat{A}_L\equiv\frac{L\uparrow-L\downarrow}{L\uparrow+L\downarrow} \tag{76}$$

and

$$\hat{A}_R\equiv-\frac{R\uparrow-R\downarrow}{R\uparrow+R\downarrow} \tag{77}$$

are the asymmetries measured by the left and right arms of the polarimeter. The beam polarization is then given by

$$P_B=\frac{1}{2}\left[\frac{\hat{A}_L}{A_H}+\frac{\hat{A}_R}{A_H}\right] . \tag{78}$$

During the experiment, the ratios $L\uparrow/R\downarrow$ and $L\downarrow/R\uparrow$ were equal to within $\pm5\%$ and the polarizations $\hat{A}_L/A_H$ and $\hat{A}_R/A_H$ were equal to within 4% for a 35% polarized proton beam.

Results

We measured four data points during the experiment. Points I and II were both at $P_{\text{Lab}}=13.3$ GeV/c and $P_\perp^2=1.5$ (GeV/c)^2. Point III was at $P_{\text{Lab}}=16.5$ GeV/c and $P_\perp^2=1.6$ (GeV/c)^2. Point IV was at $P_{\text{Lab}}=18.5$ GeV/c and $P_\perp^2=4.7$ (GeV)^2. We used ammonia (NH_3) beads in the polarized proton target for points II, III, and IV and chemically doped EABA beads for point I. Since the two solid angles defined by the two arms of our spectrometer are best matched at high $P_\perp^2$, we used only the middle B and C hodoscope channels for the medium-$P_\perp^2$ runs of points I, II, and III. However, we used all the four hodoscope channels for the high-$P_\perp^2$ point IV. We used the M and N counters as well as the ion chamber to normalize the event rates in points I and II. We used the M and N counters, the ion chamber, and B to normalize the events in points III and IV.

For each matched set our raw data were the measured asymmetry $\hat{A}$; the statistical error on the measured asymmetry $\Delta\hat{A}$; and the beam and target polarizations P_B and P_T. We then calculated A_{nn}, A_B, and A_T and their statistical errors which are listed in Table IX.

The measured A_B and A_T were used to determine the beam polarization at $P_{\rm Lab}=13.3$ GeV/c by requiring that

$$A_B = A_T \ , \tag{79}$$

as required by rotational invariance in proton-proton elastic scattering. Using Eqs. (55), (62), and (79), we then obtained

$$A_H = -A_T \frac{\hat{A}_H}{\hat{A}_B} \ , \tag{80}$$

which gave a good measurement of the analyzing power, $A_H \equiv A$, of our high-energy polarimeter at $P_{\rm Lab}=13.3$ GeV/c and $P_\perp^2=0.3$ (GeV/c)^2. We found that $A=4.66\pm0.26\%$ as indicated earlier in Table VI and Fig. 38.

We calculated A_{nn}, A_B, and A_T and their errors for each $P_\perp^2$ point by averaging over all the data sets using the formulas

$$A = \frac{\sum_i A_i/(\Delta A_i)^2}{\sum_i (1/\Delta A_i)^2} \tag{81}$$

and

$$\left[\frac{1}{\Delta A}\right]^2 = \sum_i \left[\frac{1}{\Delta A_i}\right]^2 , \tag{82}$$

where each A_i is either A_{nn}, A_B or A_T for a single matched set, each ΔA_i is the corresponding statistical error, and i runs through the N data sets in each point. We also calculated the χ^2 of each averaging process by using

$$\chi^2 = \frac{1}{N-1}\sum_{i=1}^{N}\left[\frac{A-A_i}{\Delta A_i}\right]^2 . \tag{83}$$

When χ^2 was greater than 1, we multiplied the error, ΔA, by $\sqrt{\chi^2}$ to better estimate the systematic errors; when $\chi^2 \le 1$ we did not reduce the error. Note in Table IX that the $\sqrt{\chi^2}$ for A_B and A_{nn} is generally very close to 1; however, $\sqrt{\chi^2}$ for A_T is much larger than 1 for data points I, II, and III. This is because we reversed the target polarization much less frequently than the beam polarization and thus A_T was more sensitive to beam motion systematic errors as discussed earlier. The χ^2 for A_T was 1.04 for point IV where we had 32 target reversals.

We also listed for each point the total number of events, the percentage of accidental events, the quasielastic background correction factor r, and the number of matched sets. We did not take quasielastic background runs at $P_{\rm Lab}=16.5$ GeV/c. However, we estimated this background to be approximately equal to that of point II since the $P_\perp^2$'s and energies were similar and we used the same ammonia target for both points.

A summary of the final data is given in Table X where the estimated systematic errors are included. We have also included our earlier 16.5-GeV/c data.[24] The quantity A is the analyzing power obtained by averaging A_B and A_T, while A_{nn} is the spin-spin correlation parameter.

DISCUSSION

We will now discuss our measurements of spin effects in proton-proton elastic scattering. We measured two medium-$P_\perp^2$ points, at $P_\perp^2=1.5$ and 1.6 (GeV/c)^2 and one high-$P_\perp^2$ point at $P_\perp^2=4.7$ (GeV/c)^2. By using both a polarized beam and a polarized target we measured simultaneously the one-spin analyzing power A and the spin-spin correlation parameter A_{nn}.

The analyzing power,[13,84–89] A, is plotted against $P_{\rm Lab}$

TABLE IX. Detailed data summary.

Data point	I	II	III	IV
$P_{\rm Lab}$ (GeV/c)	13.3	13.3	16.5	18.5
$P_\perp^2$ [(GeV/c)^2]	1.5	1.5	1.6	4.7
Total events	86 775	206 961	28 606	1529
Accidentals (%)	0.2	0.2	0.15	0.13
Number of matched data sets	7	13	4	16
P_T (%)	57.9	53.3	52.4	51.2
P_B (%)	50.8	54.7	21.4	34.1
A_T (%)	11.5±0.6	12.1±0.4	14.1±1.1	1.3±5.0
$\chi^2(A_T)$	4.38	1.49	3.2	1.04
A_B (%)	$=A_T$	$=A_T$	8.4±2.7	−1.3±7.6
$\chi^2(A_B)$			0.36	0.95
A_{nn} (%)	6.3±1.1	8.6±0.7	4.3±5.1	−1.6±14.7
$\chi^2(A_{nn})$	1.2	0.88	0.55	0.82
r	0.052±0.002	0.071±0.003	0.071 (est.)	0.150±0.026
A_T (corrected) (%)	12.1±2.7	13.0±0.6	15.2±3.8	1.5±6.1
A_B (corrected) (%)	$=A_T$	$=A_T$	9.0±2.9	−1.5±8.9
A_{nn} (corrected) (%)	6.6±1.4	9.3±0.8	5±5	−2±17

TABLE X. Final data summary. The analyzing power A is the error weighted mean of A_B and A_T. The $P_\perp^2=2.2$ (GeV/c)^2 point is from our earlier run, Brown *et al.* (Ref. 24).

$P_{\rm Lab}$ (GeV/c)	$P_\perp^2$ [(GeV/c)^2]	A (%)	A_{nn} (%)
13.3	0.3	4.66±0.26	
13.3	1.5	13.0 ±0.6	8.6±0.9
16.5	1.6	11 ±2	5 ±5
16.5	2.2	4.5 ±1.2	6.1±3.0
18.5	4.7	1 ±5	−2 ±17

at $P_\perp^2=1.5$ (GeV/c)^2 in Fig. 47. Some older measurements of A at 14 and 17.5 GeV/c (Ref. 12) were not plotted because of their large errors. The point at 28 GeV/c is the highest energy, good precision measurement of A near $P_\perp^2=1.5$ (GeV/c)^2. From rotational invariance, the analyzing power in p-p elastic scattering must vanish at $\theta_{\rm c.m.}=90°$ which occurs near 4 GeV/c. The plot shows that A rises very rapidly from 0 near 4 GeV/c to about 22% at 6 GeV/c. The analyzing power then appears to decrease fairly smoothly to about 6% at 28 GeV/c. If the decrease in A continues at higher energies, then A might become negative near 40 GeV/c.

The spin-spin correlation parameter[84–86] A_{nn} is also plotted against $P_{\rm Lab}$ at $P_\perp^2=1.5$ (GeV/c)^2 in Fig. 47. Notice that A_{nn} drops from a value of about 12% at 4 GeV/c, where $\theta_{\rm c.m.}$ is about 90°, to about 8% at 6 GeV/c; A_{nn} then remains constant up to 13.3 GeV/c. The large error data point at 16.5 GeV/c and $P_\perp^2=1.6$ (GeV/c)^2 is consistent with A_{nn} remaining constant.

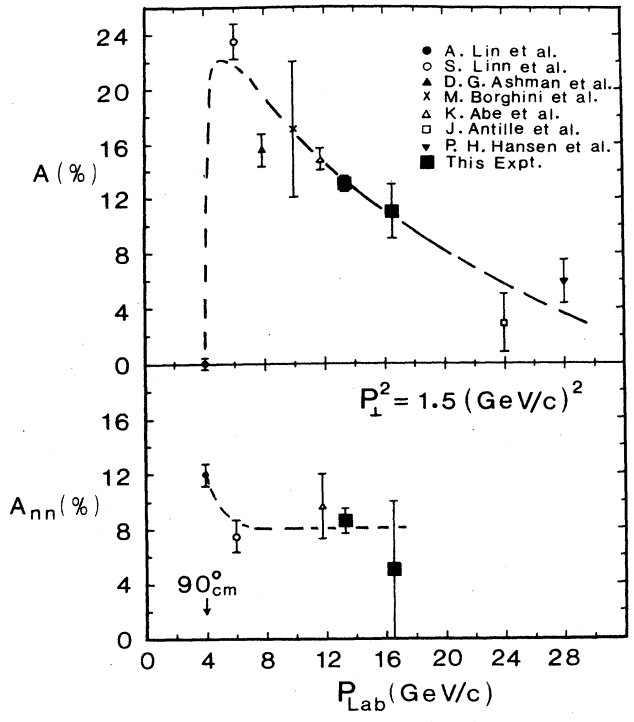

FIG. 47. The analyzing power A and the spin-spin correlation parameter A_{nn} are plotted against $P_{\rm Lab}$ at $P_\perp^2=1.5$ (GeV/c)^2. The dashed lines are hand-drawn curves to guide the eye.

Both A and A_{nn} are plotted as a function of $P_\perp^2$ at $P_{\rm Lab}=16.5$ GeV/c in Fig. 48 (Ref. 24). The data suggest that A has a pronounced $P_\perp^2$ dependence in this medium $P_\perp^2$ region. This behavior appears similar to the broad medium-$P_\perp^2$ peak in A at 11.75 GeV which is shown[23] in Fig. 49 along with our new 13.3-GeV/c data. The errors on A_{nn} in Fig. 48 are too large to say much except that the $P_\perp^2$ dependence is probably not very strong. Notice that A and A_{nn} appear to behave differently from each other when plotted against either $P_{\rm Lab}$ or $P_\perp^2$. This suggests that A and A_{nn} might have different origins and their study may address quite different physics questions.

We now turn to our measurements at large $P_\perp^2$ which probe the inner structure of the proton. In these violent collisions both the 1-spin and 2-spin forces show unexpected behavior which is difficult to reconcile with our current theories of strong interactions. The analyzing power[90–92] A at $P_\perp^2=4.7$ (GeV/c)^2 is plotted against $P_{\rm Lab}$ in Fig. 50. The data suggest that A is quite small and has

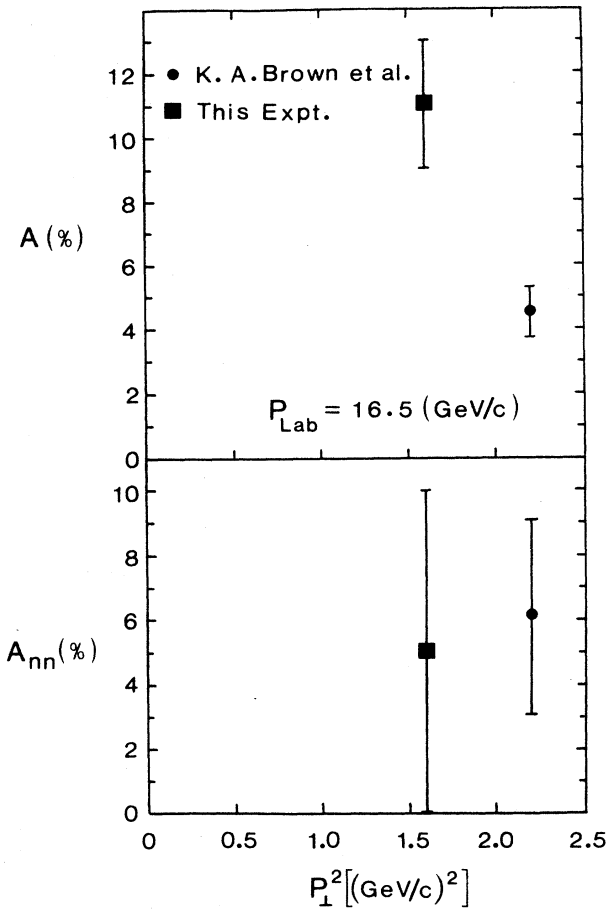

FIG. 48. The analyzing power A and the spin-spin correlation parameter A_{nn} are plotted against $P_\perp^2$ at $P_{\rm Lab}=16.5$ GeV/c.

little energy dependence at this fairly large $P_\perp^2$. Note that A must be equal to 0 near $P_{\rm Lab}=11$ GeV/c where $P_\perp^2=4.7$ (GeV/c)^2 corresponds to $90°_{\rm c.m.}$. In an earlier AGS experiment[93] we found a rapid and unexpected rise in A just beyond $P_\perp^2=5$ (GeV/c)^2.

The spin-spin correlation parameter A_{nn} is plotted against $P_{\rm Lab}$ at $P_\perp^2=4.7$ (GeV/c)^2 in Fig. 51. In this high-$P_\perp^2$ region, A_{nn} has a strong and unexpected energy dependence; it appears to drop from about 60% near 11.75 GeV/c to near zero at 18.5 GeV/c. This sharp change seems just as surprising as the original discovery of the large spin-spin force at high $P_\perp^2$. Several theoretical models predicted oscillations in A_{nn}, but none predicted that it would drop in this way. To better understand this unexpected behavior we will briefly review the two ZGS experiments which studied A_{nn} at high $P_\perp^2$.

The first ZGS experiment[87,91,94] changed $P_\perp^2$ by varying the scattering angle while $P_{\rm Lab}$ was held fixed at 11.75 GeV/c. This fixed-energy experiment found that A_{nn} increased rapidly from about 10% at $P_\perp^2=3.6$ (GeV/c)^2 to about 60% at $P_\perp^2=5.1$ (GeV/c)^2. However, $P_\perp^2=5.1$ (GeV/c)^2 corresponds to $\theta_{\rm c.m.}=90°$ at $P_{\rm Lab}=11.75$ GeV/c. Since $90°_{\rm c.m.}$ is a symmetry point for p-p scattering, Bethe[95] and Weisskopf[96] independently noted that the large value of A_{nn} could be a particle identity effect rather than a high-$P_\perp^2$ hard scattering effect. A second experiment[84,90] was then done in which the scattering angle was held fixed at $\theta_{\rm c.m.}=90°$ and $P_\perp^2$ was changed by varying the beam momentum up to 12.75 GeV/c. The ratio of the spin-parallel to spin-antiparallel cross sections, $\sigma(\uparrow\uparrow)/\sigma(\uparrow\downarrow)$, was then plotted against $P_\perp^2$ as shown in Fig. 52. Clearly the behavior of the ratio in the fixed-angle experiment was essentially identical to the ratio's behavior in the fixed-energy experiment, except at small $P_\perp^2$. Indeed, at the ZGS's maximum $P_\perp^2$ of about 5 (GeV/c)^2, the ratio $\sigma(\uparrow\uparrow)/\sigma(\uparrow\downarrow)$ increased up to a value

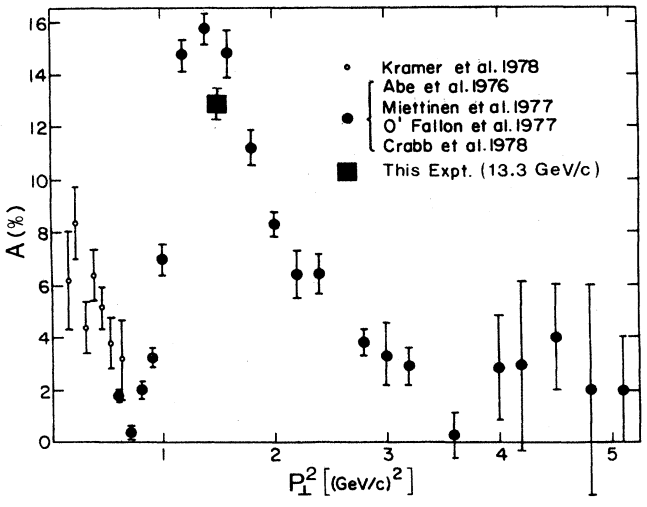

FIG. 49. The analyzing power A at 11.75 GeV/c is plotted (Ref. 23) against $P_\perp^2$. Data from various experiments are shown (Refs. 65, 87, 91, and 94) along with our new 13.3-GeV/c data.

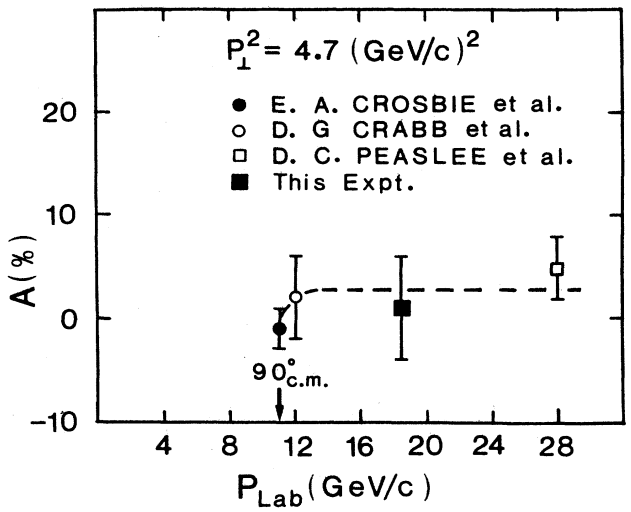

FIG. 50. The analyzing power A is plotted against $P_{\rm Lab}$ at $P_\perp^2=4.7$ (GeV/c)^2. The dashed line is a hand-drawn curve to guide the eye.

of about 4 in both experiments. A ratio of 4 corresponds to an A_{nn} of 60%. This striking similarity in behavior strongly suggested that the large value of A_{nn} was indeed a high-$P_\perp^2$ hard-scattering effect and was not a particle identity effect.

However, the ZGS data gave no indication of how A_{nn} would behave at high $P_\perp^2$ when $\theta_{\rm c.m.}$ was far from 90°. The smallest angle 11.75 GeV/c point with large A_{nn} was

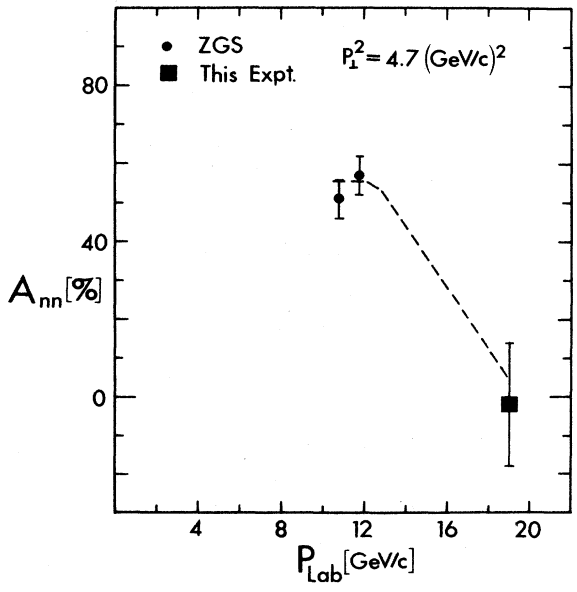

FIG. 51. The spin-spin correlation parameter A_{nn} is plotted against incident laboratory momentum for proton-proton elastic scattering at $P_\perp^2=4.7$ (GeV/c)^2. The error bars include both statistical and systematic errors. The dashed line is a hand-drawn curve to guide the eye.

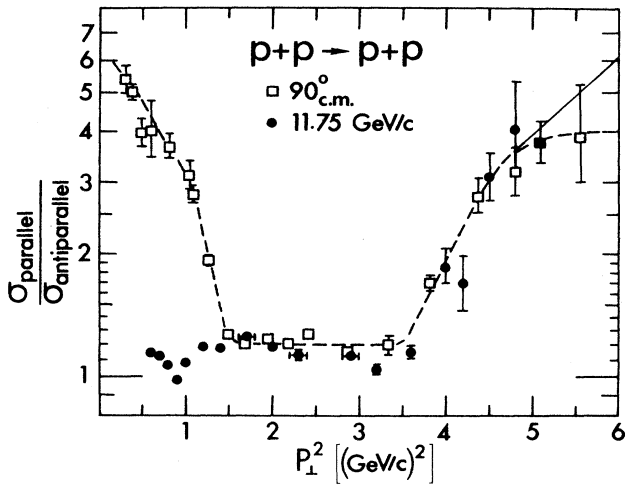

FIG. 52. The ratio of the spin-parallel to spin-antiparallel differential cross sections is plotted against $P_\perp^2$ for p-p elastic scattering. The dashed and solid lines are hand-drawn to guide the eye for the $90°_{\text{c.m.}}$ fixed-angle experiment and the 11.75-GeV/c fixed-energy experiment.

at $P_\perp^2=4$ (GeV/c)^2 where $\theta_{\text{c.m.}}$ was about 62°. Our new AGS point was the first A_{nn} measurement at high $P_\perp^2$ with $\theta_{\text{c.m.}}$ very far from 90°. At $P_{\text{Lab}}=18.5$ GeV/c and $P_\perp^2=4.7$ (GeV/c)^2 where $\theta_{\text{c.m.}}$ was 49° we found that A_{nn} was consistent with zero.

One possible explanation of this strange behavior is that large spin-spin effects might only occur when two conditions both occur simultaneously: $P_\perp^2$ must be large and $\theta_{\text{c.m.}}$ must be near 90°. Another possible explanation is that A_{nn} may oscillate as a function of $P_\perp^2$ and/or P_{Lab}. An unlikely but possible explanation is that A_{nn} is still 60% and our new zero A_{nn} measurement was a 3.6 standard deviation statistical fluctuation. It seems very improbable that A_{nn} is small everywhere and that the many ZGS points were wrong by 5 to 10 standard deviations. There has recently been considerable theoretical discussion of the first two explanations which we will discuss below. However, the best way to understand the nature of this unexpected effect may be to measure A_{nn} at exactly $90°_{\text{c.m.}}$ at higher energy.

Most ZGS transversity spin-spin data are shown along with the AGS data in Fig. 53, which is a three-dimensional plot of the ratio of the spin-parallel to spin-antiparallel cross sections against $P_\perp^2$ and P_{Lab}. There is a great deal of structure in this three-dimensional plot, especially near $\theta_{\text{c.m.}}=90°$. While the maximum value of the spin ratio depends strongly on P_{Lab}, the ratio always seems to reach a maximum at exactly $90°_{\text{c.m.}}$. The ratio also seems to oscillate strongly as a function of both $P_\perp^2$ and P_{Lab}. This three-dimensional plot certainly does not support the earlier belief that spin effects go to zero at high energy and at large $P_\perp^2$.

To better understand the spin parameters, we can set $P_B=P_T=1$ and rewrite Eq. (53) as

$$\sigma(ij)\equiv\frac{(d\sigma/d\Omega)_{ij}}{(d\sigma/d\Omega)_0}=1\pm A_B\pm A_T\pm A_{nn}\ , \tag{84}$$

where the $\sigma(ij)$'s are the relative pure-initial-spin cross sections. Using rotational invariance, we get, from Eq. (84),

$$\sigma(\uparrow\uparrow)=1+2A+A_{nn}\ , \tag{85}$$

$$\sigma(\uparrow\downarrow)=\sigma(\downarrow\uparrow)=1-A_{\text{nn}}\ , \tag{86}$$

$$\sigma(\downarrow\downarrow)=1-2A+A_{nn}\ . \tag{87}$$

From Eqs. (85)–(87) the ratio of the spin-parallel to spin-antiparallel cross sections can now be written as

$$\frac{\sigma(\uparrow\uparrow)+\sigma(\downarrow\downarrow)}{\sigma(\uparrow\downarrow)+\sigma(\downarrow\uparrow)}=\frac{1+A_{nn}}{1-A_{nn}}\ . \tag{88}$$

Thus, when A_{nn} is positive the protons scatter more often when their spins are parallel than when they are antiparallel. Moreover, positive A_{nn} is equivalent to the spin-triplet cross section being larger than the spin singlet cross section. Notice that A_{nn} parametrizes the spin-spin or tensor component of the nuclear force.

We can also obtain from Eqs. (85)–(87) the analyzing power, A, which measures the spin-orbit component of the proton-proton force:

$$\frac{\sigma(\uparrow\uparrow)-\sigma(\downarrow\downarrow)}{\sigma(\uparrow\uparrow)+\sigma(\downarrow\downarrow)+\sigma(\uparrow\downarrow)+\sigma(\downarrow\uparrow)}=A\ . \tag{89}$$

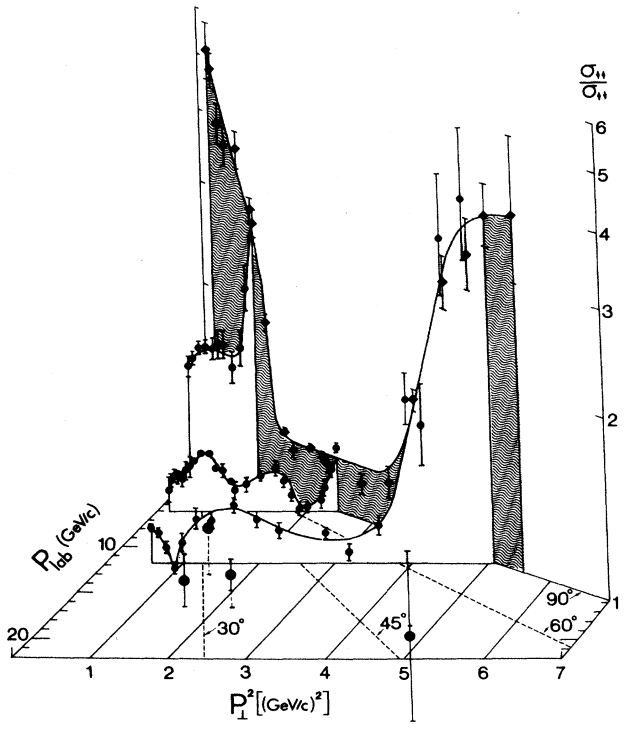

FIG. 53. Three-dimensional plot. The ratio of the spin-parallel to spin-antiparallel cross sections is plotted against $P_\perp^2$ and P_{Lab}. Data from the ZGS and this experiment are shown along with hand-drawn curves to guide the eye. The dashed lines show the c.m. scattering angle.

When A is positive, a proton scatters more when its spin is parallel to its orbital angular momentum than when it is antiparallel. Thus using the Ann Arbor convention,[83] spin-up protons scatter more to the left than to the right when A is positive.

To relate our spin experiments to various theoretical models of strong interactions, we will introduce the p-p scattering amplitudes. When two spin-$\frac{1}{2}$ protons interact, there are 16 scattering amplitudes corresponding to the 2^4 different spin states of the initial and final protons. However, for proton-proton elastic scattering, the requirements of parity conservation, time-reversal invariance, and identical particle symmetry reduce the number of independent amplitudes from 16 to 5. Thus, nine real parameters (five magnitudes and four relative phases) are needed to completely specify p-p elastic scattering at each energy and scattering angle.

Many theoretical papers use the helicity amplitudes[97] which quantize the spin of each proton along its direction of motion. The s-channel helicity amplitudes can be denoted by

$$\begin{aligned}
\phi_1&=\langle ++|++\rangle\ ,\\
\phi_2&=\langle --|++\rangle\ ,\\
\phi_3&=\langle +-|+-\rangle\ ,\\
\phi_4&=\langle +-|-+\rangle\ ,\\
\phi_5&=\langle ++|+-\rangle\ ,
\end{aligned}\tag{90}$$

where $+$ and $-$, respectively, denote spin parallel and antiparallel to the proton's momentum. The helicity-nonflip amplitudes are ϕ_1 and ϕ_3. The double-flip amplitudes are ϕ_2 and ϕ_4. The single-flip amplitude is ϕ_5. The analyzing power, A, and the spin-spin correlation parameter, A_{nn}, are given in terms of these helicity amplitudes, by

$$\sigma_0 A=\mathrm{Im}[(\phi_1+\phi_2+\phi_3-\phi_4)\phi_5^*]\tag{91}$$

and

$$\sigma_0 A_{nn}=2|\phi_5|^2+\mathrm{Re}(\phi_1\phi_2^*-\phi_3\phi_4^*)\ ,\tag{92}$$

where σ_0 is proportional to the spin-averaged differential elastic cross section

$$\sigma_0=\tfrac{1}{2}(|\phi_1|^2+|\phi_2|^2+|\phi_3|^2+|\phi_4|^2+4|\phi_5|^2)\ .\tag{93}$$

Another common set of amplitudes are the transversity amplitudes[98] which quantize the spin along the normal to the scattering plane. The transversity amplitudes are especially interesting since most high-energy spin experiments are done in transversity states with the beam and target both polarized in the vertical direction which is perpendicular to the horizontal scattering plane. In p-p elastic scattering all single spin-flip transversity amplitudes must vanish because of parity conservation.[99] A third set are the exchange amplitudes[100] which have definite t-channel quantum numbers at large s and small t.

During the 1970s, when the ZGS spin experiments were under way, several optical,[101] Regge,[102] or quantum-chromodynamics[103–105] models were proposed to account for the observed spin effects. Both the optical and Regge models had some success in describing spin effects in the small-$P_\perp^2$ diffraction region, but could not successfully describe spin effects at large $P_\perp^2$. Quantum chromodynamics is much more directed towards large-$P_\perp^2$ spin effects and we will discuss it in some detail.

The variable $P_\perp$ is especially useful in describing scattering processes because it is canonically conjugate to the impact parameter b. Thus high $P_\perp^2$ is required to deeply probe the internal structure of the proton at small distance. High-$P_\perp^2$ studies have led to a dynamical theory of the proton's constituents called quantum chromo-

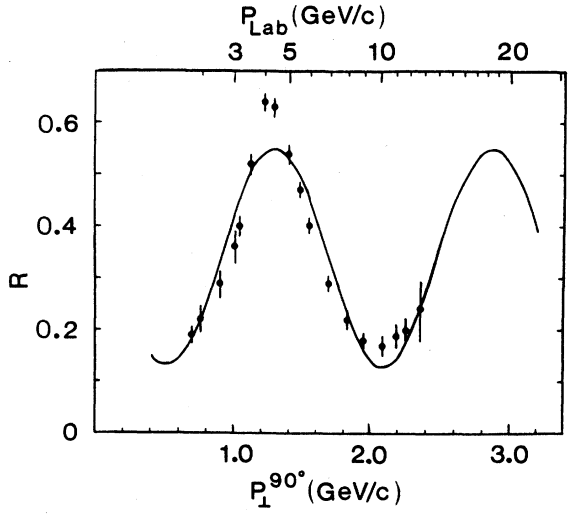

FIG. 54. The ratio $R=\frac{1}{2}[1-A_{nn}(90°)]d\sigma/dt(90°)$: $1.15\times10^3\exp(-8.13P_\perp)$ is plotted against $P_\perp$ at $90°_{\text{c.m.}}$. Also shown is Hendry's fit (Ref. 109) to this plot, $R=0.34[1-0.62\cos(4.0P_\perp^{90°}-2.06)]$.

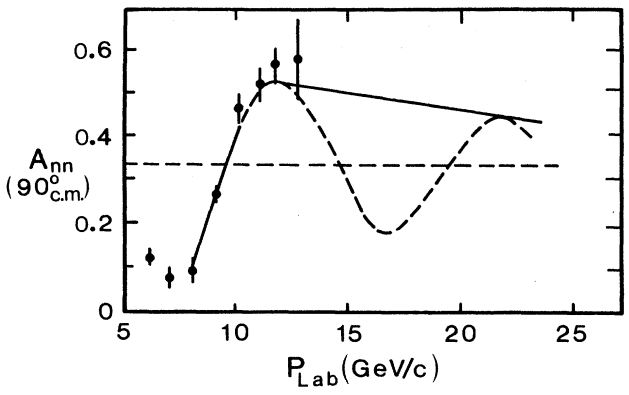

FIG. 55. The spin-spin correlation parameter (Refs. 84 and 90) A_{nn} at $90°_{\text{c.m.}}$ is plotted against P_{Lab} and compared with the model of Troshin and Tyurin (Ref. 113). The solid curve represents a monotonic decrease to the limiting value of $\frac{1}{3}$ while the dashed curve shows a decreasing oscillation about $\frac{1}{3}$.

dynamics (QCD).[106] This theory should allow perturbative calculations of proton-proton elastic scattering at high enough energy and high enough $P_\perp^2$. There is some indication that perturbative QCD should be applicable to our data because the dimensional-counting scaling law for fixed-angle scattering seems to apply[107] at similar energy and $P_\perp^2$. The scaling law suggests that the exclusive process $A+B\to C+D$ can be fit by the equation

$$\frac{d\sigma}{dt}(A+B\to C+D)=\frac{1}{s^{n-2}}f(\theta_{\text{c.m.}}) , \tag{94}$$

where $n=n_A+n_B+n_C+n_D$ is the total number of constituents in the initial plus the final particles. For p-p elastic scattering, since the four protons are believed to each contain three constituent quarks, $n=12$ and we have

$$\frac{d\sigma}{dt}(p+p\to p+p)\propto s^{-10}f(\theta_{\text{c.m.}}) . \tag{95}$$

The best overall fit to the available data is

$$\frac{d\sigma}{dt}\propto s^{-9.7}f(\theta_{\text{c.m.}}) , \tag{96}$$

which gives a fair fit to the spin-average p-p elastic data for[107] $s\geq 15$ (GeV/c)^2 and $|t|\geq 2.5$ (GeV/c)^2.

Farrar *et al.*[103] and Brodsky *et al.*[104] made the first attempts to describe the spin dependence of p-p elastic scattering using the simple quark-interchange model (QIM). In this model, quarks are interchanged while conserving helicity, so that the total helicity of the initial p-p state is equal to the total helicity of the final p-p state. The double-helicity-flip amplitude $\phi_2=\langle --|++\rangle$ vanishes in this model. However, although $\phi_4=\langle +-|-+\rangle$ is also a double-helicity-flip amplitude, it does not vanish since there is no net helicity change when both proton's helicities are flipped. Since $\phi_5=\langle ++|+-\rangle$ is a single helicity flip amplitude, it must vanish in this model. Since $\phi_5=0$ at all $\theta_{\text{c.m.}}$, Eq. (91) implies that

$$A=0 . \tag{97}$$

This appears to be a firm prediction of the QIM at all $\theta_{\text{c.m.}}$. Any significant deviation of A from zero is thus an indication of major difficulties for the model in that kinematic domain. Another firm prediction of QIM is

$$A_{nn}(90^\circ_{\text{c.m.}})=\tfrac{1}{3} . \tag{98}$$

This value of 33% is only about half of the observed maximum value of 60% from the ZGS data. Clearly, Figs. 52 and 53 show that the A_{nn} prediction of the simple QIM is inconsistent with the data. However, it has been conjectured that these predictions of the simple QIM might only hold at very high energy and very high $P_\perp^2$. Unfortunately, there is no agreement about the exact energy and $P_\perp^2$ where QIM might become applicable to spin experiments.[108]

Another suggestion was[109] that A_{nn} at $90^\circ_{\text{c.m.}}$ might oscillate as it approaches the value of $\frac{1}{3}$. The spin-averaged p-p elastic scattering cross section shows[110,111] some oscillations around the predicted s^{-10} behavior at $90^\circ_{\text{c.m.}}$, which might be somewhat related to the structure in A_{nn} at $90^\circ_{\text{c.m.}}$. Hendry[112] illustrated these possible oscillations in $d\sigma/dt$ by plotting the ratio

$$\frac{(d\sigma/dt)^{90^\circ}[\text{mb(GeV}/c)^{-2}]}{1.15\times 10^3\exp(-8.13P_\perp)} . \tag{99}$$

This exponential gives a slightly better fit to the average behavior of $d\sigma/dt(90^\circ_{\text{c.m.}})$ than the s^{-10} power law. Hendry noticed that this $90^\circ_{\text{c.m.}}$ cross-section oscillation has a periodicity with a $\Delta P_\perp$ of about 1.6 GeV/c. He also found the same periodicity in the quantity $\frac{1}{2}[1-A_{nn}(90^\circ_{\text{c.m.}})]d\sigma/dt(90^\circ_{\text{c.m.}})$ (Ref. 109), which is plotted in Fig. 54. Hendry noted that if A_{nn} really oscillates, then $A_{nn}(90^\circ_{\text{c.m.}})$ should decrease at momenta above 14 GeV/c and reach a minimum near 25 GeV/c. However, he did not predict exact values for $A_{nn}(90^\circ_{\text{c.m.}})$ and he made no specific prediction about A_{nn} away from $90^\circ_{\text{c.m.}}$. Hendry[109] also suggested that A_{nn} may also oscillate at other $\theta_{\text{c.m.}}$.

Troshin and Tyurin[113] also predicted that $A_{nn}(90^\circ_{\text{c.m.}})$ might oscillate around $\frac{1}{3}$. Their model assumes that each quark in the proton scatters independently in a mean field at each impact parameter. Their prediction of a damped oscillation of $A_{nn}(90^\circ_{\text{c.m.}})$ as a function of beam momentum is shown in Fig. 55. Troshin and Tyurin recently extended[114] their model to angles away from $90^\circ_{\text{c.m.}}$. For our recent point at $P_{\text{Lab}}=18.5$ GeV/c, and $\theta_{\text{c.m.}}=49^\circ$, they calculated that $A_{nn}=-6\%$ which is consistent with our data. They also predict that A_{nn} at $P_\perp^2$ of 4.7 (GeV/c)^2 will again become large and positive above 20 GeV/c.

The discrepancies between the perturbative QCD predictions for large-angle p-p scattering and the experimental spin data prompted Nardulli, Preparata, and Soffer to propose[115] the massive-quark model (MQM). As in QCD, the protons are composed of quarks but in the MQM the constituents are massive and they interact via an infinite sequence of meson exchanges. One interesting prediction of the MQM at $P_{\text{Lab}}=28$ GeV/c is that

$$A_{nn}(90^\circ_{\text{c.m.}})=97\% . \tag{100}$$

Note that the 60% maximum measured value of A_{nn} lies approximately halfway between the QIM and MQM predictions. Although the MQM provides a large helicity flip amplitude, it still gives zero analyzing power because the amplitudes are real. Bourrely *et al.*[116] also suggested combining their earlier diffraction scattering model with the MQM. Large values of A and A_{nn} were calculated from the interference between the dominant imaginary nonflip amplitude for diffraction scattering and the real spin-flip amplitudes of the MQM.

As suggested by Bethe[95] and Weisskopf[96] the peaking of A_{nn} at $90^\circ_{\text{c.m.}}$ might be a particle identity effect rather than a large $P_\perp^2$ hard-scattering effect. To understand these particle identity effects we can expand Eq. (84) to define the relative pure spin transversity cross sections

$$\begin{aligned}
\sigma(\uparrow\uparrow)&\equiv\sigma(\uparrow\uparrow\rightarrow\uparrow\uparrow)+\sigma(\uparrow\uparrow\rightarrow\downarrow\downarrow)\ ,\\
\sigma(\downarrow\downarrow)&\equiv\sigma(\downarrow\downarrow\rightarrow\downarrow\downarrow)+\sigma(\downarrow\downarrow\rightarrow\uparrow\uparrow)\ ,\\
\sigma(\uparrow\downarrow)&\equiv\sigma(\uparrow\downarrow\rightarrow\uparrow\downarrow)+\sigma(\uparrow\downarrow\rightarrow\downarrow\uparrow)\ ,\\
\sigma(\downarrow\uparrow)&\equiv\sigma(\downarrow\uparrow\rightarrow\downarrow\uparrow)+\sigma(\downarrow\uparrow\rightarrow\uparrow\downarrow)\ ,
\end{aligned}\tag{101}$$

where $\sigma(ij\rightarrow kl)$ is the relative p-p elastic scattering cross section from the initial spin state (ij) to the final spin state (kl), and i,j,k, and l may each be either $\uparrow$ or $\downarrow$ (spin up or spin down). Notice that all eight single flip transversity cross sections are zero because of parity conservation in p-p elastic scattering.[99] The ratio of the spin-parallel to spin-antiparallel cross sections is given by

$$R(\theta)\equiv\frac{\sigma(\uparrow\uparrow)(\theta)+\sigma(\downarrow\downarrow)(\theta)}{\sigma(\uparrow\downarrow)(\theta)+\sigma(\downarrow\uparrow)(\theta)}\ .\tag{102}$$

Using the notation of N and D being the nonflip and the double-flip transversity amplitudes for "Gedanken distinguishable" protons, Lipkin[117,118] obtained for the scattering of two identical protons

$$\begin{aligned}
\sigma(\uparrow\uparrow)(\theta)&=|N(\uparrow\uparrow)(\theta)+N(\uparrow\uparrow)(\theta-\pi)|^2\\
&\quad+|D(\uparrow\uparrow)(\theta)+D(\uparrow\uparrow)(\theta-\pi)|^2\ ,\\
\sigma(\uparrow\downarrow)(\theta)&=|N(\uparrow\downarrow)(\theta)+D(\uparrow\downarrow)(\theta-\pi)|^2\\
&\quad+|D(\uparrow\downarrow)(\theta)+N(\uparrow\downarrow)(\theta-\pi)|^2\ .
\end{aligned}\tag{103}$$

Similar relations hold for the case where $\downarrow\downarrow$ is substituted for $\uparrow\uparrow$ and $\downarrow\uparrow$ for $\uparrow\downarrow$. He then evaluated the ratio $R(\theta)$ at both small angles and at $90^\circ_{\text{c.m.}}$. He found that even if the direct p-p scattering amplitude is totally spin independent, the forward-backward coherence in Eq. (103) can still make $R(90^\circ_{\text{c.m.}})$ equal to 2. He also found that a small double spin-flip component $(D^2/N^2\sim 0.07)$ can make $R(90^\circ_{\text{c.m.}})$ equal to 4 although $R(\theta)$ is only about 1.04 at small angles. However, Lipkin's approach has been criticized by Soffer,[119] and by Anselmino and Leader.[120] Tomozawa[121] independently suggested that $R(90^\circ_{\text{c.m.}})$ can be equal to 4 even if the proton-proton cross section exhibits "quasi spin independence." However, his definition of "quasi spin independence"

$$\sigma_{\text{triplet}}(\uparrow\uparrow)=2\sigma_{\text{singlet}}(\uparrow\downarrow)\tag{104}$$

seems to have significant spin dependence. Thus the role of particle identity near $90^\circ_{\text{c.m.}}$ seems quite interesting and is probably important; but it is still quite unsettled.

In general the large spin-spin effects seen in the three-dimensional plot of σ_{parallel}: $\sigma_{\text{antiparallel}}$ seem difficult to reconcile with current theories of strong interactions such as quantum chromodynamics. The data certainly do not suggest that spin-spin effects are disappearing as the energy and $P_\perp^2$ are increased. The large 1-spin A seen[93] at the AGS also seems inconsistent with the perturbative QCD (PQCD) prediction[122] that A should be zero at $P_\perp^2=6.5$ $(\text{GeV}/c)^2$ and 28 GeV/c. Both experiments suggest that if QCD is correct then nonperturbative effects may be quite important in this $P_\perp^2$ and P_{Lab} range. While experiments can certainly be done at much higher P_{Lab}, it will be difficult to measure any exclusive cross section at significantly higher $P_\perp^2$ because $d\sigma/dt$ drops so rapidly. Thus these unexpected 1-spin and 2-spin effects may limit the usefulness of PQCD in exclusive hadronic scattering for the foreseeable future.

Since the AGS polarized beam has now reached 22 GeV/c with 42% polarization, we hope to soon extend our measurements to 22 GeV/c to determine if A_{nn} at large $P_\perp^2$ stays near zero, oscillates up to become large and positive again, or becomes negative for the first time. If A_{nn} oscillates up and becomes large and positive, it will agree with the predictions of Hendry[109,112] and Troshin and Tyurin.[113,114] If A_{nn} stays small, this behavior might support either the importance of particle identity effects near $90^\circ_{\text{c.m.}}$ (Refs. 26, 95, 96, 117, 118, and 121) or possibly the importance of QCD (Refs. 103 and 104). If A_{nn} is negative, this would disagree with essentially all existing predictions. We also hope to later measure these spin-spin effects at exactly $90^\circ_{\text{c.m.}}$ at the highest possible energy to determine if the ratio $\sigma(\uparrow\uparrow)/\sigma(\uparrow\downarrow)$ goes up, goes down, or for some mysterious reason stays constant at exactly the value of 4.

ACKNOWLEDGMENTS

We would like to thank Dr. D. I. Lowenstein and the many members of the Brookhaven AGS staff who helped in commissioning the AGS polarized-proton beam. We thank the staff of the Massachusetts Institute of Technology Bates Linac for their help with our polarized target bead irradiation. Some of the people from Brookhaven and elsewhere deserving special thanks are A. Abola, D. Barton, E. Blesser, B. Briscoe, J. Buchanan, G. M. Bunce, L. Burgar (deceased), R. Casella, I. H. Chiang, R. Claus, T. Clifford, R. Clipperton, B. Cork, G. Cornish, J. G. Cottingham, J. Dabrowski, C. Eld, A. Feltman, H. Foelsche, R. Frankel, J. Funaro, C. Gardner, E. Gill, J. Gabusi, G. Glass, J. W. Glenn, W. Haeberli, J. W. Humphrey, E. Jablonski, S. Kennel, M. Knott, K. Kohler, R. Lari, D. Lazarus, C. Liu, V. LoDestro, R. Mackenzie-Wilson, S. Magill, L. Mazarakis, A. McNerney, R. Meier, R. Mobley, D. R. Moffett, A. Moretti, J. Niederer, B. Oerter, P. Pape, E. F. Parker (deceased), C. Pearson, A. Pendzick, A. Perlmutter, J. W. Post, C. W. Potts, W. Praeg, M. Puglisi, R. R. Rau, K. Reese, J. Rice, R. Ruth, N. P. Samios, R. Sanders, P. F. Schultz, S. Sidhu, L. W. Smith, M. Tanaka, R. Thern, R. Timm, W. van Asselt, W. Venegas, D. Warburton, R. Warkentien, P. Yamin, and P. Zuhoski. This work was supported by several research contracts from the U. S. Department of Energy. We are especially grateful to Dr. W. A. Wallenmeyer for his consistent support and encouragement during the past decade. The following authors of this paper worked on the acceleration of polarized protons: F.Z.K, P.R.C., D.G.C., M.F., P.H.H., M.E.H., A.D.K., A.M.T.L., S.L.L., R.S.R., R.R.R., T.R., T.S., K.M.T., L.A.A., J.G.A., H.N.B., E.D.C., S.G., H.J.H., A.K., R.L., S.Y.L., Y.Y.L., R.E.L., Y.I.M., P.A.M., R.J.N., L.G.R., J.F.S., T.J.S., A.S., S.T., R.L.W., J.B.R., G.C.P., V.W.H., P.S., J.A.B., and R.L.M. The following authors of this paper worked on the measurements of $p_\uparrow+p_\uparrow\rightarrow p+p$: F.Z.K., P.R.C., G.R.C., D.G.C., I.G., P.H.H., M.E.H., A.D.K.,

A.M.T.L., D.C.P., R.S.R., R.R.R., T.R., T.S., K.M.T., K.A.B., G.T.D., L.G.R., J.B.R., J.R.O., T.S.B., L.C.N., M.S. One of the authors (P.R.C.) was supported by MIT during part of this work. The early work of A.K. was performed at Yale University. The early work of L.G.R. was performed at Argonne National Laboratory. This paper is based upon a University of Michigan thesis by F. Z. Khiari (Ref. 82).

---

[a]Present address: AGS Department, Brookhaven National Laboratory, Upton, NY 11973.
[b]Present address: Physics Department, University of Liverpool, Liverpool, L69 3BX England, and Department of Physics, MIT, Cambridge, MA 02139.
[c]Present address: Sony/Tektronix Corporation, 9-31 Kitashinagawa 5-chrome Shinagawa Ku, Tokyo 141, Japan.
[d]Present address: Neils Bohr Institute, DK-2100, Copenhagen, Denmark.
[e]Present address: Wilmington College, Wilmington, Ohio 45177.
[f]Present address: Department of Physics, Florida State University, Talahassee, FL 32306.
[g]Joint appointment with University of Maryland.
[h]Present address: High Energy Physics Division, Argonne National Laboratory, Argonne, IL 60439.
[i]Present address: Suffolk County Community College, Selden, NY 11784.
[j]Present address: Fermilab, P.O. Box 500, Batavia, IL 60510.
[k]Present address: Division of High Energy Physics, U.S. Department of Energy, Washington, D.C. 20545.
[l]Present address: AT Division, Los Alamos National Laboratory, Los Alamos, NM 87545.

[1]S. Goudsmit and G. Uhlenbeck, Naturwissenschaften **13** (1925); Nature (London) **117** (1926).
[2]The spin of the proton was first postulated by D. M. Dennison in 1927. See the *Encyclopaedic Dictionary of Physics* (Pergamon, New York, 1962), Vol. 6, p. 773.
[3]E. Wigner, Phys. Rev. **51**, 106 (1937).
[4]L. Wolfenstein, Annu. Rev. Nucl. Sci. **6**, 43 (1956).
[5]N. F. Mott, Proc. R. Soc. London **A124**, 425 (1929).
[6]C. L. Oxley *et al.*, Phys. Rev. **91**, 419 (1953).
[7]O. Chamberlain *et al.*, Phys. Rev. **105**, 288 (1957).
[8]J. A. Kane *et al.*, Phys. Rev. **95**, 1694 (1954); T. Fields *et al.*, *ibid.* **96**, 812 (1954); J. Marshall *et al.*, *ibid.* **95**, 1020 (1954); S. M. Marcowitz, *ibid.* **120**, 891 (1960).
[9]R. E. Seamon *et al.*, Phys. Rev. **165**, 1579 (1968); M. H. MacGregor *et al.*, *ibid.* **182**, 1714 (1969).
[10]G. Cozzika *et al.*, Phys. Rev. **164**, 1672 (1967).
[11]P. Grannis *et al.*, Phys. Rev. **148**, 1297 (1966).
[12]M. Borghini *et al.*, Phys. Lett. **24B**, 77 (1967).
[13]M. Borghini *et al.*, Phys. Lett. **31B**, 405 (1970); **36B**, 501 (1971).
[14]M. G. Albrow *et al.*, Nucl. Phys. **B23**, 445 (1970).
[15]N. E. Booth *et al.*, Phys. Rev. Lett. **21**, 651 (1968); **23**, 192 (1969); D. J. Sherden *et al.*, *ibid.* **25**, 898 (1970); J. H. Parry *et al.*, Phys. Rev. D **8**, 45 (1973).
[16]G. W. Abshire *et al.*, Phys. Rev. D **12**, 3393 (1975); Phys. Rev. Lett. **32**, 1261 (1974); D. R. Rust *et al.*, Phys. Lett. **58B**, 114 (1975).
[17]J. H. Snyder *et al.*, Phys. Rev. Lett. **41**, 781 (1978).
[18]G. Fidecaro *et al.*, Phys. Lett. **105B**, 309 (1981).
[19]M. Corcoran *et al.*, Phys. Rev. D **22**, 2624 (1980).
[20]T. Khoe *et al.*, Part. Accel. **6**, 213 (1975).
[21]E. F. Parker, in *High Energy Physics with Polarized Beams and Polarized Targets,* edited by M. L. Marshak (AIP Conf. Proc. No. 35) (AIP, New York, 1976), p. 382.
[22]A. Yokosawa, Phys. Rep. **64**, 47 (1980).
[23]R. C. Fernow and A. D. Krisch, Annu. Rev. Nucl. Part. Sci. **31**, 107 (1981).
[24]K. A. Brown *et al.*, Phys. Rev. D **31**, 3017 (1985).
[25]L. G. Ratner, IEEE Trans. Nucl. Sci. **NS-32**, 1656 (1985).
[26]G. R. Court *et al.*, Phys. Rev. Lett. **57**, 507 (1986).
[27]A. D. Krisch, in *Proceedings of the 7th International Symposium on High Energy Spin Physics,* Protvino, USSR, 1986, edited by L. D. Soloviev, N. E. Tyurin, and V. L. Solovianov (IHEP, Protvino, 1987), Vol. 1, p. 41.
[28]K. M. Terwilliger, in 1987 Particle Acceleration Conference, Washington, D.C. (unpublished).
[29]A. D. Krisch and A. J. Salthouse, editors, *Higher Energy Polarized Beams* (AIP Conf. Proc. No. 42) (AIP, New York, 1978).
[30]B. Cork *et al.*, in *Proceedings of the 1978 Summer Study on Polarized Protons in the Brookhaven AGS,* edited by A. D. Krisch (University of Michigan, Ann Arbor, 1978), p. 1.
[31]D. G. Crabb *et al.*, IEEE Trans. Nucl. Sci. **NS-26**, 3203 (1979).
[32]K. M. Terwilliger *et al.*, IEEE Trans. Nucl. Sci. **NS-28**, 2031 (1981).
[33]D. G. Crabb *et al.*, IEEE Trans. Nucl. Sci. **NS-30**, 2176 (1983).
[34]H. N. Brown and Y. Makdisi, Brookhaven National Laboratory Report No. TN-23, 1982 (unpublished).
[35]A. Kponou *et al.*, IEEE Trans. Nucl. Sci. **NS-32**, 1764 (1985); W. Haeberli *et al.*, Nucl. Instrum. Methods **62**, 355 (1980).
[36]W. Haeberli, Annu. Rev. Nucl. Sci. **17**, 373 (1967).
[37]H. Bruck, *Accelerateurs Circulaires de Particules* (Presses Universitairs de France, Paris, 1966).
[38]I. M. Kapchinskiy and V. A. Teplyakov, Pri. Tekh. Eksp. **2**, 119 (1970).
[39]R. H. Stokes *et al.*, IEEE Trans. Nucl. Sci. **NS-26**, 3469 (1979).
[40]The computer program for machining our RFQ vanes was obtained from Los Alamos National Laboratory, K. R. Crandall *et al.* (private communication).
[41]H. N. Brown *et al.*, in Proceedings of the 1984 Linear Accelerator Conference, 1984 (unpublished).
[42]L. C. Maier, Jr., MIT Report No. 143, 1949 (unpublished).
[43]J. Le Duff, in *Proceedings of the CERN Accelerator School* (CERN, Report No. 85-19, Geneva, 1985), pp. 170 and 176.
[44]S. Humphries, Jr., *Principles of Charged Particle Acceleration* (Wiley Interscience, New York, 1986), pp. 482–493.
[45]M. Froissart and R. Stora, Nucl. Instrum. Methods **7**, 297 (1960).
[46]D. Cohen, Rev. Sci. Instrum. **33**, 161 (1962).
[47]E. Courant, BNL Report No. EDC-45, 1962 (unpublished).
[48]V. Ernst, Nucl. Instrum. Methods **60**, 52 (1968).
[49]E. D. Courant and R. D. Ruth, Report No. BNL 51270, 1980 (unpublished).
[50]L. H. Thomas, Philos. Mag. **3**, 1 (1927).
[51]V. Bargman, L. Michel, and V. L. Telegdi, Phys. Rev. Lett. **2**, 435 (1959).

[52]E. D. Courant and H. S. Snyder, Ann. Phys. (N.Y.) **3**, 1 (1958).
[53]R. J. Nawrocky and R. F. Lambiase, IEEE Trans. Nucl. Sci. **NS-30**, 2772 (1983).
[54]L. A. Ahrens and L. G. Ratner, Brookhaven National Laboratory Report No. TN-255, 1986 (unpublished).
[55]K. M. Terwilliger, University of Michigan Report No. UM HE 81-42, 1981 (unpublished).
[56]K. M. Terwilliger *et al.*, IEEE Trans. Nucl. Sci. **NS-32**, 2635 (1985).
[57]K. M. Terwilliger, Brookhaven National Laboratory report, 1986 (unpublished).
[58]J. Skelly, T. Clifford, and R. Frankel, IEEE Trans. Nucl. Sci. **NS-30** (1983).
[59]D. G. Crabb *et al.*, Report No. BNL 32780, 1983 (unpublished).
[59a]Another equation for calculating P_B is

$$P_B=\frac{1}{A}\left[\frac{L^*-R^*}{L^*+R^*}\right],$$

where L^* and R^* are given by the geometric means $L^*\equiv\sqrt{L_\uparrow R_\downarrow}$ and $R^*\equiv\sqrt{L_\downarrow R_\uparrow}$. See, e.g., G. G. Ohlsen and P. W. Keaton, Jr., Nucl. Instrum. Methods **109**, 41 (1973). The two equations give the same results if the L and R arms are identical. The two equations for P_B have different sensitivities to different types of systematic errors. For the high-energy polarimeter these systematic errors are very small compared to the 3% uncertainty in the analyzing power. The errors are larger in the 200-MeV polarimeter which is only used for beam tuning.
[60]J. B. Roberts (private communication). The elastic p-carbon analyzing power A is over 80% at 12° and 16° at 200 MeV. However, the polarimeter also detected some nonelastic events which reduced its effective analyzing power to 62% at 12° and 51% at 16°.
[61]These numbers were calculated assuming that the focusing occurred downstream of SWIC S_2 in Fig. 34. If the focusing had occurred upstream of SWIC S_2, the beam divergences at SWIC S_1 would be larger.
[62]R. E. Diebold *et al.*, Phys. Rev. Lett. **35**, 632 (1975).
[63]D. G. Crabb *et al.*, Nucl. Phys. **B121**, 231 (1977).
[64]D. Miller *et al.*, Phys. Rev. D **16**, 2016 (1977).
[65]S. L. Kramer *et al.*, Phys. Rev. D **17**, 1709 (1978).
[66]A. Gaidot *et al.*, Phys. Lett. **61B**, 103 (1976).
[67]G. M. Bunce, Report No. BNL 29856, 1981 (unpublished).
[68]A. Abragam, *Principles of Nuclear Magnetism* (Clarendon, Oxford, 1961); C. D. Jeffries, *Dynamic Nuclear Orientation* (Interscience, New York, 1963); A. Abragam and M. Goldman, Rep. Prog. Phys. **41**, 395 (1978).
[69]T. O. Niinikoski and J. M. Rieubland, Phys. Lett. **72A**, 141 (1979).
[70]D. G. Crabb, P. R. Cameron, A. M. T. Lin, and R. S. Raymond, in *Proceedings of the 4th International Workshop on Polarized Target Materials and Techniques,* Bad Honnef, 1984, edited by W. Meyer (Bonn University, Bonn, 1984), p. 7.
[71]See Cameron, Crabb, Lin, and Raymond (Ref. 70, p. 143).
[72]N. Bloembergen, Physica **15**, 386 (1949).
[73]J. A. Bywater *et al.*, University of Michigan report, 1974 (unpublished).
[74]See Crabb *et al.* (Ref. 70, p. 7); Brown *et al.* (Ref. 70, p. 66); P. R. Cameron *et al.* (Ref. 70), p. 143.
[75]R. S. Raymond, P. R. Cameron, D. G. Crabb, and T. Roser, in *International Workshop on Polarized Sources and Targets,* Montana, Switzerland, 1986, edited by S. Jaccard and S. Mango [Helv. Phys. Acta **59**, 777 (1986)].
[76]D. Gifford and G. R. Court, in *Proceedings of the 2nd Workshop on Polarized Target Materials,* edited by G. R. Court, S. F. J. Cox, D. A. Cragg, and T. O. Niinikoski (Rutherford Laboratory, Chilton, 1980), pp. 76 and 85.
[77]P. Roubeau and J. Vermeulen, Cryogenics **478** (1971).
[78]See Hill, Hill, and Krumpolc (Ref. 70, p. 84).
[79]See Cameron (Ref. 70, p. 79).
[80]See Court, Heyes, Meyer, and Thiel (Ref. 70, p. 53).
[81]D. Halliday, *Introduction to Nuclear Physics* (Wiley, New York, 1961), p. 262.
[82]This estimate was based on both analytical and Monte Carlo calculations, F. Z. Khiari, University of Michigan thesis, Ann Arbor, 1987.
[83]*Higher Energy Polarized Beams,* edited by A. D. Krisch and A. J. Salthouse (AIP Conf. Proc. No. 42) (AIP, New York, 1978), p. 142.
[84]A. Lin *et al.*, Phys. Lett. **74B**, 273 (1978).
[85]S. L. Linn *et al.*, Phys. Rev. D **26**, 550 (1982).
[86]D. G. Aschman *et al.*, Nucl. Phys. **B125**, 349 (1977).
[87]K. Abe *et al.*, Phys. Lett. **63B**, 239 (1976).
[88]J. Antille *et al.*, Nucl. Phys. **B185**, 1 (1981).
[89]P. H. Hansen *et al.*, Phys. Rev. Lett. **50**, 802 (1983).
[90]E. A. Crosbie *et al.*, Phys. Rev. D **23**, 600 (1981).
[91]D. G. Crabb *et al.*, Phys. Rev. Lett. **41**, 1257 (1978); J. R. O'Fallon *et al.*, *ibid.* **39**, 733 (1977).
[92]D. C. Peaslee *et al.*, Phys. Rev. Lett. **51**, 2359 (1983).
[93]P. R. Cameron *et al.*, Phys. Rev. D **32**, 3070 (1985).
[94]H. E. Miettinen *et al.*, Phys. Rev. D **16**, 549 (1977).
[95]H. A. Bethe (private communication).
[96]V. F. Weisskopf (private communication).
[97]M. Jacob and G. C. Wick, Ann. Phys. (N.Y.) **7**, 404 (1959).
[98]A. Kotanski, Acta Phys. Pol. **30**, 629 (1966).
[99]A. Bohr, Nucl. Phys. **10**, 486 (1959).
[100]F. Halzen and G. H. Thomas, Phys. Rev. D **10**, 344 (1974).
[101]L. Durant and F. Halzen, Nucl. Phys. **B104**, 317 (1976).
[102]A. W. Hendry and G. W. Abshire, Phys. Rev. D **10**, 3662 (1974).
[103]G. R. Farrar *et al.*, Phys. Rev. D **20**, 202 (1979).
[104]S. J. Brodsky, C. E. Carlson, and H. J. Lipkin, Phys. Rev. D **20**, 2278 (1979).
[105]G. F. Wolters, Phys. Rev. Lett. **45**, 776 (1980).
[106]D. Sivers *et al.*, Phys. Rep. **23**, 1 (1976).
[107]P. V. Landshoff and J. C. Polkinghorne, Phys. Lett. **44B**, 293 (1973).
[108]B. M. Schwarzschild, Phys. Today **38**(8), 17 (1985).
[109]A. W. Hendry, Phys. Rev. D **23**, 2075 (1981).
[110]C. W. Akerlof *et al.*, Phys. Rev. **159**, 1138 (1967).
[111]R. C. Kammerud *et al.*, Phys. Rev. D **4**, 1309 (1971).
[112]A. W. Hendry, Phys. Rev. D **10**, 2300 (1974).
[113]S. M. Troshin and N. E. Tyurin, J. Phys. (Paris) Colloq. **46**, C2-235 (1985).
[114]S. M. Troshin and N. E. Tyurin, Report No. IHEP 86-121, Serpukhov, 1986 (unpublished).
[115]G. Nardulli, G. Preparata, and J. Soffer, Nuovo Cimento **83A**, 361 (1984); Phys. Rev. D **31**, 626 (1985).
[116]C. Bourrely, J. Soffer, and T. T. Wu, Phys. Rev. D **19**, 3249 (1979); Nucl. Phys. **B247**, 15 (1984); C. Bourrely and J. Soffer, Phys. Rev. Lett. **54**, 760 (1985).
[117]H. J. Lipkin, Phys. Lett. B **181**, 164 (1987).

[118]H. J. Lipkin, in *1985 School on Intermediate and High Energy Physics,* edited by W. R. Falk (TRIUMF report, Vancouver, 1985), p. 1.
[119]J. Soffer, BNL theory report, 1986 (unpublished).
[120]M. Anselmino and E. Leader, Birkbeck College, University of London report, 1986 (unpublished).
[121]Y. Tomozawa, Phys. Rev. D **36**, 2854 (1987).
[122]G. R. Goldstein and M. J. Moravcsik, Phys. Rev. D **32**, 303 (1985).

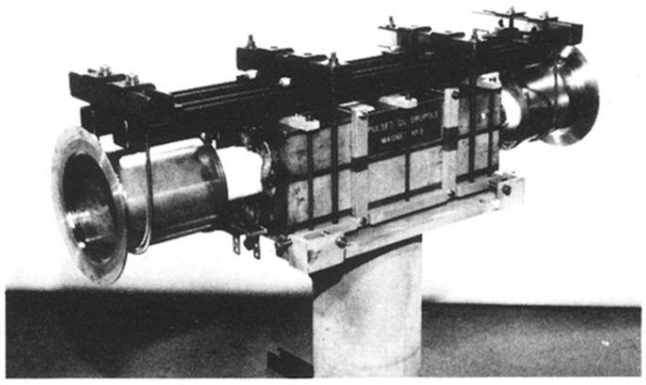

FIG. 18. Picture of an assembled pulsed quadrupole.

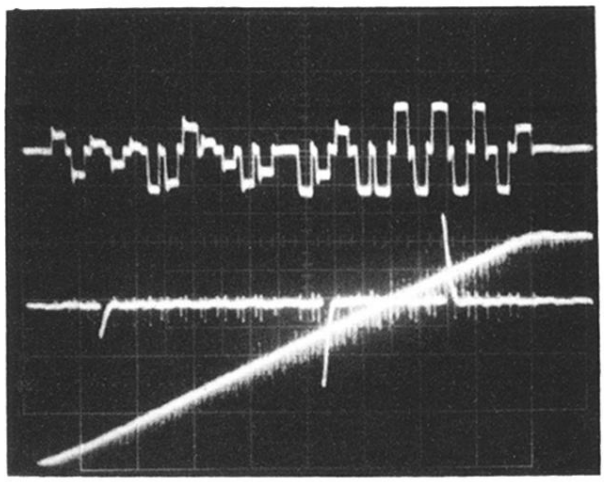

FIG. 30. Oscilloscope trace showing the pulsed quadrupoles firing three times and the dipoles being pulsed 24 times as the rising AGS magnet field guides the polarized protons to 16.5 GeV/*c*.